FEDERAL UNIVERSITY OF CEARÁ

CENTER OF TECHNOLOGY

DEPARTMENT OF STRUCTURAL ENGINEERING AND CIVIL CONSTRUCTION

GRADUATE PROGRAM IN CIVIL ENGINEERING:

STRUCTURES AND CIVIL CONSTRUCTION

FRANCISCO GUERREIRO CHAVES NETO

INVESTIGATIONS ON THE STRUCTURAL BEHAVIOR OF POST-TENSIONED WIND TOWERS USING A NONLINEAR 3D MODEL

FORTALEZA

2022

FRANCISCO GUERREIRO CHAVES NETO

INVESTIGATIONS ON THE STRUCTURAL BEHAVIOR OF POST-TENSIONED WIND TOWERS USING A NONLINEAR 3D MODEL

Thesis submitted to the Graduate Program in Civil Engineering of the Center of Technology of the Federal University of Ceará, as a partial requirement for obtaining the title of Master in Civil Engineering. Concentration Area: Structures.

Advisor: Prof. Dr. Antônio Macário Cartaxo de Melo

FORTALEZA

2022

Dados Internacionais de Catalogação na Publicação
Universidade Federal do Ceará
Biblioteca Universitária
Gerada automaticamente pelo módulo Catalog, mediante os dados fornecidos pelo(a) autor(a)

C438i Chaves Neto, Francisco Guerreiro.
Investigations on the structural behavior of post-tensioned wind towers using a nonlinear 3D model / Francisco Guerreiro Chaves Neto. – 2022.
172 f. : il. color.

Dissertação (mestrado) – Universidade Federal do Ceará, Centro de Tecnologia, Programa de Pós-Graduação em Engenharia Civil: Estruturas e Construção Civil, Fortaleza, 2022.
Orientação: Prof. Dr. Antônio Macário Cartaxo de Melo.

1. Wind towers. 2. Prestressed concrete. 3. External unbonded tendon. 4. Nonlinear analysis. 5. 3D model. I. Título.

CDD 624.1

FRANCISCO GUERREIRO CHAVES NETO

INVESTIGATIONS ON THE STRUCTURAL BEHAVIOR OF POST-TENSIONED WIND TOWERS USING A NONLINEAR 3D MODEL

Thesis submitted to the Graduate Program in Civil Engineering of the Center of Technology of the Federal University of Ceará, as a partial requirement for obtaining the title of Master in Civil Engineering. Concentration Area: Structures.

Approved on: 28 / 04 / 2022.

EXAMINATION BOARD

_____

Prof. Dr. Antônio Macário Cartaxo de Melo (Advisor)
Federal University of Ceará (UFC)

_____

Prof. Dr. Evandro Parente Junior
Federal University of Ceará (UFC)

_____

Prof. Dr. Francisco Alex Correia Monteiro
Aeronautics Institute of Technology (ITA)

To my family, for the willpower, motivation and determination. Mothers, your care and dedication gave me, in some moments, the strength to persist and persevere.

ACKNOWLEDGEMENTS

First and foremost, I would like to thank my family, for the support, appreciation and encouragement during this long journey, which kept me going through arduous and unprecedented times. My mothers, Aurizelia Machado, Maria Olinda and Maria Enir, gave me all the love and care that made it possible to push through adversity.

Secondly, I would like to express my deep and sincere gratitude to my research supervisor, Prof. Dr. Antônio Macário Cartaxo de Melo, for providing invaluable guidance throughout this work and giving me this incredible opportunity. His sincerity, pieces of advice and expertise enabled me to improve and re-analyze my statements. I would also like to thank my examination board members Prof. Dr. Evandro Parente Junior and Prof. Dr. Francisco Alex Correia Monteiro for the brilliant comments, feedback and suggestions.

My brother, who has been the father figure I needed most and whose support is with me in whatever I pursue, thank you for keeping a relaxing and calm atmosphere during hardship and spare times.

I would like to thank my friends and colleagues in the LMCV, where it has been my pleasure and honor to study and develop as a human person during these years. Special thanks to Maurício Melo, for the conversations and debates and for offering important data for this research.

I’m grateful for all of those who offered me love, unity, care, affection and serenity when I needed it most.

“Considerate la vostra semenza:
fatti non foste a viver come bruti,
ma per seguir virtute e canoscenza.”

(Dante Alighieri, *La Divina Commedia*)

ABSTRACT

Prestressed concrete has been used in place of steel in high-rise towers of wind farms around the northeastern region of Brazil, in particular in Ceará State. Researches on the structural analysis of the these towers have sought an alternative to make the analysis process more efficient by simplifying the problem modeling, which could lead to underestimating the applied loads or overestimating the structure strength, depending on the simplification chosen by the engineer. In either case, the preliminary design obtained from such simplified analysis may not be conservative for the problem, missing data that might be important to evaluate the strength and safety of the prestressed tower, such as localized stresses, cracking patterns, tendons behavior and free vibration mode shapes. The overall objective of this study is to offer a high fidelity model with shell, cable and solid elements, and to develop investigations on the structural behavior of prestressed concrete wind towers, providing parameter sensitivity information or to validate low fidelity models (beam models) that incorporate nonlinearities. The refined shell model is applied to an externally prestressed concrete tower with a tapered tube shape, 100 m high, using cable elements to represent the prestressed tendons and solid elements to simulate the foundation. Structural analyses are performed using the DIANA software. Several aspects are investigated, such as: wind model; load combinations; element types; material and geometric nonlinearities; soil-structure interaction; the effects of prestressed tendons details, such as the amount, distribution over the tower height and presence of deviators. Parametric studies have been done to study the sensitivity of the solution to various design parameters. The study has revealed important points to the design of wind towers and supplied contributions to an improved beam element.

Keywords: Wind towers. Prestressed concrete. External unbonded tendon. Nonlinear analysis. 3D model.

RESUMO

O concreto protendido têm sido usados em substituição ao aço nas torres eólicas de grande altura, nos parques eólicos da região nordeste e, em particular, no estado do Ceará. Trabalhos sobre a análise estrutural destas torres têm buscado alternativas para tornar o processo de análise mais eficiente ao simplificar a modelagem do problema, o que pode levar a subestimação das cargas aplicadas ou a superestimação da resistência da estrutura, dependendo da simplificação adotada pelo engenheiro. De qualquer forma, o projeto preliminar obtido a partir dessa análise simplificada pode não ser conservador para o problema, faltando informações que podem ser importantes para avaliar a resistência e segurança da torre protendida, como tensões localizadas, padrões de fissuração, comportamento das cordoalhas e modos de vibração livre. O objetivo geral deste trabalho é oferecer um modelo de alta fidelidade com elementos de casca, cabo e sólido, e desenvolver investigações sobre o comportamento estrutural de torres de concreto protendido, fornecendo informações sobre sensibilidade de parâmetros ou para validação de modelos de baixa fidalidade (modelo de pórtico) que incorporam não linearidades. O modelo de casca refinado é aplicado a uma torre de concreto protendido com formato de tubo cônico, 100 m de altura, utilizando elementos de cabo para representar os cabos de protensão. As análises estruturais são realizadas no *software* DIANA. Vários aspectos da metodologia são investigados, como: modelos de vento; combinação de cargas; tipos de elementos finitos; não linearidades física e geométrica; interação solo-estrutura; os efeitos dos detalhes dos cabos de protensão, como a quantidade, distribuição na altura da torre e presença de desviadores. Estudos paramétricos foram realizados para estudar a sensibilidade da solução com relação a diversos parâmetros de projeto. O estudo revelou pontos importantes para o projeto da torre eólica e forneceu contribuições para um modelo de pórtico aprimorado.

Palavras-chave: Torres eólicas. Concreto protendido. Protensão externa não aderente. Análise não linear. Modelo 3D.

LIST OF FIGURES

LIST OF TABLES

LIST OF ABBREVIATIONS AND ACRONYMS

ACI	American Concrete Insttitute
ANSI	American National Standards Institute
ASCE	American Society of Civil Engineers
BIOS	Biologically Inspired Optimization Tool
CAGR	Compound Annual Growth Rate
CFD	Computational Fluid Dynamics
ECD	Extreme Coherent Gust with Direction Change
EDC	Extreme Direction Change
EOG	Extreme Operating Gust
ETM	Extreme Turbulence Model
EWM	Extreme Wind Model
EWS	Extreme Wind Shear
FAST	Finite Element Analysis Tool
FEM	Finite Element Model
GWEC	Global Wind Energy Council
HSC	High Strength Concrete
IEC	International Electrotechnical Commission
LWST	Low Wind Speed Turbine
NBR	Norma Brasileira
NREL	National Renewable Energy Laboratory
NTM	Normal Turbulence Model
NWP	Normal Wind Profile
RCM	Rotating Crack Model
SANS	South African National Standards
SABS	South African Bureau of Standards
SLS	Serviceability Limit State
ULS	Ultimate Limit State
USA	United States of America
WTG	Wind Turbine Generator

CONTENTS

1 INTRODUCTION

Modern society demands an increased amount of energy. Advancements in materialistic lifestyles, an exponentially growing population and the realization of the adverse effects on the environment caused by the burning of fossil fuels to cope with the energy demands, have increased awareness about adverse climatic changes around the world. Global warming is a real danger, and governments worldwide are implementing strategies to generate large percentages of their countries' power needs with alternative energy sources. Thus, there is a necessity to focus on renewable and clean sources, including wind, solar, geothermal, biomass and ocean. Among them, wind power is receiving more attention worldwide, becoming more accepted by industries and people alike, and it is currently the second-largest renewable energy source, right after hydropower.

The Global Wind Energy Council (GWEC) predicts that by 2035 renewable energy will be generating more than 25% of the world's electricity need, with a quarter of this coming from wind energy (GLOBAL WIND REPORT, 2013).

In 2018, according to GWEC (2019), 51.3 GW of generating capacity wind energy was installed around the world, totaling 591 GW, representing a growth of 9% from 2017. Figure 1 illustrates the history of increasing growth in installed wind energy worldwide, including onshore and offshore Wind Turbine Generators (WTG). The Compound Annual Growth Rate (CAGR) is also shown.

Figure 1 – History of installed generating capacity wind energy worldwide (in GW)

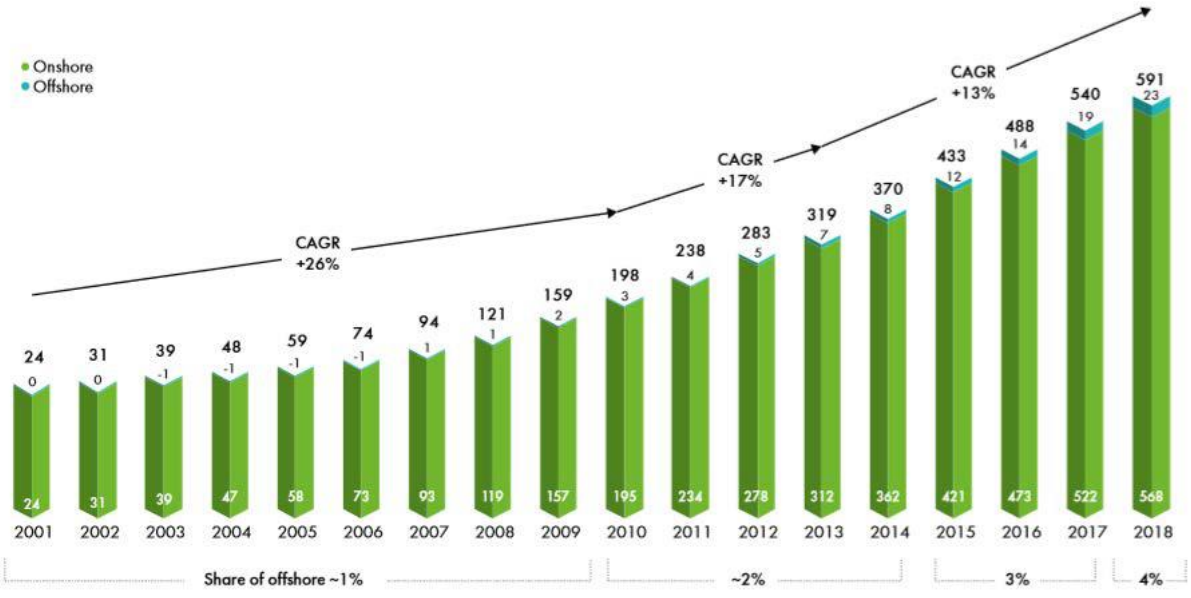

Source: GWEC (2019).

Today, Brazil possesses more than 15.1 GW of installed wind energy generating capacity, produced in 602 wind farms and 7500 wind turbines operating in 12 states, of which Ceará State represents the third place in installed generating capacity. Energy produced in 2018 by wind turbines in the country was 48.4 TWh, or 8.6% of all generating capacity injected into the National Interconnected System (Sistema Interligado Nacional) during the period, it was also responsible for avoiding the emission of 21 million tons of CO_2, an amount equivalent to about 16 million cars. It is expected that Brazil will have more than 20 GW of wind energy capacity installed by 2023 based on data obtained from contracts from auctions already carried out and in the free market (ABEEOLICA, 2019).

The generating capacity and size of wind turbines increased rapidly to harvest more energy from wind and is expected to keep growing in turbine size and production to cope up with power demand (Figure 2).

Figure 2 – Existing and expected growth in hub height and output

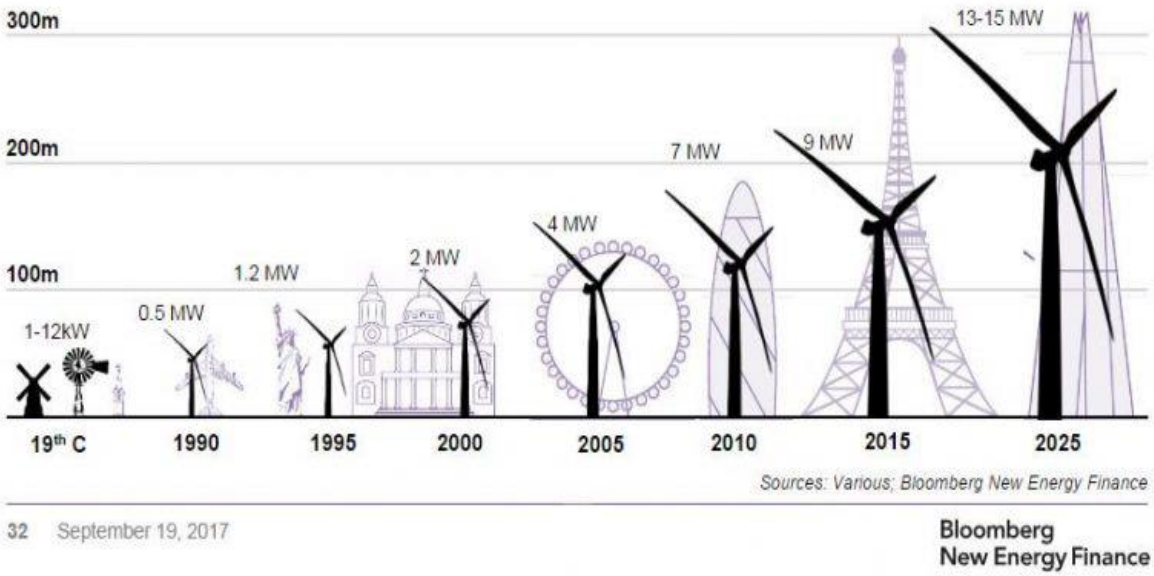

Source: Bloomberg New Energy Finance (2017).

In the year 2013, the average height of new onshore wind turbines was around 118 m, with 33% having heights of 120 m to 140 m (VON DER HAAR & MARX, 2015). The increase in outputs requires longer blades, which demands a higher support structure, as shown by Figure 2. Larger scale wind towers lead to a greater material amount and make the building process more expensive.

Besides the increasing advancements of the technology behind wind turbines, there is also the need to make it cheaper, therefore making those sources more accessible around the world. The cost of wind power generation has been reduced to between US$ 0.04 and US$ 0.07 per kilowatt-hour (REHMAN, ALAM & ALHEMS, 2019).

According to Folster (2016), one of the key arguments for the limit on the size of rotors has commonly been referred to as the “square/cube principle”. That argument shows that for each increase in blade length, the power output increases by the square of the length or diameter of the rotor blades, since the power output is proportional to the area swept by the rotor, but at the same time the volume of the blades, consequently the mass and cost, increases by the cube of the rotor blade length. Therefore, this principle predicts that eventually, the increased cost of the material for the turbine will far surpass the increased power output, making it uneconomical to increase the rotor size.

On the other hand, structural engineers have the power to influence the design of the tower and foundation of a WTG, these two components have a significant influence on the cost of a wind turbine. According to Irena (2012), for a typical onshore wind turbine, the tower will account for 17% of the total cost and the foundation will account for 16% of the total cost, but it highly depends on the specific site and turbine.

One of the challenges for the wind energy construction sector is making higher and cheaper wind towers and foundations, so it remains competitive with others energy sources, which means conceiving a structural design with the lowest possible construction and maintenance cost, but also making it safe to withstand the weight of the turbines, wind loads and general loads over its useful life, alongside an adequate performance in service, without excessive displacements or resonance.

The standard 80 to 90 m steel towers are not economically viable for the energy demand and generating capacity nowadays. Since the base diameter of a steel tower is limited to approximately 4.5 m due to transportation logistics, steel towers have become uneconomical at hub heights greater than 90 m. To solve the height problem, concrete towers are generally used, since concrete is a versatile material that can be used structurally in many different ways. Wind towers can either be made with small enough components (precast) to be transported normally or the tower can be produced on-site (ZYL & ZIJL, 2015).

According to Kenna & Basu (2015), concrete wind towers over 90 m high require prestressing to mitigate the high vertical tensile stresses induced by bending, which would lead to cracking of the concrete and a consequent reduction in their fundamental frequency.

1.1 Justification

Prestressed concrete towers offer many advantages for the wind energy market, as pointed out by Silveira (2017), such as fewer maintenance requirements and more flexibility in design and construction as concrete is a very moldable material. There is also a better dynamic response, as prestressed wind towers present lower vibration and fatigue in comparison to steel towers with similar dimensions, better transportation possibilities, since it allows for smaller concrete sections solution and precast concrete industries can be easily adapted to manufacture different types of towers, depending on the design specifications.

External unbonded tendons also allow for thinner walls for concrete sections. The tendons can be easily installed over various stages of construction, can be easily inspected and replaced, offer more tolerance to fatigue under dynamic loads, less friction loss, easy demolition procedures and many more (THE CONCRETE CENTER & GIFFORD, 2006).

The structural analysis for wind towers usually requires a lot of time, since it is a problem with many variables and complex functions to solve, which could make the analysis process ineffective. In general, structural analyzes are performed using the finite element method.

An alternative to make the analysis process more efficient is simplifying the problem modeling by means of low fidelities finite element simulations, such as the beam model used in Melo (2021), which could lead to underestimating the applied loads or overestimating the structure strength, depending on the simplification chosen by the engineer. In either case, the preliminary design obtained from such simplified analysis may not be conservative for the problem, missing data that might be important to evaluate the strength and safety of the prestressed tower, such as localized stresses, cracking patterns, tendons behavior and free vibration mode shapes. Therefore, a more refined study on the tower's behavior is needed to obtain safer results or validate the simplifications.

1.2 Objectives

The overall objective of this study is to offer a high fidelity model and to develop investigations on the structural behavior of prestressed concrete wind towers, providing parameter sensitivity information or to validate low fidelity models (beam models) that incorporate nonlinearities.

The specific objectives of this study are:

a) Gather information about the state of the art of prestressed and reinforced concrete wind towers;
b) Discuss and evaluate the wind analysis model proposed by Zyl (2014);
c) Develop a finite element analysis model to verify the efficiency of utilizing shell and cable elements to analyze a prestressed concrete wind tower;
d) Verify the structural behavior of large prestressed concrete wind towers during the limit states;
e) Investigate the free vibration response of the tower;
f) Investigate the soil-structure interaction and the effect of different soil conditions on the behavior of the tower;
g) Explore the relationships and trade-offs between different design parameters and the tower's behavior (parametric study);
h) Verify the accuracy of a beam model for prestressed wind towers using the high fidelity model.

1.3 Layout

The first chapter of this research is used to present the growing need for clean and renewable electricity sources worldwide, showing how wind energy advancements as a reliable and trusted energy source for the population. This chapter introduces the general topic in study, justifying the choice of this subject and objectives.

In chapter 2, one presents a literature review, discussing the general idea of the wind towers. The state of art for this subject is also presented here, by showing the studies made about reinforced and prestressed concrete wind towers.

Following next, chapter 3 is used to explain the analysis model developed for the research, including loads, finite elements and material description are described here.

For the 4th chapter, the case study chosen to develop the investigations on the structural behavior is presented, showing the material and geometric properties.

In chapter 5 presents the results obtained during this research and discussions about what has been found.

Finally, chapter 6 is used to give the conclusions and final remarks about the study, showing an overview of the problem and highlighting important results.

2 LITERATURE REVIEW

The references related to the subject of structural analysis of prestressed and reinforced concrete wind turbine towers are presented in this chapter.

2.1 Wind turbines

Nowadays, “Wind turbines” are used as a generic term to describe machines with rotating blades that convert the kinetic energy from the wind into useful power, meaning there is various design for the whole system. Modern wind turbine designs are mostly dominated by upwind horizontal-axis three blades turbines, thus this thesis study focuses on this kind of design.

Figure 3 – Horizontal-axis wind turbine: Vestas V126, rated power 3.45 MW, rotor diameter 126.0 m, tower height 137 m

Source: Wind Turbine Models (2016).

Horizontal axis rotors, which are realized almost exclusively on the basis of propeller-like concepts (Figure 3), are the dominant design for most wind turbines today because of its multiple qualities in comparison to others design principles, such as:

- The rotor blade shape can be aerodynamically optimized (HAU, 2013);

- In propeller design, rotor speed and power output can be controlled by pitching the rotor blades about their longitudinal axis (blade pitch control). Moreover, rotor blade pitching is the most effective protection against overspeed and extreme wind speeds, especially in large wind turbines (HAU, 2013);
- A decisive factor is the vast technological lead in the development of propeller design technology (HAU, 2013).

Vertical axis wind turbines also exist and could be built at sites with frequent change in wind direction, such as rural areas, because it does not need to face into the incoming wind direction, but it is not usual since most wind turbines are built in open rural areas, however, it has a high cost of drive train, low power efficiency and high dynamic loading on the blades.

Most modern wind turbines are of the upwind type, but earlier on turbine development, it was more popular to design downwind turbines (Figure 4), because it does not need an active yaw mechanism since there is no danger for blades to hit the tower. The yaw mechanism present on upwind turbines is used to keep the rotor facing into the wind as the wind direction changes, but there is no need for such mechanism on downwind turbines, since the wind blows the rotor downwind. However, turbulence induced by the tower leads to periodic loads on the blades and power fluctuation. For upwind turbines, since the rotor is placed before the tower along the wind direction, there is no concern for this effect (YANG, 2013).

Figure 4 – Upwind and downwind turbines

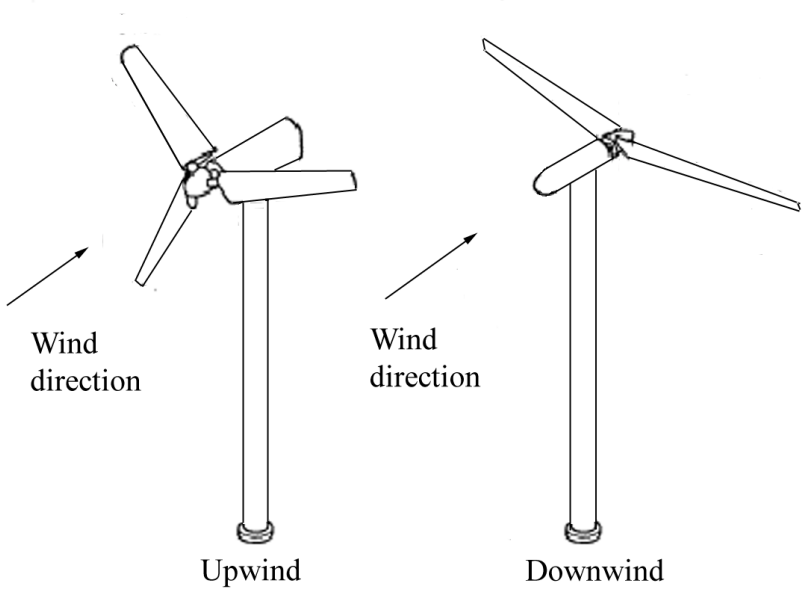

Source: Manwell, McGowan & Rogers (2009).

Due to higher energy capture efficiency and load reduction, three blades rotors are widely used for wind turbines. Figure 5 shows the influence of the number of blades on the rotor power coefficient, what can be observed is a reduction in power coefficient growth with the increase in the number of rotor blades. If one compares the power increase from one to two blades, which is around 10 percent, to the power increase from two to three blades, which is around one to two percent, it is possible to observe the reducing increase of power coefficient. According to Hau (2013), the power coefficient continues to increase with the number of blades.

An important factor shown in Figure 5 is the tip-speed ratio needed to achieve the maximum power coefficient for each number of blades, being the ratio between the tangential speed of the tip of a blade and the actual speed of the wind. The three-bladed rotors reach optimal performance at a tip-speed ratio of between 7 and 8.

It is possible the conclude that any possible gain in power and energy yield by increasing the number of blades beyond three does not justify the cost of having an additional rotor blade, moreover, two or single-bladed rotors cause a noise emission which is unacceptable at most sites, making the three-bladed rotors the most attractive commercially nowadays (HAU, 2013).

Figure 5 – Influence of the number of blades on the rotor power coefficient and the optimal tip-speed ratio

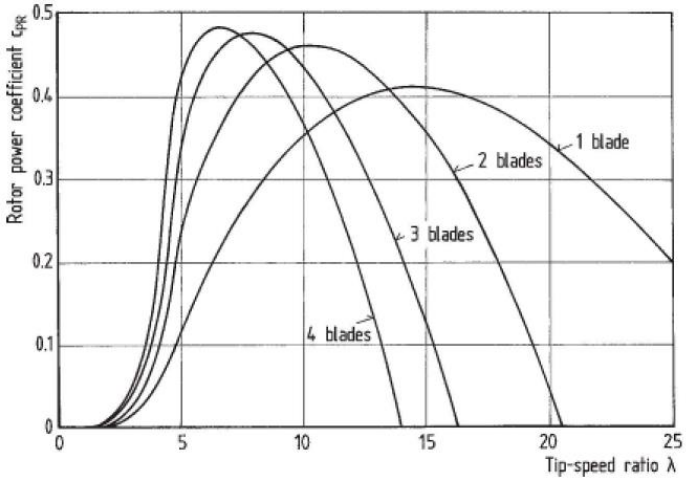

Source: Hau (2013).

The main components of horizontal wind turbines are illustrated by Figure 6 and the main parts are described below according to Manwell, McGowan & Rogers (2009):

- **Rotor:** consists of the blades and rotor hub. Most wind turbines are designed with three blades, as explained before;

- **Drive train:** consist of all the rotating parts of the wind turbine, excluding the rotor itself. It includes the rotor shaft and bearing, gearbox, rotor brake, generator and coupling;
- **Machine control system:** important to the operation of the machine and power production, consist of sensors (position, temperature, speed, flow, current, voltage, etc.), controllers (mechanical mechanisms and electrical circuits), power amplifiers, actuators and intelligence (computers, microprocessors);
- **Nacelle:** it is the wind turbine housing, bedplate and the yaw system;
- **Electrical system:** includes cables, switchgear, transformers and possibly electronic power converters;
- **Tower and foundation:** they are the structural components of the wind tower and the focus of this study.

Figure 6 – Components of a horizontal-axis wind turbine

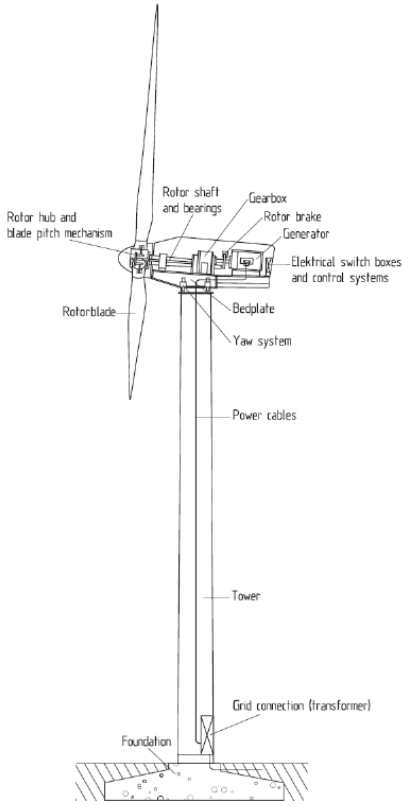

Source: Hau (2013).

When designing the tower, the structural engineers have multiple choices for material and geometry. The tower could be shaped as a tubular cylindrical, tubular-truncated cone, tubular with a parabolic variation or even be a lattice (or truss). Typical onshore towers are designed with reinforced concrete, steel, hybrid materials or prestressed concrete with

internal or external tendons, making use of both *in situ* and precast concrete (Figure 7). The optimal preliminary design of towers depends on various conditions, such as transportation, local manufacturer conditions and lifting methods (GRÜNBERG & GÖHLMANN, 2013). Hybrid towers consisting of a prestressed concrete shaft and a steel top section have proved to be a very economical solution in the 2020s.

Figure 7 – Typical onshore tower designs for wind turbines

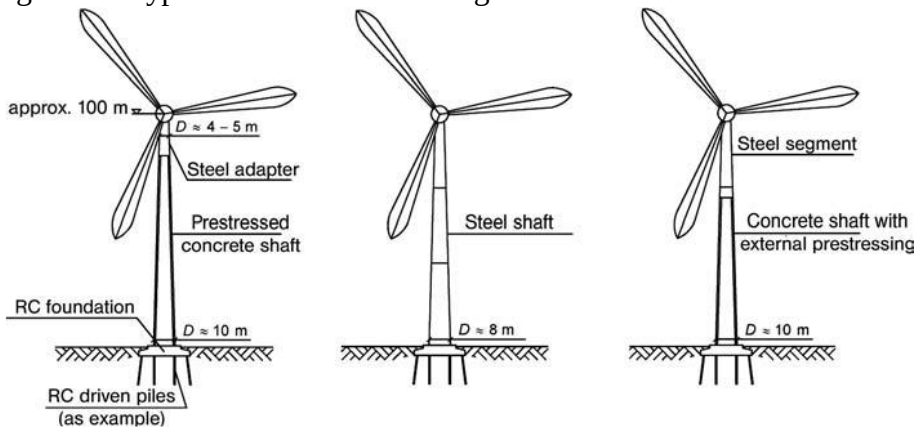

Source: Grünberg & Göhlmann (2013).

Concrete tower industries have grown fast in recent years, having the advantage that there is no transportation limit on the diameter of the tower, therefore there is no limit on the height. There are many other advantages such as: concrete is a durable material that can survive extreme conditions for 50 to 100 years if properly designed; has a long fatigue life; it is possible to retrofit the tower with a new turbine after the turbine's 20 years design life; the concrete tower's self-weight is larger than that of a steel tower, helping resist the overturning moment induced by wind forces; and the foundation cost can be greatly reduced, since the foundation of a concrete tower can be up to 30-40% lighter than that of a steel tower, due to the increased concrete weight (Zyl, 2014).

An important characteristic of a wind turbine is its power output prediction or power curve, which is the power output varying with the hub height wind speed, being possible to predict the energy production of a wind turbine without considering the technical details of each of its various components. Figure 8 shows an example of a power curve.

The power curve gives three important key points to the performance of a wind turbine, they are:

- **Cut-in speed:** the minimum hub height wind speed at which the turbine generates power;

- **Rated wind speed:** the hub height wind speed at which the rated power is reached, generally the maximum power output;
- **Cut-out speed:** the maximum hub height wind speed at which the turbine generates power, it is usually limited by the manufacturer and safety constraints.

Figure 8 – Hypothetical wind turbine power curve

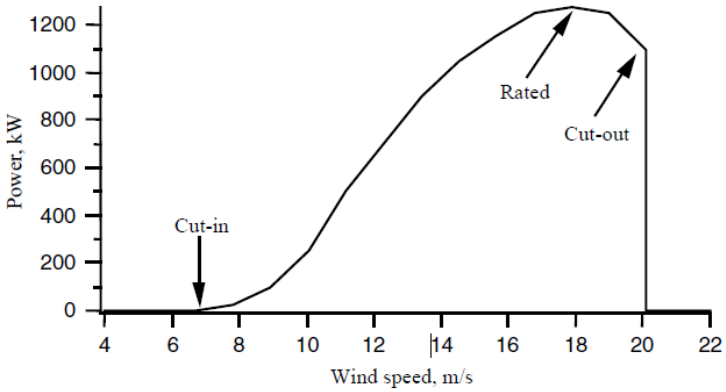

Source: Manwell, McGowan & Rogers (2009).

2.1.1 Wind turbine towers

In this topic, one presents the summary of various researches published in the last years related to the theme of this study. Those works are of vital importance to the understanding of the research problem as well for the definition of its objectives and methodology presented in this project.

LaNier (2005) analyzed hybrids (steel and concrete) and prestressed concrete wind towers with a height of 100 m. The wind loads on the turbine obtained from literature and the wind load on the tower were calculated using the equivalent static method according to the suggestions of the IEC 61400-1 (2005) and the ASCE 7 (1998). The overall objective of the project was the study of the viability of these towers when using the design project materials mentioned before for Low Wind Speed Turbines (LWST).

Nicholson (2011) did a study on the design optimization of steel wind turbine tower and foundation systems using Microsoft Excel optimization tool. In the research loading conditions and recommendations for wind towers from the IEC 61400-1 are used. The analyses are performed assuming linear elastic behavior of the structure. Results demonstrated that optimization concepts and Excel can be used to obtain reasonable conceptual designs and cost estimates for wind turbine towers and foundations, but Excel Solver's Generalized Reduced Gradient method can only handle continuous problems. Since the detailed design of the wind

turbine tower and foundation is inherently discrete, certain simplifications had to be made to overcome the limitations of the Solver, limiting the results to the conceptual design level. Foundations have been incorporated into the optimal design problem and their stiffness has been taken into consideration for evaluating the tower's fundamental frequency. The research found that considering the tower and foundation as an integral system resulted in a more expensive, but safer design. It has also been demonstrated how important it is to incorporate foundation stiffness on the fundamental frequency of the tower, since considering the foundation stiffness in fundamental frequency evaluations will result in a safer preliminary design for the tower. In comparison to a fixed support, the modeling of the tower foundation as a deformation element increases the deflection and reduces the stiffness of the system and its fundamental frequency, thus larger dimensions for the thickness and diameters have to be used in the tower.

Zyl (2014) used one of the towers from LaNier (2005) to investigate the process required to design a concrete wind turbine tower, focusing on determining the appropriate wind models and wind loads to accurately model the tower. A nonlinear shell Finite Element Model (FEM) is used as a analysis tool to evaluate the tower, study the behavior of the tower under different loading conditions and determine the critical design load case. He aims to provide a basic design process that can be followed when designing a concrete wind turbine tower.

The finite element software DIANA FEA was adopted for the tower analysis. The analyzed tower had a truncated cone shape, since the applied stress has a maximum value at the foundation level and gradually reduces to the top, that shape reduces the weight and cost of the tower.

A steel ring was modeled at the top of the tower to prevent the ovalization of the tower's top and forms a platform to which the turbine loads can be applied, simulating the effect that the steel turbine structure has on top of the tower, but it does exist on the tower's design and connects the tower to the nacelle.

Zyl's method for calculating the direct wind pressure on tower uses three different design codes: basic wind speed is calculated according to the IEC 61400-1 (2005), then the wind pressure is calculated using ASCE 7-10 (2010) and the circumference pressure distribution is calculated according to SANS 10160-3 (2011).

The reference wind speed and turbulence intensity are used in wind models to describe different wind conditions. These wind conditions are separated into two categories for load and safety considerations: normal wind conditions, which will occur frequently during the

normal operation of a wind turbine and extreme wind conditions that have a 1-year or 50-year recurrence period.

IEC (2005) describes eight different wind models and, for each design situation, a combination of wind models with other conditions, such as failure or extreme conditions, generates various cases of design loads. Manufacturers provide turbine loads for a specific turbine in a specific wind environment, these loads are regarded as trade secrets and thus not freely available. LaNier (2005) used Computational Fluid Dynamics (CFD) to find the Extreme Wind Model (EWM) and Extreme Operating Gust (EOG) model for this specific turbine and many authors adopted these wind models for the primary design stage of the project (ZYL, 2014; MA & MENG, 2014; GAMA, 2015; ARAÚJO, MELO & ARAÚJO, 2018). Zyl (2014) also analyzes the wind tower for the fatigue design.

The high-strength concrete utilized was limited to the class C80/95 and its characteristic strengths were based on the recommendations of the model code CEB-FIB (2010). This type of concrete is known for its brittle behavior, thus it is necessary to adopt a stress-strain curve that rapidly reduces the stiffness of the material when the principal stress reaches the maximum compressive strength. The Thorenfeldt curve was chosen for the compression behavior of the concrete for its ability to accurately describe the behavior of the material. DIANA offers various stress-strain diagrams, one of which is the Thorenfeldt curve (DIANA FEA 10.3, 2019).

The turbine loads are applied to the steel ring at the top of the tower. Turbine weight and thrust force on the nacelle are applied as a series of loads on each node of the ring. Torsion moment and overturning moments are applied as coupled forces on each ring node. Direct wind pressure on the turbine is applied on the elements, as a function of the height from the base and its radial position from the windward side, therefore each element has its own pressure according to the position.

Zyl (2014) considered the foundation as a rigid element and soil-foundation interaction is modeled as linear springs using the method presented by Gazetas (1983). The soil stiffness is uncoupled into a vertical, horizontal, rotational and torsional stiffness component. Since the dominant mode for the wind turbine tower is the rocking motion, the soil-foundation is simulated only by vertical springs which have a resultant rocking stiffness equal to the one obtained from Gazetas' method (Figure 9). The effect of soil stiffness on the tower fundamental frequency is evaluated for various soils types.

Figure 9 – Soil-structure interaction springs simulation

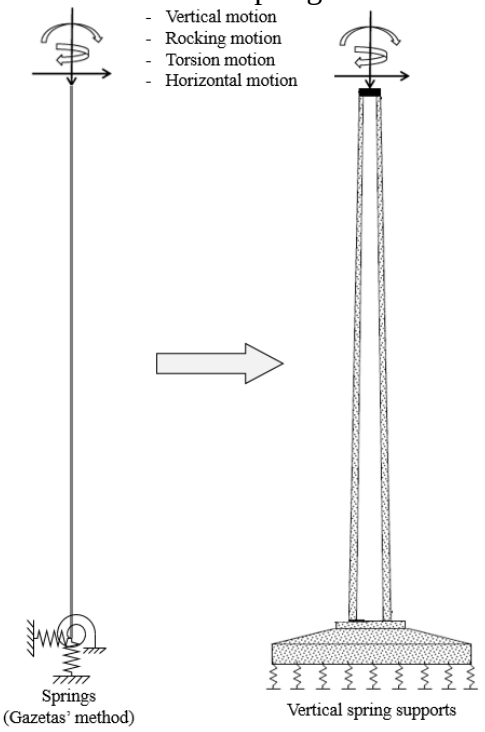

Source: Zyl (2014, adapted).

According to Zyl (2014), for the Serviceability Limit State (SLS), the evaluation of deflections on the tower is important, since great deflections will lower the power production of the turbine and such deflections must be limited. The turbine manufacturer usually gives those deflection limits, otherwise, ACI-307 (2008) is often used. For the Ultimate Limit State (ULS), there is no limit for deflection, provided that there is enough structural strength to avoid collapse.

The fatigue life of the tower is evaluated according to the Model Code CEB-FIB (2010), which allows cracking to occur during the serviceability loads, then loads are reduced by the variable fatigue loads and the structure is analyzed again.

Zyl (2014) observed that the fatigue limit state was not critical for the design stage. The turbine loads adopted for the research were determined by a study done by engineers of the National Renewable Energy Laboratory (NREL) in Colorado, which listed turbines loads obtained using CFD, since the real loads are protected by copyright. The real fatigue life of the tower can only be determined with precision if the real fatigue loads of a specific turbine are provided by the turbine manufacturer.

The tower dynamic behavior and stiffness were also affected by the formation of cracks, as its fundamental frequency had a 46% reduction after the loads application on SLS.

Zyl (2014) verified that the soil type stiffness has a significant influence on the tower's fundamental frequency. When the foundation is built on gravel, a common soil type to put wind turbine towers on, the frequency is reduced by 15%, concluding that the preparation of the soil under the foundation has a strong impact on the dynamic behavior of the tower.

Kenna & Basu (2015) proposed a finite element model, describing the structure of the tower using four-noded two-dimensional Reisser-Mindlin shell elements and a nonlinear stress-strain relationship for the concrete. The prestressing tendons are represented by one-dimensional bar elements with an imposed prestress, using an elastic-perfectly plastic relationship. They studied the effect of varying the design parameter of the magnitude of prestressing and the time dependence of prestressing force was investigated, together with the impact of concrete compressive strength on overall tower stiffness. It is important to mention that wind load on tower was not specified within the paper. Numerical application was done to a concrete wind tower with a 5 MW turbine, 100 m in height, base diameter of 7.62 m and top diameter of 3.658 m, with the wall thickness varying from 762 mm at the base to 457 mm at the top. The concrete compressive strength is given as 48 MPa, with a density of 2450 kg/m³ and a Poisson ratio of 0.15. For the post-tensioned unbonded tendons, the study adopted a modulus of elasticity of 196.5 GPa and yield stress of 1860 MPa. Non-prestressed reinforcement has not been included in the model. The losses were included in terms of anchorage, friction and elastic deformation losses during construction, and for the long-term losses: creep, shrinkage and relaxation.

It was found that compression softening in the concrete tower led to a reduction in tower stiffness for the particular tower studied, since the shell of the tower carried initial compressive stress, reducing the out-of-plane stiffness in shell structures. That softening was expected, because the tendons would become stiffer, that being out of plane, since their tension do not contribute to the stiffness of the structure for the fact that they are unbonded and could not offset the softening present on the concrete (KENNA & BASU, 2015). It is also important to note that, for the geometry of the tower adopted by Kenna & Basu (2015), the effect of compression softening due to prestress is really low when high-strength concrete is used, but becomes higher when lower strength concrete is used. It was found that at higher stress levels, the extent of the reduction in stiffness is highly influenced by the nonlinear material properties of concrete, but at lower stress levels, the geometrical stiffness considerations plays a significant part in the softening.

According to Kenna & Basu (2015), it is important to take into consideration the nonlinear behavior of the concrete on prestressed towers, including the concrete behavior on

tension and compression. Using the modified Hognestad model for the concrete behavior, the researchers concluded that an increase in prestressing forces results in a greater influence of the nonlinear nature of concrete in compression on the stiffness of the structure to the same level extent as the membrane forces within the shell, whereas for lower levels of prestressing, the reduction in stiffness is predominantly due to compression softening caused by geometrical stiffness considerations (Figure 10).

Figure 10 – Concrete material model effect on tower's behavior

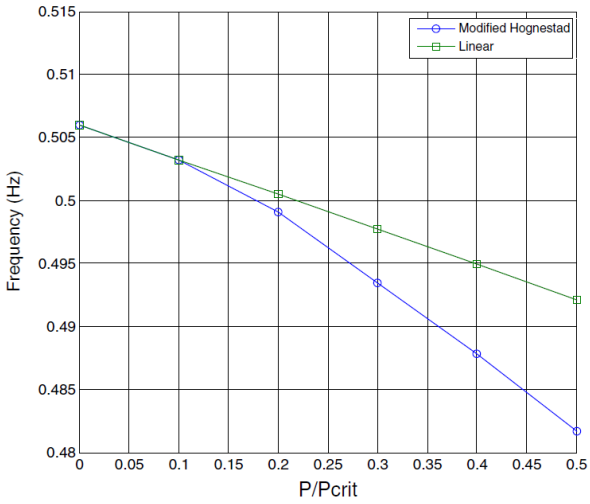

Source: Kenna & Basu (2015).

The formation of cracks in the concrete can have a significant effect on the behavior of the tower, and even make it difficult to predict the dynamic behavior. Post-tensioned tower construction is suitable for dynamically loaded structures and should eliminate the formation of cracks in the concrete if the post-tension is sufficiently large, increasing the durability of the structure and being possible to accurately compute the behavior of the tower. The cracking reduction also minimizes the need for a fatigue limit state analysis. This justifies the increased cost of using this method on concrete wind towers (ZYL & ZIJL, 2015).

According to Brasil & Silva (2016), a nonlinear dynamic analysis for slender structures, such as telecommunication reinforced concrete towers, is essential for the analysis, since these structures are susceptible to dynamic load, which could lead to larger displacements and stress on the structure up to three times greater than those obtained from a simple linear static analysis. That could be related to the fact that the displacement and fundamental frequency of the statically determined structure in analysis are sensitive to the decrease of strength of the tower lower segments. The nonlinear dynamic analysis is computationally intensive, making the analysis and a structural optimization process ineffective when using this

method, therefore many researchers use the static or equivalent static methods to consider wind loads (NICHOLSON, 2011; MA & MENG, 2014; BAI *et al*., 2017; ARAÚJO, MELO & ARAÚJO, 2018).

Bai *et al*. (2017) applied an optimization method for a tall external prestressed wind turbine tower. The optimization method consists of using an augmented Lagrangian particle swarm-based optimizer, verifying the constraints by using the Code_Aster finite element analysis software. The tower is modeled using Timoshenko beam elements to access all static stress states and natural frequencies. The optimization method used is efficient for dealing with constrained design optimization problems, being a population-based global optimization method, allowing to solve large-scale problems. The tower was 140 m in height with a 3 MW turbine and tendons anchored on the foundation and top of the tower. The geometry and material of the tower consists of a conical concrete part with variable thickness at the bottom, a cylindrical concrete part with variable thickness in the middle and a cylindrical metallic ring with a constant thickness on top. The objective function to be minimized is the construction cost of the wind turbine tower, as a function of the volume of materials with weighted coefficients to represent construction costs. The design variables are the wall thickness and prestress force. The constraints used in this research are related to the maximum compressive stress on concrete, no tensile stress, natural frequency and fatigue. The authors did not discuss the turbine loads and fatigue analysis details.

Barroso Filho (2018) studied the influence of the type of finite element (one and two-dimensional), material and geometric nonlinearities and soil-structure interaction on the behavior of reinforced concrete wind towers, using linear springs on the base to simulate the soil-foundation interaction, demonstrating that there is a significant decrease on the tower fundamental frequency when that interaction is taken into consideration. There was also a change in the fundamental frequency when analyzing the cracking on the concrete, that effect was represented by the secant stiffness of the material, resulting in a decrease in the modulus of elasticity by 31% of the original value for ULS and 41% for SLS.

Duarte (2019) presented a formulation for cost optimization of reinforced concrete wind towers, using a one-dimensional finite elements analysis, a simplified model for the treatment of material nonlinearities, by reducing the modulus of elasticity, and an investigation of dynamic wind modeling for efficient optimization. The loading conditions and recommendations of NBR 6118 (2014) and IEC 61400-1 (2005) are used. The design variables are treated as discrete, namely, the characteristic dimensions of tubular cone tower segments, reinforcement and the concrete strength. In that research, towers with a height of 100 m or more

are studied, with the diameter of the base reaching values of 11.4 m, much larger than the 4.4 m of metallic towers, which is possible because of the concrete moldable behavior.

According to Duarte (2019), the three wind models from NBR 6123 presented similar results on the optimization, since all of these have a similar order of magnitude when compared to the magnitude of the turbine loads. Therefore, it is recommended to use simpler models, such as the static wind models, being more efficient and less computationally intensive.

Melo (2021) developed a formulation for cost optimization of externally prestressed wind towers, with the tower modeled as a finite element beam model, considering the geometric and material nonlinearities. The prestress tendons are modeled as a load resistance element. The finite element software FAST (Finite Element Analysis Tool) has been used to model the tower and the software BIOS (Biologically Inspired Optimization Tool) has been used for optimization purposes. The research adopted the wall thickness, tower diameter and number of prestressing tendons as the design variables. The constraints adopted are related to the natural frequency of the tower, wall thickness and diameter, concrete tensile stress, concrete compressive stress and maximum displacement.

Tomczak (2021) did a finite element analysis of post-tensioned concrete wind turbine towers using ANSYS software. It used multiple towers based on LaNier (2005), obtained by extrapolating the tower geometric properties and a composite section to represent the concrete and prestressing steel. It is important to mention that it does not evaluate the direct wind load on the tower, as site-specific wind speeds were not defined, and the prestressing forces are applied as equivalent point loads. The results consist of computing the maximum and minimum von-Mises stress and total deformation from static structural, eigenvalue buckling and modal ANSYS module. The study aimed to show the viability of concrete for tall turbine tower material and provide information for evaluating prestressed tendon towers design, but lacks a deeper explanation of the tower's behavior and the methods adopted for the model.

Lana *et al*. (2021) studied the behavior of prestressed concrete wind-turbine towers in circular cross-section, using a genetic algorithm to obtain an optimal design of the tower, minimizing the stress concentrations. The study found a tubular design that requires less material than an optimized polygonal section. Analyses consisted of evaluating displacements, buckling, stress distribution and vibration modes.

A brief summary of the most important works presented in this section is shown in Table 1, providing some information about what topics has been studied so far and differences between them.

Table 1 – Summary of the literature review

	Type of research		**Type of tower**			**Wind Load on Tower**		**Reinfor-cement**		**Finite Element**		**Found-ation**		**Tendon Deviators (External)**		**Tendons Anchorage (Prestressed)**	
References	Analysis	Optimization	Reinforced	Hybrid	Prestressed	With	Without	With	Without	1D	3D	With	Without	With	Without	Base to top	Along the tower
LaNier (2005)	X		X	X	X	X		X			X	X			X	X	
Zyl (2014)	X		X			X		X			X	X	X	-	-	-	-
Kenna & Basu (2015)					X	X			X		X		X		X	X	
Zyl & Zijl (2015)	X		X			X		X			X	X	X	-	-	-	-
Bai *et al.* (2017)		X			X	X			X	X			X		X	X	
Barroso Filho (2018)	X		X			X		X		X	X	X	X	-	-	-	-
Duarte (2019)		X	X			X		X		X			X	-	-	-	-
Melo (2021)		X			X	X		X		X		X	X		X	X	
Tomczak (2021)	X				X		X		X		X		X		X		X
Lana *et al.* (2021)		X			X	X			X		X		X		X	X	
Present study	X		X		X	X	X	X	X		X	X	X	X	X	X	X

Source: elaborated by the author.

2.2 Working frequency

Wind turbine structures are exposed to multiple external excitation frequencies that can cause the structure to vibrate, which can cause resonance, resulting in the structure suffering large displacements or even immediate failure. Therefore, those excitations must be taken into consideration to ensure that the fundamental frequency of the structure does not coincide with those external vibration frequencies (ZYL & ZIJL, 2015).

Working frequency is designed for a structure with fundamental frequency within the limits of the blade rotational frequency (1P) and the blade passing frequency (3P), classified as a soft-stiff structure. The soft-stiff structure is more economical for wind turbine towers (ZYL, 2014). It is important to mention that modern wind turbines are variable-speed turbines, therefore the 1P and 3P frequencies are not fixed frequency but intervals.

Figure 11 – Excitation frequencies

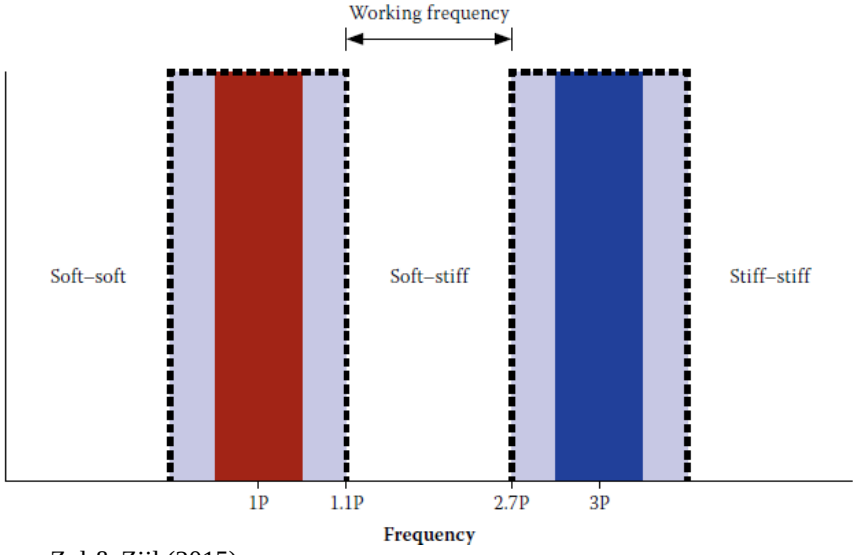

Source: Zyl & Zijl (2015).

Because of the uncertainty of the calculated frequency on the design phase of the project, the tower frequency is kept out of ± 10% of the 1P and 3P frequency intervals (DNV & RISO, 2002). The frequency between the 1.1P and 2.7P is defined as the working frequency of the turbine being. Figure 11 illustrates the working frequency interval.

2.3 Foundation

The foundation plays an important part when analyzing the tower's behavior and designing wind turbine towers. Considering the tower foundation fully fixed at the base could lead up to 20% difference on the tower fundamental frequency (DNV & RISO, 2002). According to DNV & RISO (2002), the effect of the soil stiffness on the frequency is higher than that of the foundation itself. The soil stiffness can be modeled as a finite element model and interface elements can be used to simulate the soil-structure interaction. An alternative generally proposed by wind turbine guidelines, less time-consuming and less computationally intensive, involves using linear springs to simulate the soil stiffness.

By using the linear springs method, which is simple and cost-effective, the soil stiffness is uncoupled into a vertical, horizontal, rotational and torsional stiffness component, and the foundation it is assumed to be rigid and supported on the springs.

Gazetas (1983) offers a model, which is widely used for representing the stiffness of the soil through linear springs. For a circular foundation on a homogeneous half-space, the soil stiffness to vertical (K_V), horizontal (K_H), rocking (K_R) and torsion (K_T) are (Figure 9):

$$K_V = \frac{4GR}{1-\nu} \quad (1)$$

$$K_H = \frac{8GR}{2-\nu} \quad (2)$$

$$K_R = \frac{8GR^3}{3(1-\nu)} \quad (3)$$

$$K_T = \frac{16GR^3}{3} \quad (4)$$

where *R* is the radius of the foundation, *G* is the dynamic shear modulus of the soil, which can be obtained from Table 2 for different soil types and *v* is the Poisson's ratio of the soil.

Table 2 – Properties of typical soil types

Soil type	Dynamic Young's modulus (MPa)	Dynamic shear modulus (MPa)[a]
Fine sand	110	41
Sand	170	63
Coarse sand	200	74
Gravel	300	111
Soft clay	35	13
Clay	70	25
Stiff clay	140	50

[a] Poisson's ratio for sand is taken as 0.40 and for clay is taken as 0.35.

Source: Zyl (2014).

These equations do not take into account that the foundation is embedded into the soil, therefore the stiffness obtained with Equations (1) to (3) must be multiplied by embedment factors as presented below for vertical, horizontal and rocking mode of motion. There is no embedment factor for torsion.

$$\eta_V = 1 + 0.6(1-\nu)\left(\frac{h}{R}\right) \quad (5)$$

$$\eta_H = 1 + 0.55(2-\nu)\left(\frac{h}{R}\right) \quad (6)$$

$$\eta_R = 1 + 1.2(1-\nu)\left(\frac{h}{R}\right) + 0.2(2-\nu)\left(\frac{h}{R}\right)^3 \quad (7)$$

where *h* is the embedment depth.

It is important to mention that the added stiffness due to embedment will only be accurate if there is complete contact between the foundation sides and the soil surrounding it, which might be affected by various factors such as concrete shrinkage and poor soil compacting. Therefore, taking into consideration these embedment effects would not be conservative and they are not taken into account for this research, as proposed by Zyl (2014).

For the wind turbine tower, the rocking motion is the dominant mode. To represent this the foundation is supported on vertical springs that give the same rocking stiffness as the one calculated on Gazetas' method. A typical gravity spread foundation size for a 3.6 MW turbine is illustrated in Figure 12 and is going to be used for this study.

Figure 12 – Typical gravity spread foundation dimensions

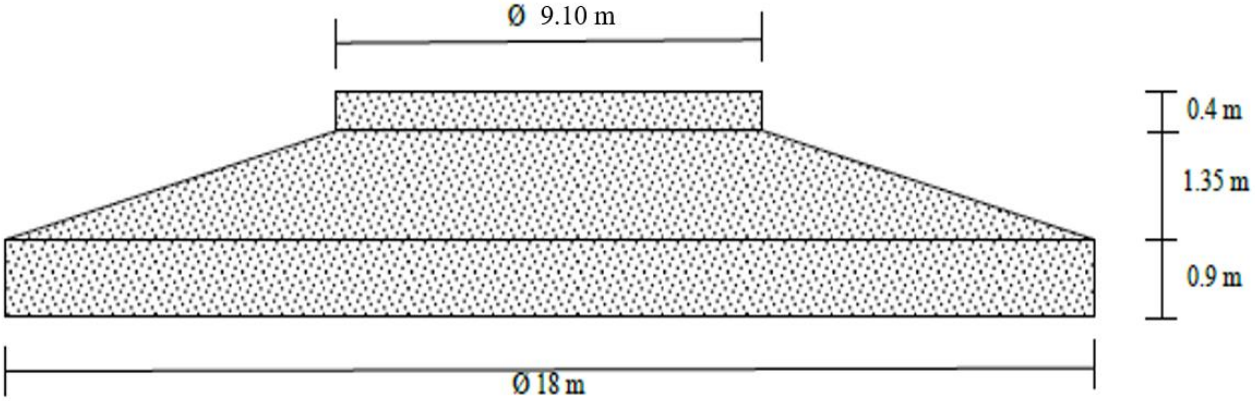

Source: Zyl (2014, adapted).

2.4 Prestressing of the tower

Prestressing the tower is a process that distributes a circumferentially uniform pattern of prestressing forces to be applied at a certain value that changes with height, because the tower has to resist different forces at certain heights. Vertical tensile stress in the tube walls may be avoided with a sufficient circumferentially uniform vertical compressive stress provided by the application of prestressing, also contributing to the shear strength of the tower tube.

Prestressing provides an efficient and economic means to design a wind tower, providing strength, excellent durability, fatigue and dynamic performance to the structure. Prestressed concrete towers for onshore wind turbines may be constructed using either *in situ* or precast concrete techniques. When building a precast concrete tower, it provides a means to unify the separate rings, making it so that they act as a monolithic tower structure, it also provides solutions to the problems of handling units for erection and maintaining adequate

strength in the partially completed tower during its construction, this can be observed in Figure 13 (THE CONCRETE CENTER & GIFFORD, 2006).

Figure 13 – Precast concrete tower construction

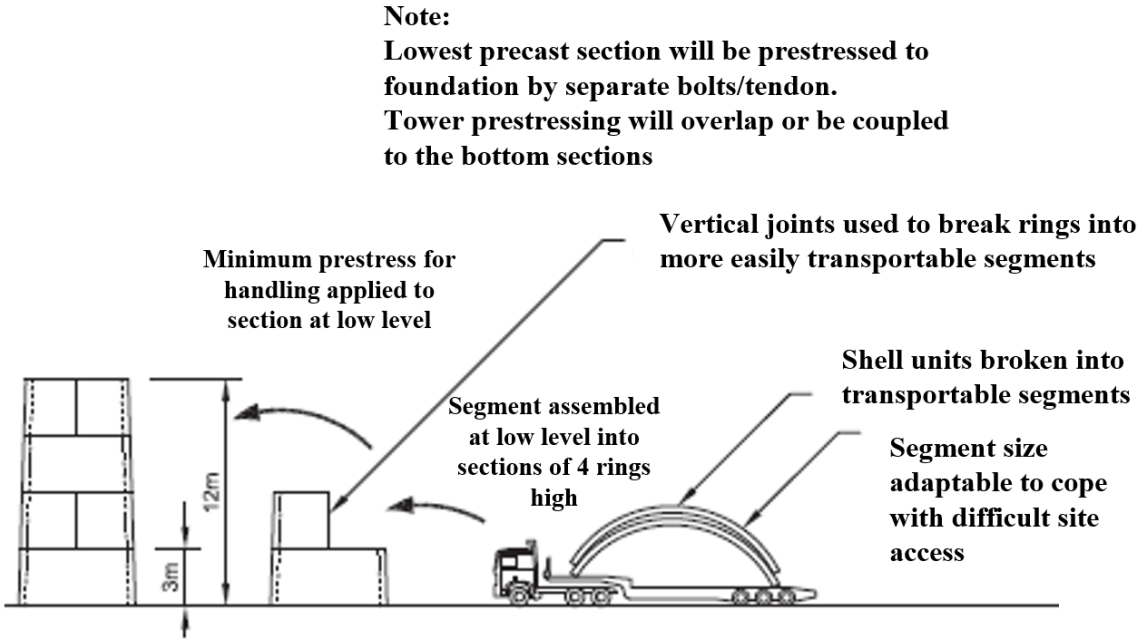

Source: The Concrete Centre & Gifford (2006).

The structural engineer has three choices of general technique and configuration: internal bonded and internal or external unbonded tendons. Unbonded external tendons are the preferred option for this study, mainly because of their simplicity, ease of installation and low cost.

By design, the external tendon is not continuously bonded to the section in question, although the engineer might restrain it back to the shell at discrete points along its length. For the tower, the vertical and parallel to the wall prestressing is applied using a circular array of tendons placed within the concrete tower, close to its inside face.

External prestressing (which could be wire, strand, tendon, cable or bars) are placed outside the structural section which is to be prestressed, thus removing the need to accommodate the tendons and any ducts within the shell wall and permitting the use of thin-walled concrete sections. Therefore, there are fewer restrictions to the wall thickness and the installation of the tendons during the various stages of construction can be easily achieved.

An anchorage is required at each end of the tendon, being the place where the stressing force is imposed, transferring it back into the section. Figure 14 illustrates an example of how a prestressed precast concrete tower with external tendons is designed.

Figure 14 – Prestressed precast concrete tower with external tendons

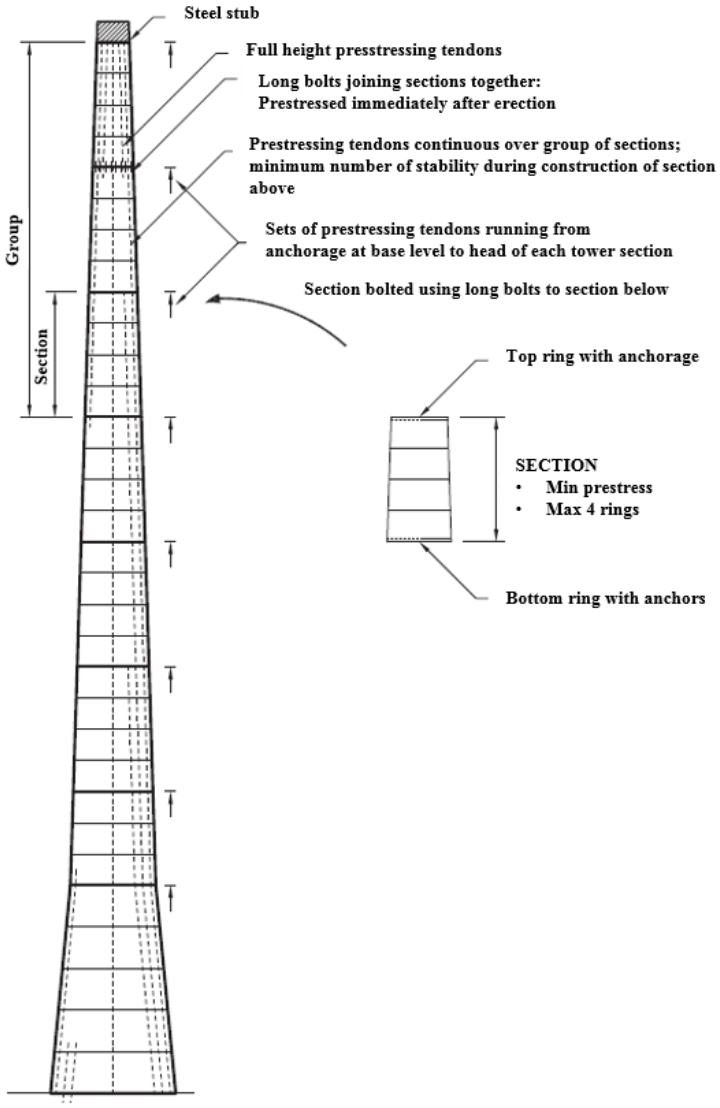

Source: The Concrete Centre & Gifford (2006).

One may think that external prestressing tendons are more susceptible to corrosion, which is an easily solvable problem with simple solutions. Many bridge structures use external tendons, and although the maintenances play an important part on the durability of highly stressed components, particularly in the anchorage areas, the tendons are already protected by factory-installed corrosion protection systems, which include inhibitors, greasing and heavy plastic sheathing. Proper finishing, capping and inhibiting grease injection can be easily done in the anchorage areas.

Unlike internal prestressing tendons, external tendons are visible, easily inspected and replaceable, making maintenance much easier for the structure, when built within the internal tower shaft, the tendons are sheltered and located in a relatively benign environment, where humidity and condensation could be controlled as a further precaution.

According to The Concrete Center & Gifford (2006), there are more advantages to the external unbonded prestressing, which includes:

- Higher fatigue tolerance of dynamic loading as compared to bonded tendons, since the tendons will experience an overall averaged stress, thus lower stress range during loading cycling, where bonded are subjected to higher more localized stress;
- Lower friction losses during stressing;
- Simplified eventual demolition of the structure;
- Recovery of the concrete and steel components for recycling will be simpler and cheaper.

LaNier (2005) states that post-tensioned concrete towers of the same extreme load capacity are of similar stiffness as steel towers, being even cheaper than the latter for taller towers, since for larger wind turbines and taller towers the construction cost for tubular steel towers increases exponentially and costs of construction logistics increases.

When applying prestress one must take into account the prestress losses, which can be: short-term losses due to elastic shortening of concrete, friction, anchor retraction and the wobble effect, which is the loss due to straightening or stretching of the tendons; long-term prestressing levels also change due to relaxation, shrinkage and creep of the structure. The level of prestressing should be evaluated accurately. If that is not possible the design prestressing level should be reduced to 70% for SLS and ULS simulations.

Some researchers state that using deviators on the individual unbonded tendons, which link them back to the tower shell, is fundamental for the design (GRÜNBERG & GÖHLMANN, 2013). These deviators provide additional stability to the tower under accidental overload or high-level impact. In addition, it is a safety measure restraining any whiplash movement if the tendon fails due to overstressing, which might occur during erection.

Those deviators also help with the eccentricities of the tendons, which needs to be considered in the deformed loadbearing structure, because in this case, the tendons on the windward side coincide with the chord, but those on the leeward side touch the inside of the tower shaft, according to Figure 15-a. By building the deviators on the inside of the tower shaft, the tendons follow a polygonal line in the deformed loadbearing structure without touching the inside of the tower shaft, resulting in restoring forces and second-order change-of-direction

forces, which can be observed in Figure 15-b. The deviators must be positioned at the third points at least (GRÜNBERG & GÖHLMANN, 2013).

Figure 15 – Actions of the exposed external prestressing tendons: a) without deviators, b) deviator-guided tendons

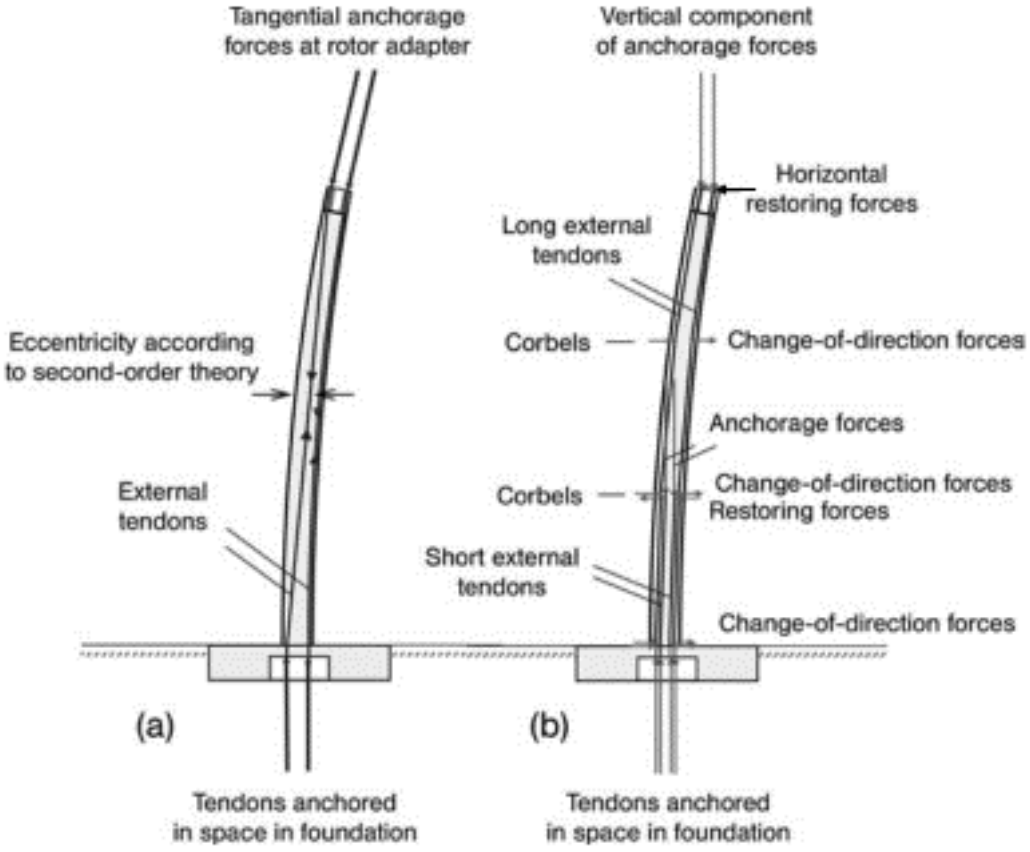

Source: Grünberg & Göhlmann (2013).

Another important aspect is that external prestressing creates anchorage forces, which act tangentially to the deformed structure, that is with restoring horizontal components.

The restoring forces and second-order change-of-direction forces are associated with friction forces, for which the deviators must be designed. An example of tendon deviator is illustrated in Figure 16, which are “U” bars stainless steel cast into the shell, fabricated as part of the cage with a saddle bolted on.

Figure 16 – Tendon deviator example

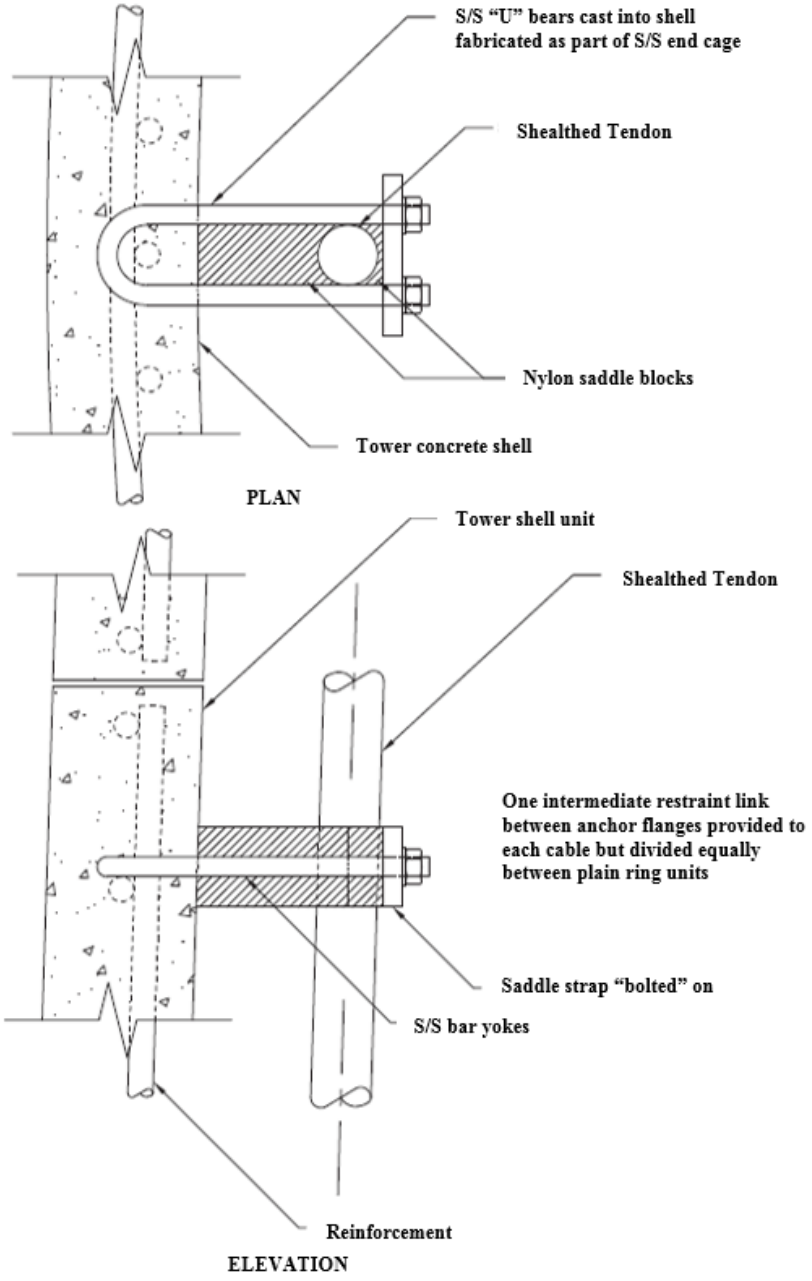

Source: The Concrete Centre & Gifford (2006).

3 ANALYSIS MODEL

In the following section, a strategy to model the loads applied on the tower and the prestressed tower for the finite element analysis in DIANA is presented, using elements and material models already implemented on the software.

3.1 Loads

For WTG towers, loadings consist of evaluating dead load, due to self-weight of the structure and the prestressing forces, and wind loads, as direct wind pressure on the tower and turbine, which are the most significant live load. The structure's self-weight is beneficial for resisting bending, as it creates a compressive force in the concrete (ZYL, 2014).

This section is used to describe the chosen model adopted for this study to obtain the wind loads imposed on the structure, since there is currently no design code for the design process of WTG towers, including reinforced and prestressed concrete towers.

There are many ways to take into consideration the wind load for the design process. Although it is considered as a dynamic load, according to the Brazilian design code ABNT NBR 6123 (2013), the wind load can be modeled as a static load with an amplification factor.

Brasil *et al.* (2003) show that loads calculated for a precast telecommunication tower using the static analysis generate higher stress than the ones obtained using pseudo-static loads obtained from the dynamic analysis with a discrete model. Duarte (2019) demonstrates that static wind models are more conservative, producing more expensive solutions than the simplified and discrete dynamic models, even though static wind models do not take into consideration the wind dynamic behavior. A dynamic analysis for the wind loads on the tower, without taking into consideration the dynamic loadings on the turbine and blades might produce nonrealistic results. Thus, this work adopts the model proposed by Zyl (2014) and various design codes are used to obtain the wind loads.

3.1.1 Direct wind pressure on tower

This section describes Zyl's method for calculating the direct wind pressure on a wind turbine tower and three different design codes are used to accomplish this. Basic wind speed is calculated according to the IEC 61400-1 (2005), then the wind pressure is calculated using ASCE 7-16 (2016) and finally, the circumference pressure distribution is calculated

according to SANS 10160-3 (2011). Please refer to Appendices A and B for a more detailed flowchart to obtain the direct wind pressure on the WTG tower.

Figure 17 – Flowchart for wind pressure evaluation

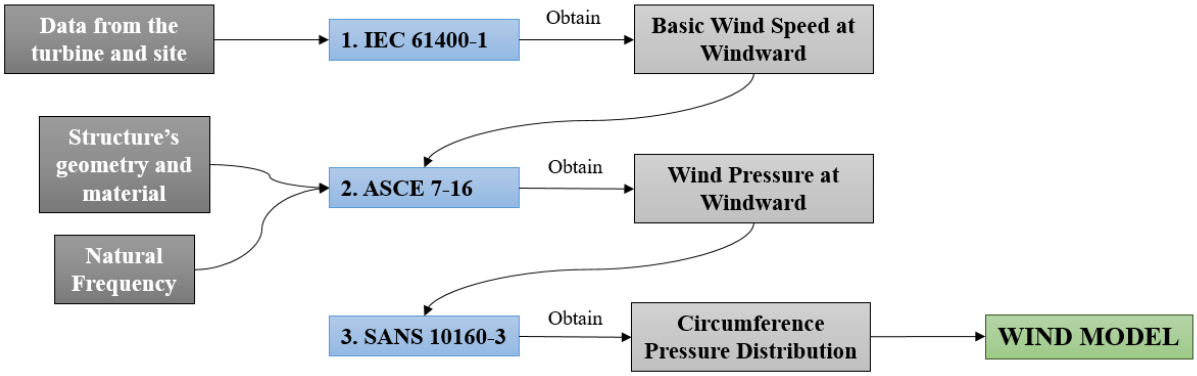

Source: elaborated by the author.

3.1.1.1 Basic wind speed (IEC 61400-1)

The international standard IEC 61400-1 (2005), published by the International Electrotechnical Commission (IEC), gives minimum design requirements for wind turbines and is not intended for use as a complete design specification or instruction manual (IEC, 2005). It is useful for obtaining the design wind speed and appropriate wind model for a WTG, by categorizing it into three classes based on the typical wind environment that it will be exposed to (Class I, II and III) and can be further sub-divided into categories A, B and C according to the turbulence characteristics of the wind. It is important to mention that the turbine classes describe a generic type of site for a specific type of turbine and not a specific site. Besides the standard three classes, a fourth one is specified (Class S), which must be used when the turbine is exposed to wind conditions not covered by the standard classes, such as hurricanes.

The standard classes are shown in Table 3. The speed V_{ref} is the reference wind speed average over 10 minutes on a 50-years recurrence period, A is the category for higher turbulence characteristics, B is the category for medium turbulence characteristics, C is the category for lower turbulence characteristics and I_{ref} is the expected value of the turbulence intensity at 15 m/s. Turbulence intensity is defined as the ratio between wind speed standard deviation and wind speed average, determined from a set of sample data measured from wind speed and taken over a specified period of time. Those wind profile components are illustrated in Figure 18.

Table 3 – Standard wind turbine classes

Wind turbine class	**I**	**II**	**III**	**S**
V_{ref} (m/s)	50	42.5	37.5	Values specified by the designer
I_{ref} – A	0.16			
I_{ref} – B	0.14			
I_{ref} – C	0.12			

*All values apply at hub height

Source: IEC (2005).

Figure 18 – Wind profile components

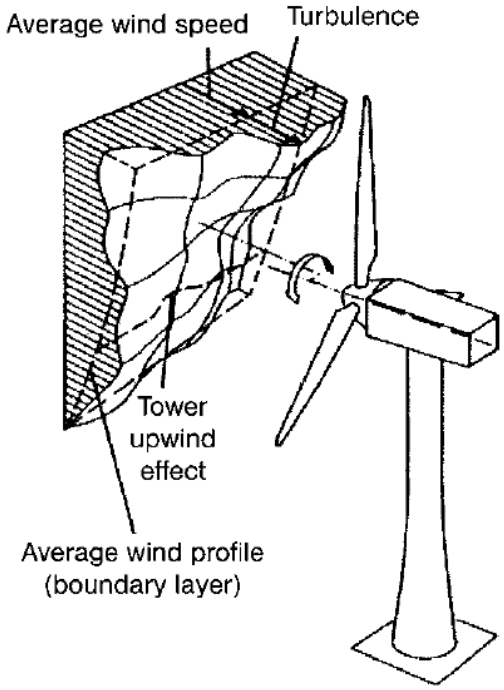

Source: Grünberg & Göhlmann (2013).

The values for reference wind speed average and turbulence intensity given in Table 3 are then used in wind models to describe different wind conditions, that could be separated into two categories for load and safety considerations: normal wind conditions, which will occur frequently during normal operation of a wind turbine and the extreme wind conditions that have a 1-year or 50-year recurrence period. IEC (2005) describes eight different wind models, which are: Normal Wind Profile (NWP), Normal Turbulence Model (NTM), Extreme Wind Model (EWM), Extreme Operating Gust (EOG), Extreme Turbulence Model (ETM), Extreme Direction Change (EDC), Extreme Coherent Gust with Direction Change (ECD), and Extreme Wind Shear (EWS). Nowadays, the manufacturers provide turbine loads only for two extreme conditions, the EWM and EOG models. These and others important models are explained in the following topics.

The normal wind profile model (NWP)

The two of the most used models for describing mean wind speed with height are power law and logarithmic law. IEC (2005) uses the power law to describe the average wind speed with height, *V(z)*:

$$V(z) = V_{hub}\left(\frac{z}{z_{hub}}\right)^{\alpha} \quad (8)$$

where V_{hub} is the reference wind speed according to turbine class, as shown in Table 3, z is the vertical coordinate measure from the ground to where the wind speed is calculated, z_{hub} is the coordinate z for the hub height.

The power law exponent α depends on the ground roughness and IEC 61400-1 (2005) uses the value of 0.1 for extreme conditions and 0.2 for normal conditions, which is for terrains with the following description: tall row crops, hedges and a few trees.

The normal turbulence model (NTM)

The value for turbulence standard deviation for the standard turbine classes (σ_1) is represented by Equation (9) and is given by the 90% quantile for a given wind speed at hub height (IEC, 2005).

$$\sigma_1 = I_{ref}(0.75V_{hub} + b) \quad (9)$$

where b = 5.6 m/s and I_{ref} is the turbulence intensity according to turbine class and turbulence category as presented in Table 3.

The extreme wind model (EWM)

In this model, the turbine is stationary, which is a non-operating condition. EWM can either be a steady or a turbulent wind model. Turbulent wind model is used for dynamic analysis. Steady extreme wind speeds are given by the following equations:

$$V_{e50}(z) = 1.4V_{ref}\left(\frac{z}{z_{ref}}\right)^{0.11} \tag{10}$$

$$V_{e1}(z) = 0.8V_{e50}(z) \tag{11}$$

where V_{e50} is the steady extreme 3-second gust wind speed with a recurrence period of 50 years, V_{e1} is the steady extreme 3-second gust wind speed with a recurrence period of 1 year, V_{ref} is the reference wind speed for the standard wind turbine classes given in Table 3, z is the height where the wind speed is calculated and z_{ref} is the vertical coordinate of where the V_{ref} is defined, which is the hub height.

The extreme operating gust (EOG)

The hub height gust magnitude for the standard wind turbine classes with an expected recurrence period of 50 years (V_{gust}) according to IEC (2005) is given by:

$$V_{gust} = Min\begin{cases} 1.35(V_{e1} - V_{out}) \\ 3.3\left(\dfrac{\sigma_1}{1 + 0.1\left(\dfrac{D}{\Lambda_1}\right)}\right) \end{cases} \tag{12}$$

where V_{out} is the cut-out wind speed at hub height that is given by the turbine manufacturers, which is the maximum wind speed at which the turbine is allowed to deliver power, σ_1 is the turbulence standard deviation at hub height given in Equation (9) and Λ_1 is the longitudinal turbulence scale parameter for $z_{hub} \geq 60$ m, which value is assumed to be 42 m, and D is the turbine rotor diameter.

The following equation defines the wind speed for EOG:

$$V(z,t) = \begin{cases} V(z) - 0.37V_{gust}sin\left(\dfrac{3\pi t}{T}\right)\left(1 - cos\left(\dfrac{2\pi t}{T}\right)\right) & for\ 0 \leq t \leq T \\ V(z) & for\ t > T \end{cases} \tag{13}$$

where the speed $V(z)$ is given in Equation (8) and T = 10.5 s.

By taking the maximum peak value obtained on Equation (13) one obtains the static 3-second gust wind speed for the EOG model, which means this model can be used as a static

model. Figure 19 shows an example of the extreme operating gust wind profile (V_{out} = 25 m/s, Class II_B, D = 108.4 m).

Figure 19 – EOG wind speed profile at hub height

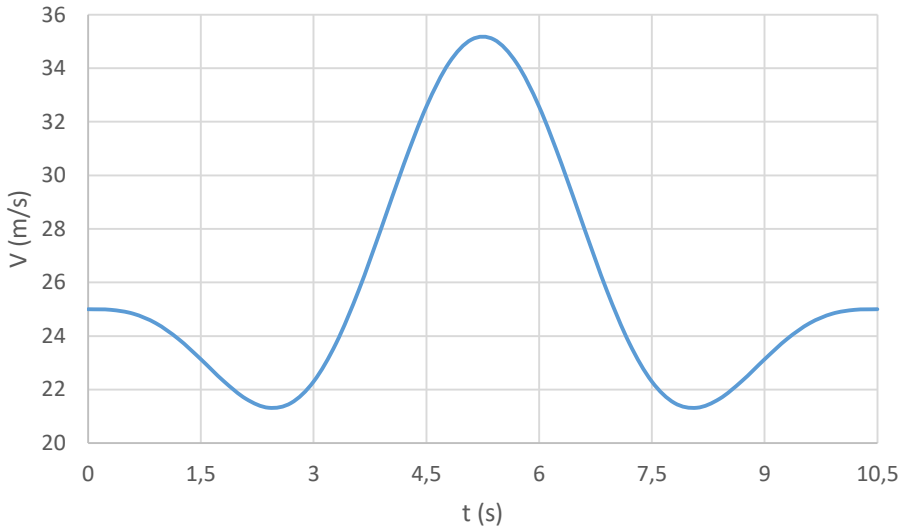

Source: elaborated by the author.

3.1.1.2 Wind pressure (ASCE 7-16)

The ASCE 7-16 (2016) guides the civil engineers to calculate the minimum design loads for buildings and other structures. This design code is used in this research due to the fact that it considers the dynamic interaction between a slender structure and the wind by using the gust factor method, it distinguishes between stiff structures (f_n > 1 Hz) and slender structures that have a fundamental frequency below 1 Hz, which is important since concrete wind turbine towers of 100 m height normally have a first natural frequency in the range of 0.4 Hz.

The code states that wind calculations are applicable to a regularly shaped building or structure which does not have response characteristics related to the action of transverse wind loading, vortex shedding, instability due to galloping or flutter.

Wind pressures on the Main Wind-Force Resisting System of chimneys are stated in Chapter 29 of the code. Concrete chimney design codes are often used for the design of concrete wind turbine towers because the geometry and slenderness are similar for these structures.

Wind speed calculated by using IEC (2005) is the 3s gust wind speed at hub height. Therefore, it must be converted to wind speed at 10 m to be used on the wind pressure according to ASCE 7-16 (2016). The updated reference wind speed for EOG can be obtained by using the

power law given in Equation (8) with 0.2 exponent and for EWM the exponent must be taken as 0.1.

The following equations describe the steps determined by the ASCE 7-16 (2016) to calculate the design wind pressure on the wind turbine tower.

The wind pressure in N/m² as a function of tower height is given by:

$$q_z(z) = 0.613 K_z K_{zt} K_d K_e V^2 I G \tag{14}$$

where the coefficient K_{zt} represents the topographic factor that takes account of the wind speed-up effect at hills and ridges where the topography of the landscape changes abruptly, and is taken as 1.0 (the value for flat terrains), K_d is the directionality factor, takes into account the shape of the structure and is 0.95 for round towers, and K_e is the ground elevation factor to adjust for air density in function of the structure placement above sea level and can be taken as 1.0 for any elevation. The speed V is the basic wind speed (m/s) with a 3 second averaging time at a height of 10 m, which should be obtained for EOG and EWM. The importance factor I takes into account the risk to humans in the case of structural failure. Since wind turbines are usually constructed in areas where humans are not in close proximity, such as open rural areas, this factor can be taken as 1.0. K_z is a velocity exposure coefficient and is a function of surface roughness and the height of the structure, as given by:

$$K_z = \begin{cases} 2.01\left(\dfrac{z}{z_g}\right)^{\frac{2}{\alpha}} & for\ 4.6 < z < z_g \\ 2.01\left(\dfrac{4.6}{z_g}\right)^{\frac{2}{\alpha}} & for\ z < 4.6 \end{cases} \tag{15}$$

where, z is the distance from the ground which is being used to calculate the pressure, α = 11.5 for exposure category D (Table 4), z_g = 213.36 m, it is the gradient height of exposure category D (Table 4).

Zyl (2014) adopted the exposure category D from ASCE 7-16 (2016), which is used for open unobstructed terrains, since wind turbines are usually constructed in sites with few obstructions to the wind, being an important factor to optimize the generating power for this type of turbine.

The gust effect factor *G* becomes G_f for flexible or dynamic sensitive structures, which is important for wind towers. It accounts for build and gust size, dynamic amplification caused by the design wind speed, the fundamental frequency of vibration and the damping ratio (ASCE 7-16, 2016), and it is calculated by:

$$G_f = 0.925\left(\frac{1 + 1.7I_{\bar{z}}\sqrt{g_Q^2Q^2 + g_R^2R^2}}{1 + 1.7g_vI_{\bar{z}}}\right) \tag{16}$$

where g_Q = 3.4 and is the peak factor for background response and g_v = 3.4 is the peak factor for wind response.

Turbulence intensity at height $\bar{z}$ is given by:

$$I_{\bar{z}} = c\left(\frac{10}{\bar{z}}\right)^{\frac{1}{6}} \tag{17}$$

where $\bar{z} = 0.6h$, being the equivalent height of the tower and *h* is the tower height. The background response (*Q*) is given by the expression:

$$Q = \sqrt{\frac{1}{1 + 0.63\left(\frac{B + h}{L_{\bar{z}}}\right)^{0.63}}} \tag{18}$$

where $L_{\bar{z}}$ is the integral length scale of turbulence at the equivalent height:

$$L_{\bar{z}} = l\left(\frac{\bar{z}}{10}\right)^{\bar{\epsilon}} \tag{19}$$

The peak factor for resonance g_R is given by:

$$g_R = \sqrt{2\ln(3600n_1)} + \frac{0.577}{\sqrt{2\ln(3600n_1)}} \tag{20}$$

where n_1 is the tower fundamental frequency in Hz. The resonant response factor *R* is given by:

$$R = \sqrt{\frac{1}{\beta} R_n R_h R_B (0.53 + 0.47 R_L)} \tag{21}$$

where β is the material damping ratio, which is usually taken as 0.02 for concrete and between 0.004 to 0.007 for prestressed concrete structures (BACHMANN *et al.*, 1995). The present study takes the damping ratio as 0.005. The resonant response components are:

$$R_n = \frac{7.47 N_1}{(1 + 10.3 N_1)^{\frac{5}{3}}} \tag{22}$$

$$N_1 = \frac{n_1 L_{\bar{z}}}{\bar{V}_{\bar{z}}} \tag{23}$$

$$R_h = \frac{1}{4.6 n_1 \frac{h}{\bar{V}_{\bar{z}}}} - \frac{(1 - e^{-2\left(4.6 n_1 \frac{h}{\bar{V}_{\bar{z}}}\right)})}{2\left(4.6 n_1 \frac{h}{\bar{V}_{\bar{z}}}\right)^2} \tag{24}$$

$$R_B = \frac{1}{4.6 n_1 \frac{B}{\bar{V}_{\bar{z}}}} - \frac{\left(1 - e^{-2\left(4.6 n_1 \frac{B}{\bar{V}_{\bar{z}}}\right)}\right)}{2\left(4.6 n_1 \frac{B}{\bar{V}_{\bar{z}}}\right)^2} \tag{25}$$

$$R_L = \frac{1}{15.4 n_1 \frac{L}{\bar{V}_{\bar{z}}}} - \frac{(1 - e^{-2\left(15.4 n_1 \frac{L}{\bar{V}_{\bar{z}}}\right)})}{2\left(15.4 n_1 \frac{L}{\bar{V}_{\bar{z}}}\right)^2} \tag{26}$$

$$\bar{V}_{\bar{z}} = \bar{b} \left(\frac{\bar{z}}{10}\right)^{\bar{\alpha}} V \tag{27}$$

where V is the basic wind speed (m/s), B is the width of the tower perpendicular to the wind direction and L is the tower dimension parallel to the wind direction, therefore both are equal to the tower diameter.

The constants required to calculate wind pressure are given in Table 4 for each exposure category.

Table 4 – Wind constants

Exposure	α	$z_g(m)$	$\hat{a}$	$\hat{b}$	$\bar{a}$	$\bar{b}$	c	$l\,(m)$	$\bar{\epsilon}$	$z_{min}\ (m)^a$
B	7.0	365.76	$\frac{1}{7}$	0.84	$\frac{1}{4.0}$	0.45	0.30	97.54	$\frac{1}{3.0}$	9.14
C	9.5	274.32	$\frac{1}{9.5}$	1.00	$\frac{1}{6.5}$	0.65	0.20	152.40	$\frac{1}{5.0}$	4.57
D	11.5	213.36	$\frac{1}{11.5}$	1.07	$\frac{1}{9.0}$	0.80	0.15	198.12	$\frac{1}{8.0}$	2.13

[a] z_{min} is the minimum height used to ensure that the equivalent height $\bar{z}$ is greater of $0.6h$ or z_{min}.

Source: ASCE (2016).

According to Kenna & Basu (2015), the magnitude of prestressing force and the time after prestressing which the structure is analyzed influences the fundamental frequency of the structure. The researchers applied the prestressing force as a percentage of the critical buckling load of the tower and the results are presented in Figure 20.

It is important to determine the fundamental frequency of the structure after prestressing is applied at the tendons and before evaluating the wind load on the tower, since the gust factor for wind loads is influenced by the fundamental frequency. As higher is the ratio of applied prestress to buckling load (P/P_{crit}), as lower is the natural frequency, which in turn results in higher wind pressure on the tower (Figure 21).

Figure 20 – Fundamental frequency versus magnitude of prestressing force

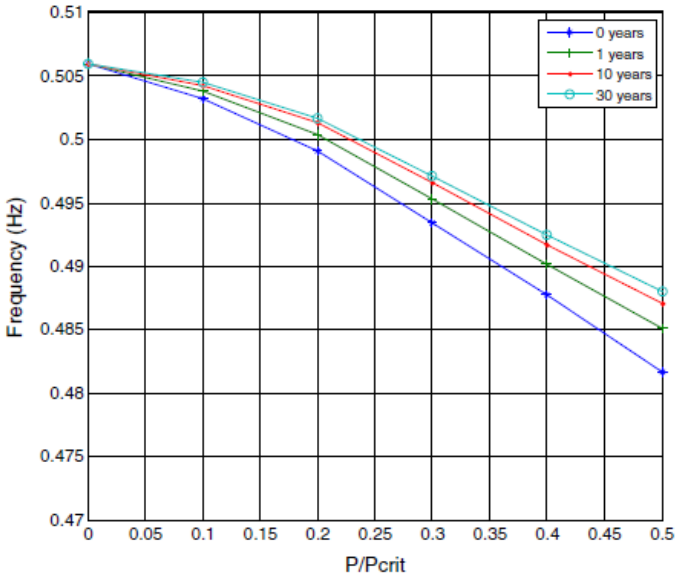

Source: Kenna & Basu (2015).

Figure 21 – Pressure versus fundamental frequency sensitivity analysis at hub height for Zyl's wind model (EWM)

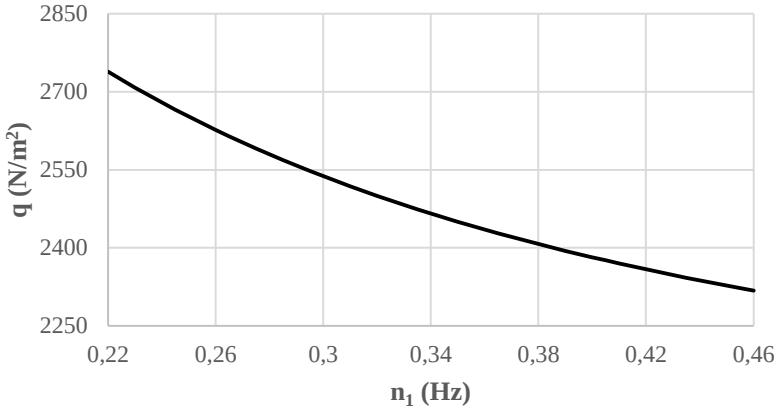

Source: elaborated by the author

3.1.1.3 Circumferential pressure distribution (SANS 10160-3)

The circumferential pressure distribution is calculated using the proposed method by SANS (2011), which gives guidance on the determination of natural wind actions for the structural design of buildings and industrial structures and is published by the South African Bureau of Standards (SABS).

The Reynolds number that describes the flow regime of the wind highly influences the circumference pressure distribution. SANS (2011) gives the external pressure coefficients for various Reynolds numbers. The pressure distribution for cylinders based on an equivalent roughness of $k/b < 5x10^{-4}$ is presented on Figure 22.

Figure 22 – Pressure distribution for cylinders with different Reynolds numbers

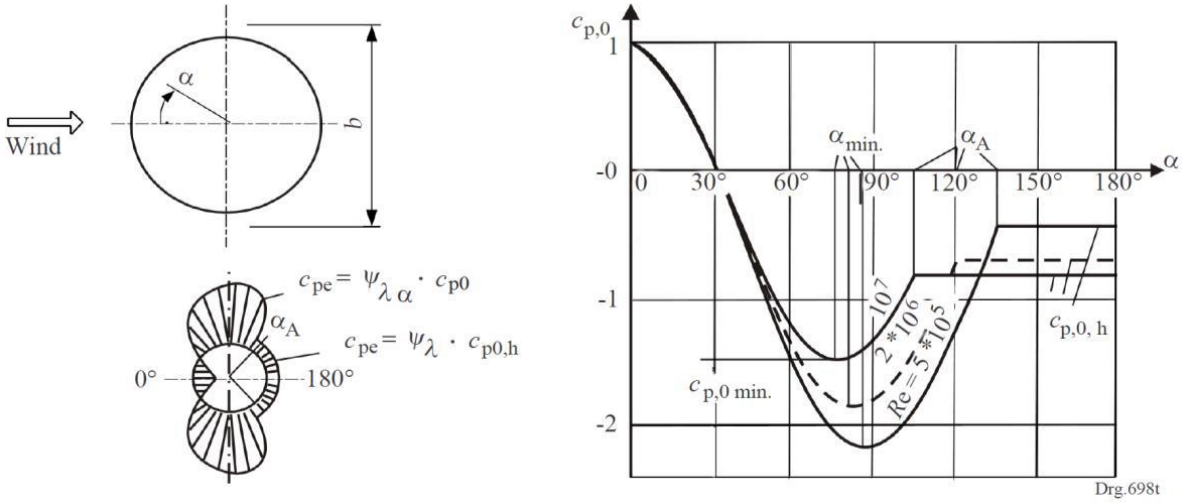

Source: SANS (2011).

The parameter *k* is the roughness protrusion and *b* is the diameter of the cylinder. The concrete wind turbine tower used in this work satisfies the limit for *k/b*. It is important to mention that the direct wind pressure acting on the tower causes a positive pressure on the windward side and a negative pressure (suction) on the sides and leeward of the tower. Table 5 gives the critical pressure coefficients of Figure 22.

According to SANS (2011), the intermediate values may be obtained from linear interpolation. Figure 23 demonstrates the values obtained for pressures on top of the tower for various polynomial interpolation and extracted using the WebPlotDigitizer tool in Figure 22. It is possible to observe that linear interpolation leads to underestimating the pressure, as it provided an overall lower wind pressure on the tower. Thus, this research adopted the quadratic interpolation and only uses the linear interpolation suggested by the design code for comparison purposes.

Table 5 – External pressure coefficient

Re	α_{min} [a]	$c_{p,0min}$ [b]	α_A [c]	$c_{p,0,h}$ [d]
$5\ x\ 10^5$	85	-2.2	135	-0.4
$2\ x\ 10^6$	80	-1.9	120	-0.7
10^7	75	-1.5	105	-0.8

[a] α_{min} is the position of the minimum pressure expressed in degrees.

[b] $c_{p,0min}$ is the value of the minimum pressure coefficient.

[c] α_A is the position of the flow separation, expressed in degrees.

[d] $c_{p,0,h}$ is the base pressure coefficient.

Source: SANS (2011).

Figure 23 – Different interpolation for circumferential pressure distribution

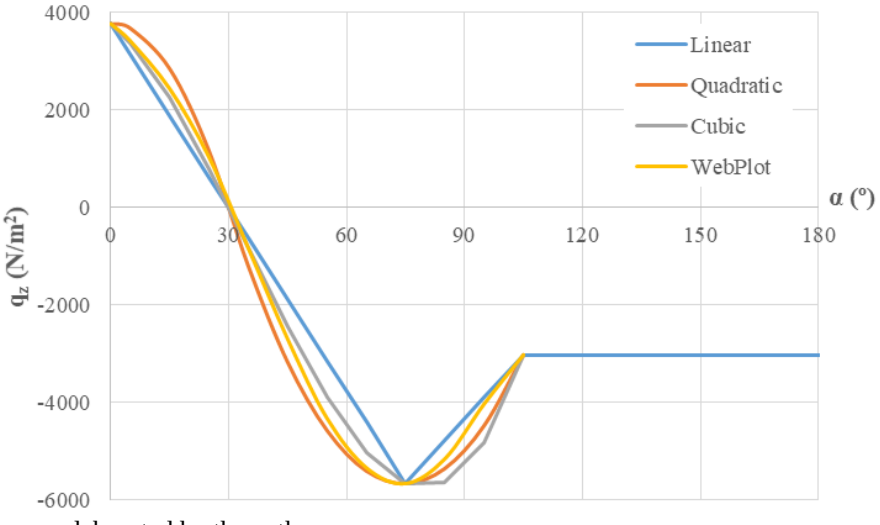

Source: elaborated by the author.

3.1.2 Wind pressure on tower considering dynamic effects (ABNT NBR 6123)

Wind loads according to the ABNR NBR 6123 (2013) can be evaluated as a static or dynamic action. A structure with a fundamental period equal to or lower than 1 second ($f \geq 1$ Hz) has a small or insignificant dynamic effects response. However, structures with higher fundamental periods ($f < 1$ Hz) may exhibit significant dynamic responses. Wind speed fluctuation may induce significant oscillations on the average wind speed direction for flexible or dynamic sensitive structures, which are called fluctuation responses.

The dynamic portion of the wind load can be evaluated as a quasi-static action, i.e., the dynamic effects on the structure are taken into consideration on the static load.

The design wind speed ($\overline{V_p}$) for roughness class II terrains, which is classified as open and leveled terrains, with few isolated obstacles, such as short buildings and trees, is obtained from the equation:

$$\overline{V_p} = 0.69 V_o S_1 S_3 \tag{28}$$

where V_o is the reference wind speed average over 10 minutes on a 50-years recurrence period at 10 m above ground level. S_1 is the topographic factor, taken as 1.0 for flat terrains, for deep valley it is taken as 0.9 and for slopes it varies depending on the vertical coordinate and the slope inclination. S_3 is the statistical factor, which takes into consideration the required safety level of the building and it is taken as 0.95 for industrial buildings and installations with low occupancy factor (deposit, silo, rural buildings, etc.), for other buildings types please refer to annex A.

The dynamic pressure in N/m^2 varies along the height according to:

$$q(z) = \bar{q}_0 b^2 \left(\left(\frac{z}{z_r} \right)^{2p} + \left(\frac{h}{z_r} \right)^{p} \left(\frac{z}{h} \right)^{\gamma} \frac{1 + 2\gamma}{1 + \gamma + p} \xi \right) \tag{29}$$

where the first term inside the bracket corresponds to the average response, the second one corresponds to the maximum amplitude of the fluctuation response and:

$$\bar{q}_0 = 0.613\overline{V_p}^{\,2} \ (\bar{q}_0 \text{ in N/m}^2 \text{ and } \overline{V_p} \text{ in m/s}) \tag{30}$$

The exponent p and parameter b depend on the terrain category, for terrain class II they are taken as 0.15 and 1.00, respectively, for other terrain roughness classes please refer to annex A. z_r is the reference height for the wind speed, h is the structure's height and γ can be taken as 2.7 for concrete towers and chimney with variable cross-section.

The dynamic amplification factor ξ is a function of the building dimensions, the critical damping factor ζ (taken as 0.015 for variable cross-section concrete towers) and the frequency f. It is obtained using the dimensionless factor $\overline{V_p}/fL$ in Figure 24 for roughness class II terrains. I_1 is the structure's diameter and intermediate values for ξ can be obtained using linear interpolation.

Figure 24 – Dynamic amplification factor ξ for roughness class II terrains (L = 1800 m; h in meters)

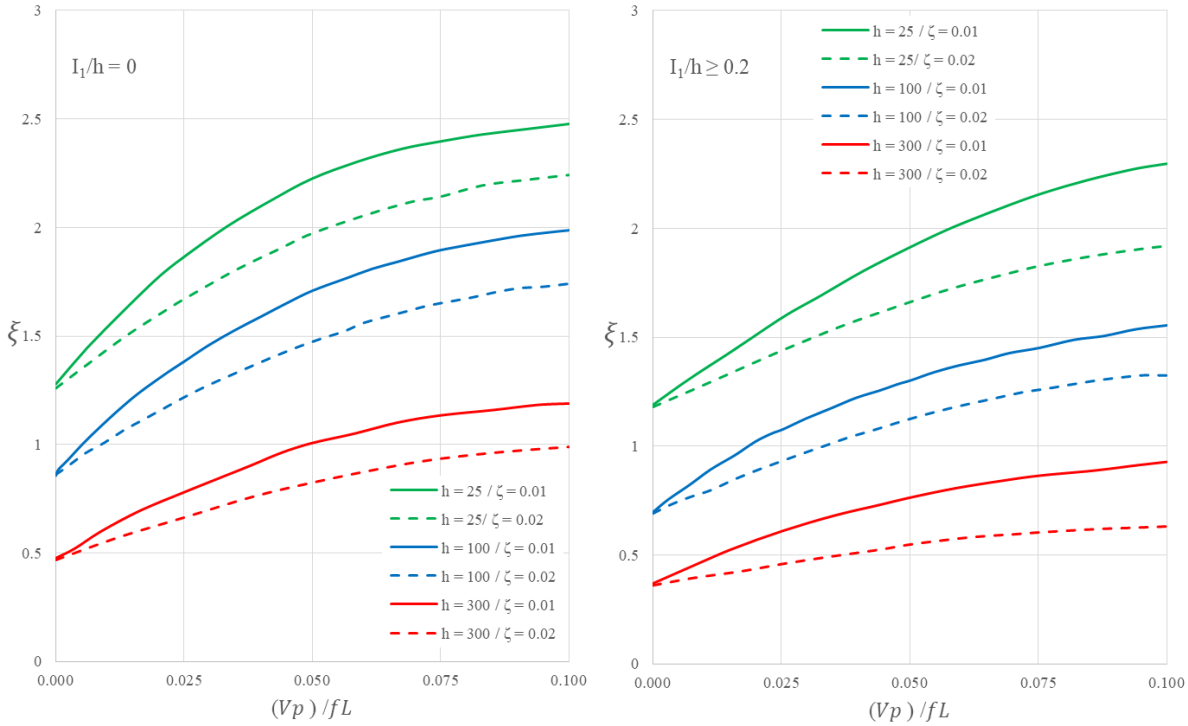

Source: ABNT NBR 6123 (2013, adapted).

This method takes into consideration the fundamental frequency of the structure, therefore it is important to determine the frequency of the structure after prestressing is applied at the tendons before evaluating the wind load on the tower. Higher prestressing loads lead to a

decrease of the fundamental frequency, which in turn increases the dynamic amplification factor and the wind pressure on the tower.

Figure 25 – Wind pressure versus fundamental frequency sensitivity analysis at hub height for the ABNT NBR 6123 (2013) wind model

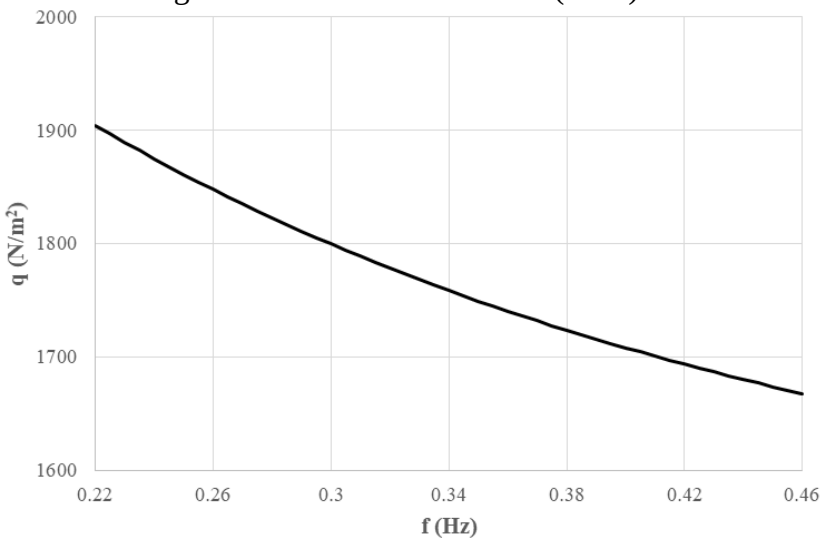

Source: elaborated by the author

Table 6 – External pressure factor c_{pe} for cylindrical structure with circular cross-section

α	External pressure factor for smooth surface	
	$\frac{h}{d} = 10$	$\frac{h}{d} \leq 2.5$
0°	+1.0	+1.0
10°	+0.9	+0.9
20°	+0.7	+0.7
30°	+0.35	+0.35
40°	0	0
50°	-0.7	-0.5
60°	-1.2	-1.05
70°	-1.4	-1.25
80°	-1.45	-1.3
90°	-1.4	-1.2
100°	-1.1	-0.85
120°	-0.6	-0.4
140°	-0.35	-0.25
160°	-0.35	-0.25
180°	-0.35	-0.25

Source: ABNT NBR 6123 (2013).

For the external wind pressure distribution on a cylindrical building, one must use the values for external pressure factor c_{pe} present in Table 6, which depends on the tower height and diameter (*d*). Those values are applied for above the critical region flow, i.e., for Reynolds number higher than 4.20 x 10^5 and perpendicular wind flow to the cylinder axis. Intermediate values may be obtained using linear interpolation.

3.1.3 Turbine loads

Turbine loads are determined by the manufacturers based on a specific Wind environment for a specific turbine, but these loads are considered as trade secrets protected by copyright, therefore are not freely available. Turbine loads consist of the transference of the head mass and wind pressure on the blades to the top of the tower, being the largest loads imposed on the tower and are extremely complex to determinate.

Zyl (2014) used the loads obtained from a study done by Berger-Abam engineers for the National Renewable Energy Laboratory, obtained by using the Computational Fluid Dynamics, for the turbine which specifications are listed in Table 7.

Table 8 gives the loads obtained by the NREL for two IEC wind conditions: EWM and EOG. In the former is used a 59.5 m/s for the 3 seconds gust wind speed and in the latter is 35.1 m/s.

Table 7 – 3.6 MW turbine specifications

Power output	3.6 MW
Rotor speed	13.2 rpm
Rotor diameter	108.4 m
Head mass (including nacelle, hub and blades)	314912 kg
Hub height	100 m
IEC class	IIB

Source: LaNier (2005).

Table 8 – 3.6 MW turbine loads

	Thrust force (kN)	**Overturning moment (kNm)**	**Axial force – causing tower compression (kN)**	**Torsional moment – about tower longitudinal axis (kNm)**
EWM	1086	16767	3155	5961
EOG	1199	9913	3129	1597

Source: LaNier (2005).

3.2 Load factors and load combinations

Loads on the tower can be classified into two categories: dead loads and live loads (GAMA, 2015). Wind loads acting on the turbine and directly on the tower have the same origin and they are classified as live loads. Self-weight and prestressing loads are classified as dead loads. The following section describes the load factors and load combinations used in this work.

3.2.1 Zyl's model

ASCE and IEC specify different partial load factors to wind load, 1.6 and 1.35, respectively. As it was done by Zyl (2014), the direct wind pressure on the tower is calculated according to ASCE recommendations, so the factor of 1.6 is used for that load. However, the turbine loads are usually evaluated according to the IEC (2005), thus the partial load factor of 1.35 is used for the wind-induced turbine loads.

For the serviceability limit state, the wind turbine must be operating under normal wind conditions, therefore the EOG model (that simulates an extreme condition with a reoccurrence period of 1 year) is being used for this case, since it is the only operational wind model for which turbine loads are available. Using the EOG model will lead to an uneconomical design, since it greatly overestimates the normal operation loads of the turbine. Therefore, it is recommended to use 60% of the extreme characteristic load obtained from EOG in the absence of operational load (ZYL, 2014). Thus, for the Ultimate Limit State,

$$0.9\mathrm{D} + 1.6\mathrm{W} + 1.35\mathrm{TWL} + 1.0\mathrm{P} \tag{31}$$

and, for the Serviceability Limit State,

$$0.6(1.0\mathrm{D} + 1.0\mathrm{W} + 1.0\mathrm{TWL}) + 1.0\mathrm{P} \tag{32}$$

where D is the dead load, W is the direct wind load on the tower, TWL is the wind-induced turbine loads and P is the prestressing load.

3.2.2 ABNT NBR 6118:2014

The dead loads act during the whole lifespan of a structure, varying little during that time and it must consider the most unfavorable representative values. According to the ABNT NBR 6118 (2014), dead loads can be classified into two groups: direct and indirect. The live loads are also divided into direct and indirect, the former includes the live load predicted during the construction stages, the wind and water loads, and the latter includes temperature variation and dynamic actions.

The load combinations according to the ABNT NBR 6118 (2014) adopted in this research are, for the Ultimate Limit State

$$1.0\mathrm{D} + 1.4\mathrm{W} + 1.4\mathrm{TWL} + 0.9\mathrm{P} \tag{33}$$

and, for the Serviceability Limit State

$$1.0\mathrm{D} + 0.3\mathrm{W} + 0.3\mathrm{TWL} + 1.0\mathrm{P} \tag{34}$$

The serviceability frequent combination is used to evaluate the cracking opening limit state for the reinforced tower and the cracking initiation limit state for the prestressed tower.

The complete steps on how to properly choose the load factors and combination acoording to the NBR 6118 (2014) is described on annex B.

3.3 Shell element

Quadratic quadrilateral curved shell elements (CQ40S) are used to model the standard concrete tower. Shell elements has been chosen to model the concrete tower because it is a better solution to simulate the tower’s behavior, as it can compute localized stresses, detailed crack patterns and some mode shapes on the free vibration analysis. Such data can be missed during low fidelity model analyses.

DIANA provides two types of shell elements: flat and curved shells. Flat shell elements are a combination of plane stress elements and plate bending elements and there is no coupling between membrane and bending behavior. They are characterized by the following hypotheses: after deformation, the normal of the element plane remains straight, but they do not

have to be perpendicular to the element plane and the displacement perpendicular to the plane does not vary in the direction of the thickness (DIANA FEA 10.3, 2019). This element does not allow reinforcement to be placed in the shell, therefore it cannot be used for a reinforced concrete structure.

Curved shell elements are based on isoparametric degenerated-solid approach, introducing two shell hypotheses: assumes that normal remain straight, but not necessarily normal to the reference surface, so Reissner-Mindlin theory is used for transverse shear deformation and this element assumes that the normal stress component in the normal direction of a lamina basis is forced to zero (DIANA FEA 10.3, 2019). These elements allow reinforcement to be placed into the shell, therefore it was used to model the tower structure.

A normal curved shell element can be triangular or quadrilateral, has five degrees of freedom in each node, two rotations and three translations. In the global *XYZ* directions, the translations are u_x, u_y and u_z, and the rotations are ϕ_x and ϕ_y, in the local *x* and *y* axes respectively in the tangent plane (Figure 26). There are also curved shell elements with a drilling degree of freedom (ϕ_z), but they are not required in this model, therefore a moment force around an axis normal to the surface of the shell will not exist since ϕ_z is not taken into consideration.

Figure 26 – Curved shell element with 8 nodes and its degree of freedom

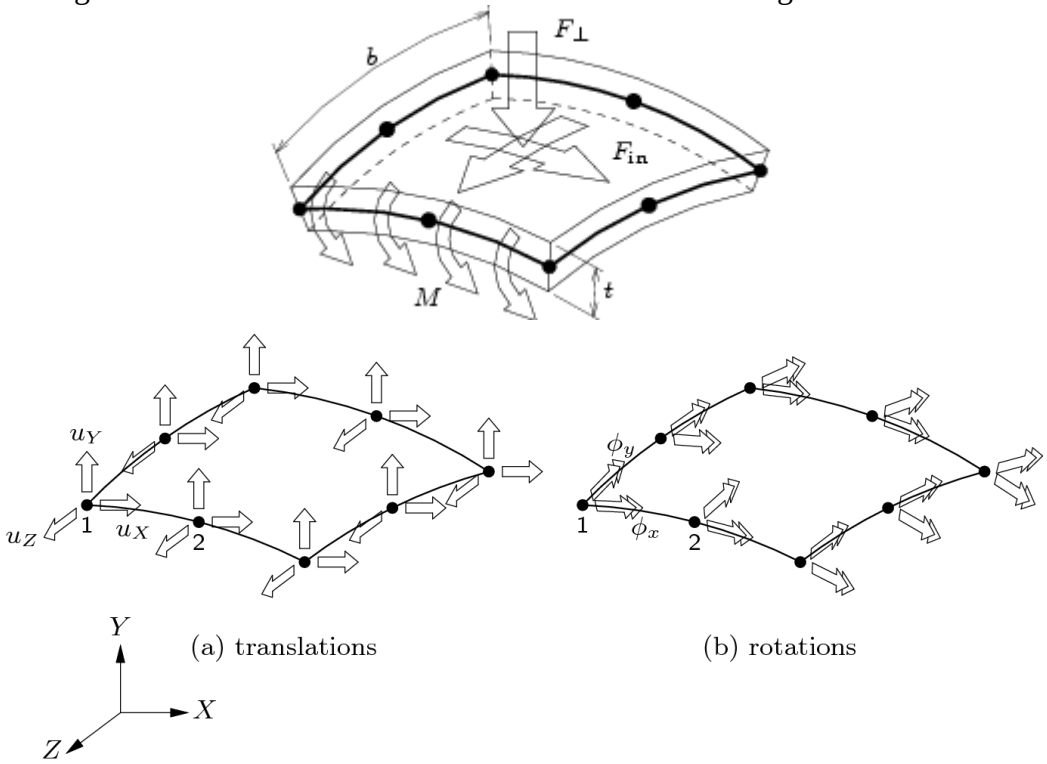

Source: DIANA FEA 10.3 (2019).

A shear correction factor (S = 1.2) is applied on the transverse shear strains γ_{xz} and γ_{yz}, because they are forced to be constant along the thickness, but the actual transverse shearing stresses and strains vary parabolically in the thickness direction. Thus, the correction factor is applied to make sure the constant transverse shear stress yields approximately the same shear strain energy as the actual shearing stress. The in-plane lamina strains ε_{xx}, ε_{yy} and γ_{xy} vary linearly along the thickness direction.

3.3.1 Loads model

The prestressing load and tower self-weight were applied simultaneously to the tower during the first steps of the analysis, then the turbine and tower wind-induced loads were gradually increased during the subsequent steps. The turbine loads are applied to the shell elements of the steel ring at the top of the tower.

The thrust force has been computed as a series of point loads at each node of the ring (Figure 27) and the turbine weight has been applied using two methods for comparison: distributed mass at the top nodes of the ring and as a concentrated mass applied on a node created on the tower axis and with its translations degree of freedom tied using rigid connections to the top nodes of the rings.

Figure 27 – Thrust nodal forces distribution on the steel ring

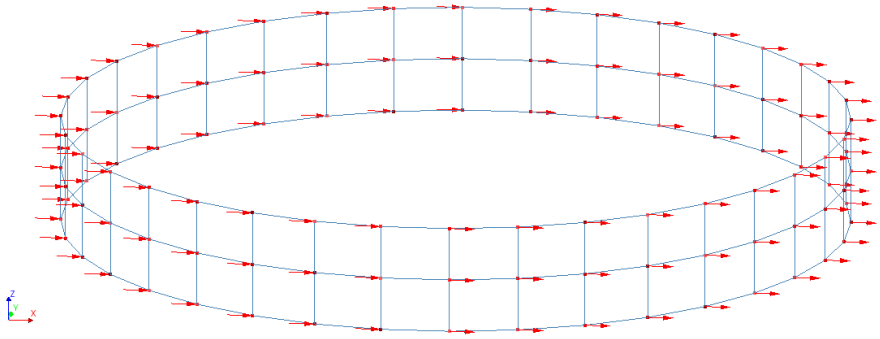

Source: elaborated by the author.

For the overturning moment, a series of equivalent vertical coupled forces have been applied at the top nodes of the steel ring. Considering a linear variation of the forces applied, the modulus of the maximum force on the nodes at the windward and backside of the tower can be obtained through the following equation:

$$F_{max} = \frac{R_c M_{ov}}{\sum_{i=1}^{n} x_i^2} \tag{35}$$

where R_c is the central radius of the ring, M_{ov} is the overturning moment, n is the number of nodes at the top of the ring and x_i is the relative position of the nodes to the center of the ring. The individual forces at each node are obtained by the following equation:

$$F_i = \frac{x_i}{R_c} F_{max} \tag{36}$$

The forces are upward on the nodes at the windward of the tower and downward at the leeward of the tower, as illustrated in Figure 28.

Figure 28 – Overturning coupled forces distribution on the steel ring

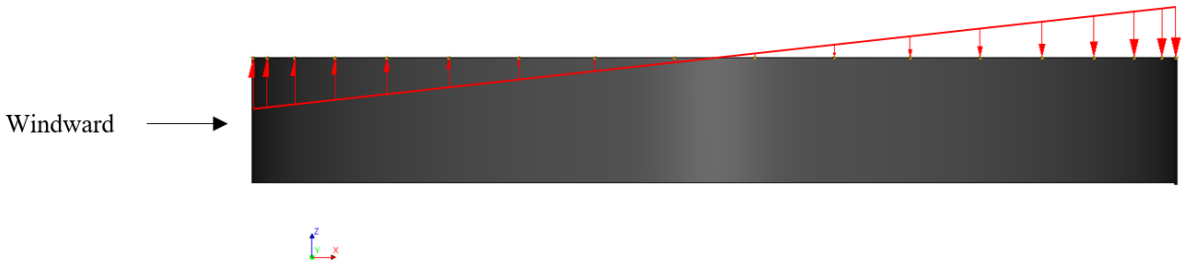

Source: elaborated by the author.

For the torsion moment, a series of equivalent horizontal forces have been applied at the bottom nodes of the steel ring. It is unclear which methods previous researchers adopted for simulating the torsion moment, thus, two methods have been chosen to verify and compare the results. On the first one, which might have been adopted by Zyl (2014), the individual forces at each node are obtained by the following equation:

$$F_T = \frac{M_T}{\sum_{i=1}^{n} R_i} \tag{37}$$

where M_T is the torsion moment and R_i is the lever arm of the nodes to the center of the ring, then the forces are applied to the node as illustrated in Figure 29.

Figure 29 – Equivalent torsion nodal forces distribution for the first method

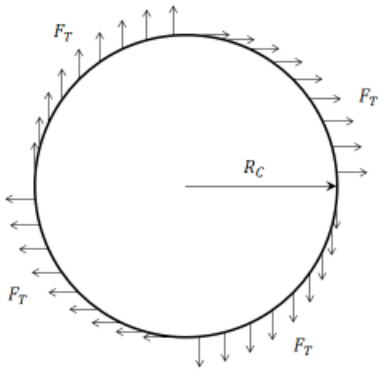

Source: elaborated by the author.

For the second method, the forces are tangential to the ring wall, but split into two perpendicular components. The force magnitude is equal for each node and it can be obtained by using the thin-walled tube average shear stress method:

$$F_T = \frac{M_T s}{2A_m} \tag{38}$$

where s is the arc length of the element and A_m is the mean area enclosed within the boundary of the centerline of the tube's thickness. The vector components depend on the position of each node, as illustrated in Figure 30.

Figure 30 – Equivalent torsion nodal forces distribution for the second method

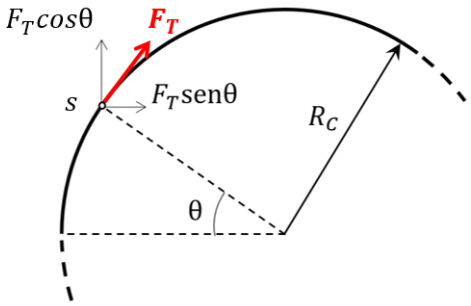

Source: elaborated by the author.

For the wind pressure on the tower, a pressure load is applied on each shell element, as a function of the element centroid's vertical position above the ground as well as its circumferential position from the most windward node following the methodology described in section 3.1, therefore each element forming the tower shell have a unique wind pressure.

Figure 31 – Wind pressure load on the tower shell

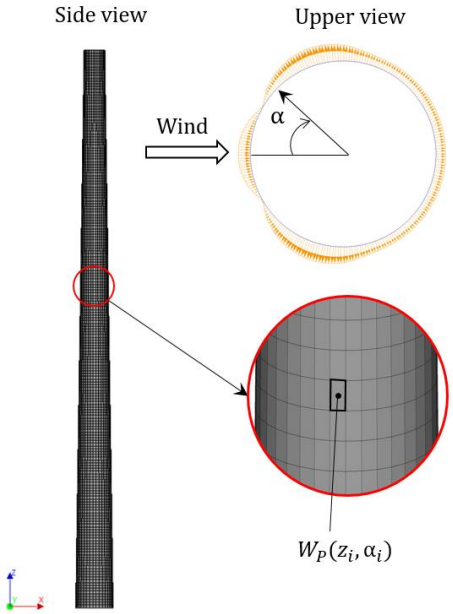

Source: elaborated by the author.

3.4 Cable element

Quadratic cable elements or curved enhanced truss elements (CL12T) are used to model the external unbonded tendons. This type of element is similar to truss elements, but cable elements are curved and have additional degrees of freedom, making it possible to be used for the discrete modeling of prestressing tendons in nonlinear analysis of reinforced concrete (DIANA FEA 10.3, 2019).

Cable elements do not have initial stiffness in the transverse direction by itself, but that can be obtained from surrounding elements or initial stress in geometric nonlinear analysis, such as prestressing the element.

DIANA allows applying initial stress or load in two-dimensional body elements, three-dimensional body elements, plates and shells, beams and trusses, interface elements and embedded reinforcements. It is always defined as the local stress tensor for the respective element type, having six components for solid elements ($\sigma_{xx}, \sigma_{yy}, \sigma_{zz}, \sigma_{xy}, \sigma_{yz}, \sigma_{xz}$) and only one for embedded bar reinforcement or cable elements (σ_{xx}). It is also defined in the local coordinate system of the element or reinforcement.

The cables can be anchored at any point along with the height of the tower. A simple method to represent the anchorage is to apply rigid connections on every translation at the top and bottom of the cables to the tower wall. Another method to simulate the anchorage and properly distribute the prestress load across the concrete section on the model is to insert a rigid

disc with no mass using shell element across the tower section at anchorage height (Figure 32). The cables which are not anchored on the disk must have all degrees of freedom of the nodes that coincide with the disc's nodes disconnected from each other. Both methods are used in this study.

Figure 32 – Rigid disc

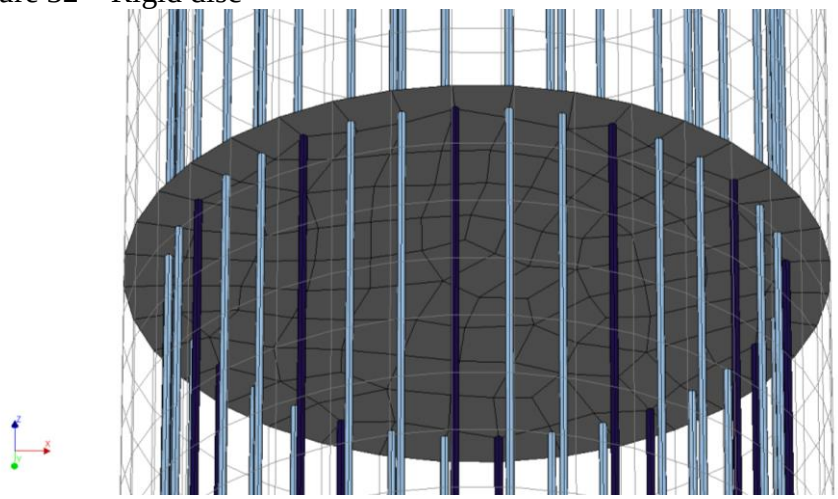

Source: elaborated by the author.

Rigid connections at the transversal directions must be applied on the cables nodes at least every one-third of the tower height to simulate the deviators and make sure the tendons do not touch the inside of the wall, thus making them follow a polygonal line.

Cables have *x, y* and *z* axes for displacements in the nodes, which are parallel to the global *XYZ* axes for three-dimensional application. They also have additional displacement degrees of freedom compared to the regular truss elements, having displacements in all model *XYZ* directions for each node. A tangential direction $\hat{x}$ is used to orient the strains ε_{xx} and stresses σ_{xx} in the cable element. The three-dimensional cable elements' characteristics (CL9TR) are illustrated in Figure 33.

Figure 33 – Three-dimensional cables

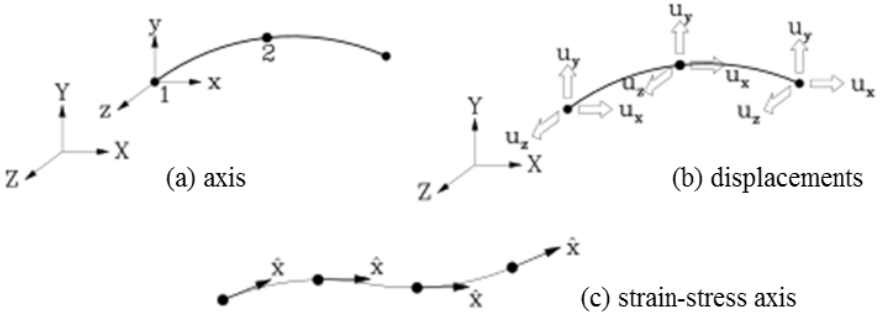

Source: DIANA FEA 10.3 (2019).

3.5 Reinforcing element

For the reinforcing steel elements in the tower wall, DIANA offers two different types for curved shells: bar and grid reinforcing elements.

The bar element models individual bars adding stiffness only in the axial direction of the bar. This element is guided by the location points of the particles that are embedded in the shell and define the curvature of the bar (Figure 34).

DIANA evaluates the numerical integration of each particle of the reinforcement separately using the isoparametric ξ axis, in the integration points (Δ) it determines an $\hat{x}$ axis tangential to the bar axis, which orients the strains ε_{xx} and stresses σ_{xx} that are coupled to the degrees of freedom of the mother element.

Figure 34 – Bar reinforcement in curved shell element

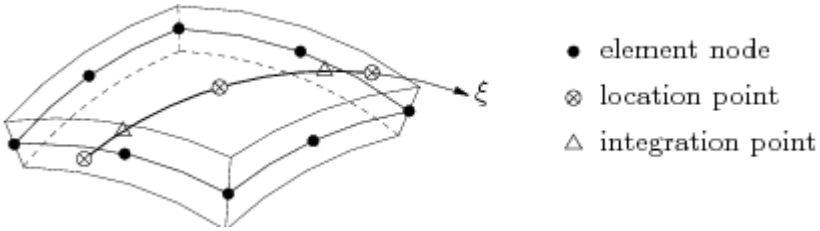

Source: DIANA FEA 10.3 (2019).

The grid element, or plane-shaped reinforcement grids, uses an equivalent thickness method, which calculates the equivalent thickness of the reinforcing bars over a unit area and it can provide stiffness in two orthogonal directions. The total area of the grid is considered divided into several particles that contributes to the stiffness of the element that embeds it, which is called the mother element. Two-dimensional elements may be fully or partly covered by one or more particles of the reinforcement. The location of the grid particle in the element is determined by location points, which must be within the thickness domain of the element (Figure 35). The numerical integration is done for each particle of a reinforcement grid separately and the mother element determines the number of integration points.

Figure 35 – Grid reinforcement in curved shell element

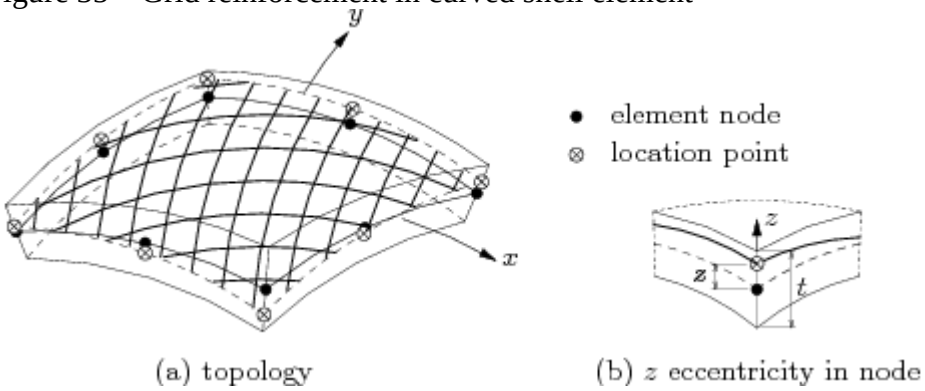

Source: DIANA FEA 10.3 (2019).

To orient the x and y directions of the grid, a $\bar{x}$ axis must be specified as vector components in the model *XYZ* coordinate system. The $\bar{x}$ axis can't be perpendicular to the plane of the grid, since the software uses the specified axis to set up the real x axis, by creating a z axis perpendicular to the grid plane, then it creates $y \perp z\bar{x}$ and $x \perp yz$ (Figure 36).

Figure 36 – Axes of reinforcement grid

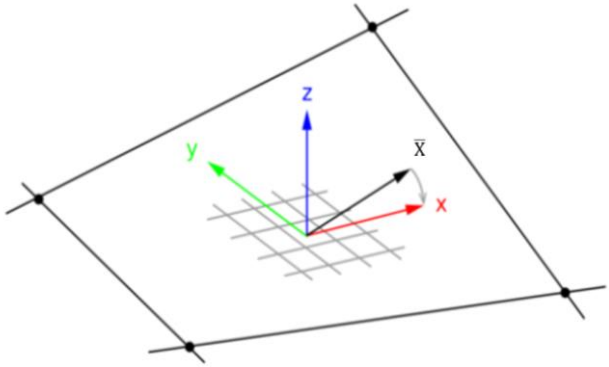

Source: DIANA FEA 10.3 (2019).

Standard reinforcement elements do not have their own degrees of freedom, which means the displacement and strains of the reinforcing element are fully coupled (perfect bond) to that of the element in which it is embedded. The conditions for a grid element to be embedded in a curved shell element are that it must intersect one or two element edges, but none of them more than once and the location points must be inside the shell element thickness.

Another characteristic of embedded reinforcement is that DIANA ignores the space occupied by it, which means the mother element neither diminishes in stiffness, nor in weight and the reinforcement does not contribute to the weight of the element (DIANA FEA 10.3, 2019).

Two layers of grid elements are used to model the reinforcement in the tower, with the respective horizontal and vertical equivalent thickness in each layer, both kept constant throughout the height of the tower. Zyl (2014) adopted bar elements and kept the number of bars constant throughout the height, leading to a 137% increase on the vertical reinforcement ratio on the top in comparison to the bottom of the tower for the case study, whilst the grid element with constant equivalent thickness increased only 33%.

That strategy was adopted to simplify the FE model, since in practice the bar diameter decrease with height. This is done to account for the bending moment decreasing with height. The reinforcing layout of the concrete tower can be observed in Figure 37, where two vertical layers of steel are placed inside the wall and two layers of horizontal steel are placed aside each vertical layer. For post-tensioned towers, the normal reinforcing layout is still used, but the percentage of vertical steel is reduced (Zyl, 2014).

Figure 37 – Reinforcement layout of concrete tower

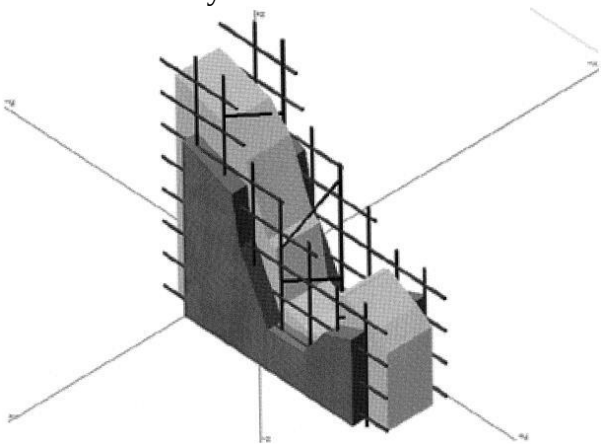

Source: Zyl (2014).

3.6 Materials

DIANA offers an array of predefined models to simulate the material behavior. A material such as concrete behaves very differently in tension and compression, therefore the concrete's material behavior is divided into concrete failing in tension (cracking) and failing in compression (crushing).

To simulate the concrete's behavior in tension, a total strain based smeared cracking model is used in DIANA. When the tensile strength is exceeded a significant material nonlinearity happens on the concrete, which is due to crack formation. Cracking is a combination of tension softening, tension cut-off and shear retention (DIANA FEA 10.3, 2019).

This model smear out or average the crack width over an element, which is different from a discrete cracking model wherein a physical gap occurs by two or more elements losing contact. The total strain of this model is decomposed into a crack strain component and an elastic strain component:

$$\varepsilon^{Total} = \varepsilon^{Elastic} + \varepsilon^{Crack} \tag{39}$$

When the principal tensile stress exceeds the maximum tensile strength condition, a crack is formed. That process generates a loss of tensile strength of the material, which can be either reduced to zero immediately or it can gradually decrease to zero, the latter is known as tension softening and is governed by fracture energy (ZYL, 2014).

It is possible that if the stress in the crack is reversed, then the crack will close and the material will maintain its full compressive strength, this can be done by using a rotating crack model (RCM) that reorients the crack direction, making it so that it will always be in the same direction as the principal stress direction. Although the compressive strength is maintained in this case, the tensile strength is still lost, reopening the crack as soon as tensile stresses reappear. DIANA offers various predefined tension softening behavior for total strain models, the exponential curve is the one chosen for the FEM in this study (Figure 38-f).

Figure 38 – Predefined tension softening curves for Total Strain Crack model

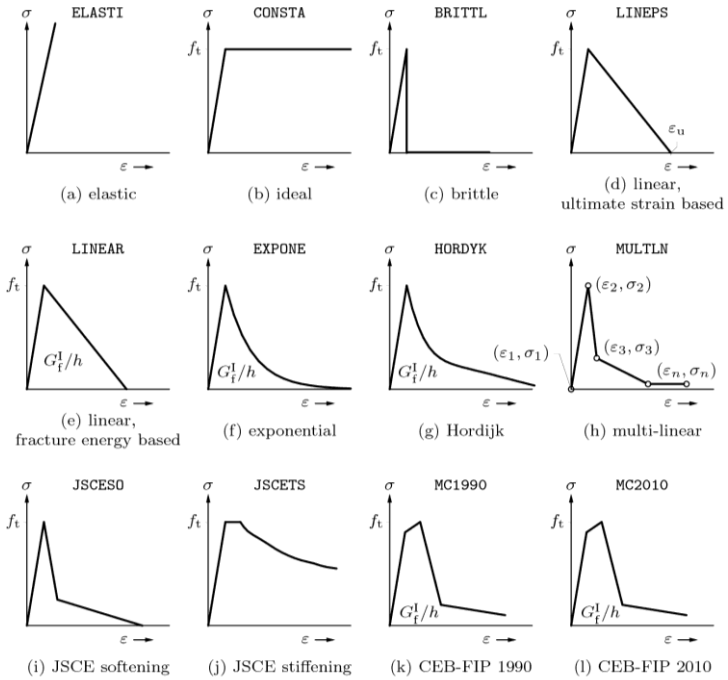

Source: DIANA FEA 10.3 (2019).

Below the tensile strength of the concrete (f_t) the material presents linear elastic strain. Beyond the peak, the stress-strain curve presents an exponential softening behavior caused by the formation of cracks and it is governed by the concrete fracture energy (G_f) and the crack bandwidth (h). The term tension softening is a relationship between tensile stress and crack bandwidth in the zone of fracture in concrete, characterizing the post-ultimate behavior of the concrete in tension (RAFI & NADJAI, 2007). The area below the softening section of the tensile stress-strain curve equals to G_f^I/h. The concrete behavior on tension adopted in this research is described by:

$$\sigma(\varepsilon) = \begin{cases} E_C\varepsilon & if\ 0 < \varepsilon < \varepsilon_c \\ f_t e^{\beta\left(1-\frac{E_C}{f_t}\varepsilon\right)} & if\ \varepsilon \geq \varepsilon_c \end{cases} \tag{40}$$

where E_C is the modulus of elasticity of concrete, ε_c is the strain where the tensile strength is reached and β is the curve fitting factor and it is given by the following equation:

$$\beta = \frac{hf_t^2}{E_C G_f} \tag{41}$$

To simulate the concrete's behavior in compression, a plasticity model is used in DIANA. Between an elastic and plastic material behavior, the main difference in a macroscopic level is that an elastic behavior will suffer no permanent deformation, but when the material has a plastic behavior it will suffer permanent or irreversible deformations. When a material shows irreversible deformations, the mathematical formulation of the plasticity behavior can be applied and for small strains, the total strain can be decomposed into a plastic part and an elastic part.

When the concrete is reaching its crushing strength, the formulation of plasticity can be used, since the concrete becomes plastic when the principal stress violates the compressive elastic limit of the material, which in turn makes the concrete exhibit softening or hardening behavior, depending on the type of the concrete used. There are various predefined compressive stress-strain curves for the total strain model available in DIANA to describe the material softening or hardening behavior, which is illustrated in Figure 39.

The concrete used is a High Strength Concrete (HSC), a known brittle material whose stiffness is reduced rapidly when the principal stress reaches the maximum compressive

strength. Thus, the Thorenfeldt model (Figure 39-b) was chosen to represent the concrete in compression since it is able to accurately describe this behavior.

Figure 39 – Predefined compressive stress-strain curves for Total Strain model

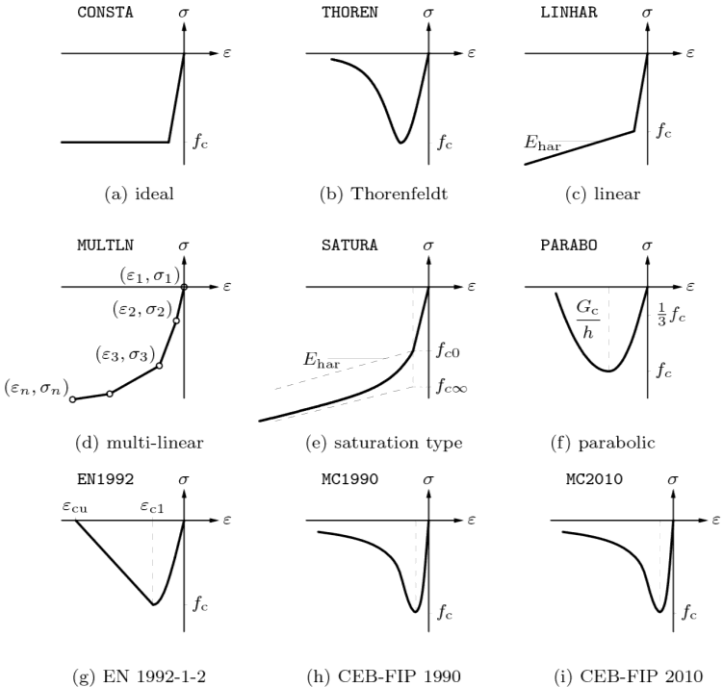

Source: DIANA FEA 10.3 (2019).

The Thorenfeldt compression curve is described by (THORENFELDT *et al.*, 1987):

$$\sigma(\varepsilon) = -f_c \frac{\varepsilon}{\varepsilon_c} \left(\frac{n}{n - \left(1 - \left(\frac{\varepsilon}{\varepsilon_c}\right)^{nk}\right)} \right) \tag{42}$$

where f_c is the compressive strength of the concrete, ε_c is the strain at the peak of the curve, n is the curve fitting factor and k is the post-peak decay term, which, according to Collins & Mitchell (1991), are given by:

$$n = 0.8 + \frac{f_c}{17} \tag{43}$$

$$k = \begin{cases} 1 & if\ \varepsilon_c < \varepsilon < 0 \\ 0.67 + \dfrac{f_c}{62} & if\ \varepsilon \leq \varepsilon_c \end{cases} \tag{44}$$

For the reinforcing steel, DIANA offers three main models to describe its stress-strain behavior, namely: linear elasticity, ideal plasticity and hardening plasticity. The ideal plasticity model (Figure 40-b) is used in this study, therefore the hardening will not be considered in the model, since the material needs to suffer large strains before hardening happens, this will lead to large deformation in the structure.

Figure 40 – Reinforcing steel material models

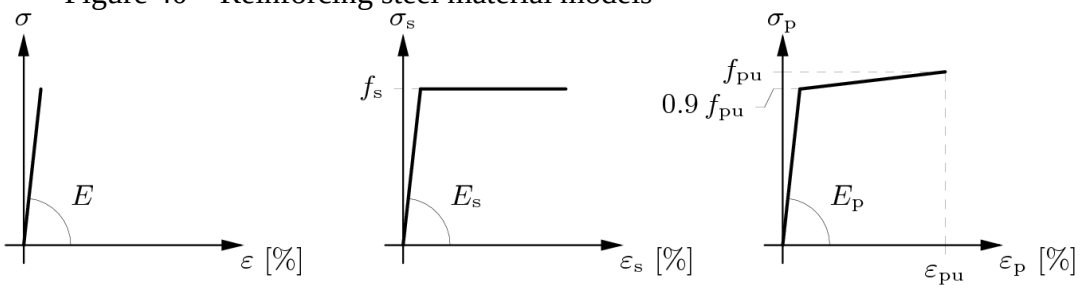

(a) linear elasticity (b) ideal plasticity (c) hardening plasticity

Source: DIANA FEA 10.3 (2019).

For prestressing steel, DIANA allows choosing a material model for either linear plasticity or hardening plasticity. It is recommended to use an elastoplastic material model with hardening to approximate the stress-strain relationship, since that relationship is characterized by the definition of the 0.1% proof stress, steel's Young's modulus (E_p), ultimate tensile strength (f_{pu}) and strain at maximum force (ε_{pu}). The bilinear curve for prestressing steel is described on the following equation:

$$\sigma_p(\varepsilon_p) = \begin{cases} E_p \varepsilon_p & if\ 0 < \varepsilon_p \leq \dfrac{0.9 f_{pu}}{E_p} \\ f_{pu}\left(0.9 + 0.1\dfrac{\varepsilon_p E_p - 0.9 f_{pu}}{\varepsilon_{pu} E_p - 0.9 f_{pu}}\right) & if\ \dfrac{0.9 f_{pu}}{E_p} < \varepsilon_p \leq \varepsilon_{pu} \end{cases} \quad (45)$$

It is important to mention that no material safety factor has been applied for the ULS analysis, thus, the characteristic strength has been used instead for research purposes only.

3.7 Foundation and soil-structure interaction

In general, wind towers have been modeled without foundation and fixed at the base. This work studies the effect of the foundation and soil-structure interaction on the tower's behavior, at first the boundary conditions restraint the rotations in two axes and displacement

in all three axes at the base of the tower without foundation, then solid elements are used to model the foundation and a simplified method to simulate the soil-structure interaction is adopted.

The adopted finite element to simulate the foundation is the quadratic pyramid (CPY39), which is a thirteen-node isoparametric solid (Figure 41). This element has 13 nodes with 3 degrees-of-freedom.

Figure 41 – The quadratic pyramid element

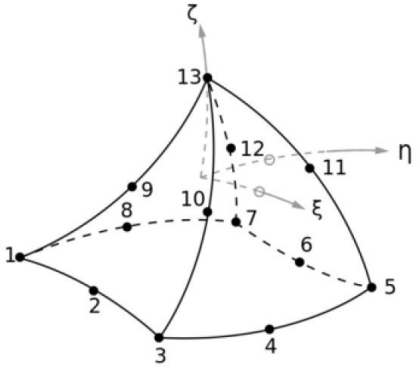

Source: DIANA FEA 10.3 (2019).

Since the foundation is a solid element and the tower is simulated with shell elements, those elements nodes must be connected to each other. This research adopted the automatic tying method, which the nodes of the connected solid elements which are on the thickness vectors *t* of the shell are tied automatically to the shell's degrees of freedom (Figure 42).

Figure 42 – Automatic tying between shell and solid

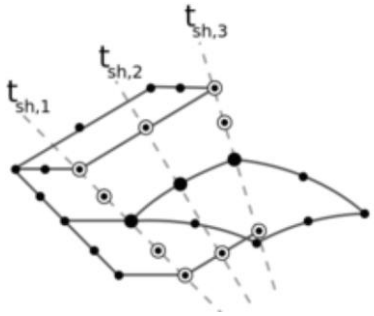

Source: DIANA FEA 10.3 (2019).

The soil-structure interaction is based on the rocking mode spring presented in Equation (3), as it is the dominant mode for the structure (ZYL, 2014), and it is a simplified model that can only be applied if the foundation is sufficiently rigid. The present work adopted

a three-dimensional model, therefore the rotational spring for the rocking mode must be transformed into a series of equivalent vertical translational springs to be applied on the soil-foundation interface.

The linear translational springs have a constant stiffness $K_v = \bar{K}_v s$, where $\bar{K}_v$ is the spring stiffness over an unit arc length and s is the element length. The springs are applied at the outside edge of the foundation, represented as the yellow dots illustrated in Figure 43–a.

Figure 43 – Discrete springs method: a) springs location, b) spring stiffness, c) spring forces and symmetry

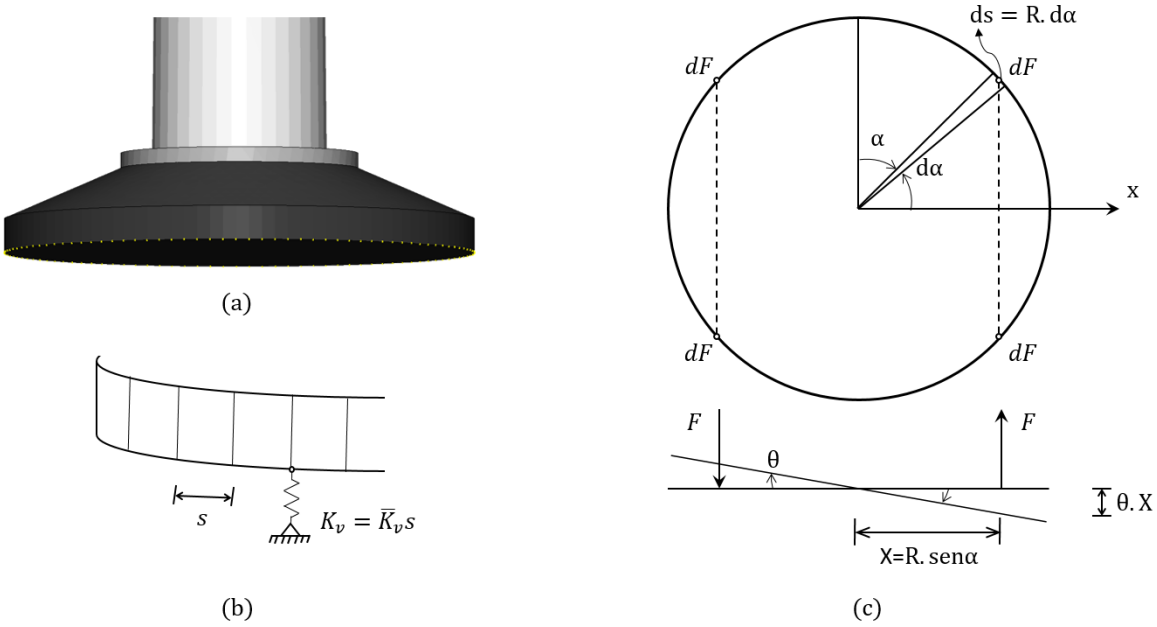

Source: elaborated by the author.

According to Hooke's law, the force on the springs can be obtained from the following equation:

$$dF = \bar{K}_v R^2 \theta sen\alpha \, d\alpha \tag{46}$$

where R is the foundation radius, θ is the foundation rotation and α defines the spring location. By using the symmetry, one can obtain the resulting momentum:

$$M = \int_0^{\pi/2} 4\bar{K}_v R^3 \theta sen^2\alpha \, d\alpha \tag{47}$$

$$M = \pi \bar{K}_v R^3 \theta \tag{48}$$

The momentum from a rotational spring on a bar must be equal to the momentum obtained from the discrete translational spring method, thus:

$$M = \pi \bar{K}_v R^3 \theta = \frac{8GR^3\theta}{3(1-\nu)} \tag{49}$$

$$\bar{K}_v = \frac{8G}{3\pi(1-\nu)} \tag{50}$$

3.8 Mesh and element type

The mesh size of a finite element model is an important factor in the accuracy and efficiency of the model. A smaller element size will most likely generate more accurate results, but it will increase computational time and the maximum element size must be limited to prevent a snap-back in the constitutive model of the concrete, which is explained in this section.

The tensile softening behavior of the concrete on the constitutive level is related to the Mode-I fracture energy, which will be released in an element if the tensile strength is violated and deformations concentrate inside the element. If the element sizes are large enough, the concept of fracture energy which has been assumed is no longer satisfied.

The Mode-I fracture energy G_f^I can be described as the area under the softening section of the material stress-strain curve, therefore:

$$G_f^I = h \int_{\varepsilon^{cr}=0}^{\varepsilon^{cr}=\infty} \sigma^{cr}(\varepsilon^{cr}) d\varepsilon^{cr} \tag{51}$$

in which h represents the equivalent length or crack bandwidth, which depends on the element type: for linear two-dimensional elements, one has $h = \sqrt{2A}$ and for higher-order two-dimensional elements $h = \sqrt{A}$, where A is the element area (HENDRIKS, DE BOER & BELLETTI, 2017). The relation between the crack stress σ^{cr} and the crack strain ε^{cr} in the normal direction can be written as:

$$\sigma^{cr}(\varepsilon^{cr}) = f_t y\left(\frac{\varepsilon^{cr}}{\varepsilon_{ult}^{cr}}\right) \tag{52}$$

Figure 44 – Exponential relationship between crack stress and crack strain

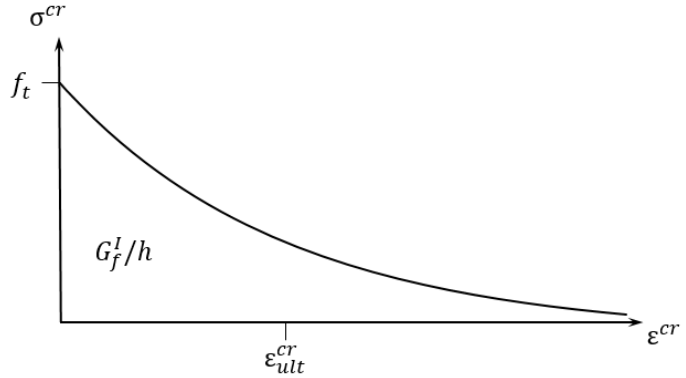

Source: elaborated by the author.

where ε_{ult}^{cr} is the ultimate crack strain and $y\left(\frac{\varepsilon^{cr}}{\varepsilon_{ult}^{cr}}\right)$ represents the softening curve. Taking $x = \frac{\varepsilon^{cr}}{\varepsilon_{ult}^{cr}}$ and substituting Equation (52) into Equation (51), one obtains:

$$\varepsilon_{ult}^{cr} = \frac{G_f^I}{h f_t} \frac{1}{\int_{x=0}^{x=\infty} y(x)dx} \tag{53}$$

the ultimate crack strain is assumed to be constant during the analysis and it is considered to be an element-related material property.

A snap-back in the constitutive model occurs if the absolute value of the initial slope, which is the greatest tangent stiffness of the tension softening diagram, is greater than the Young's modulus of the material, therefore one must observe:

$$\left.\frac{d\sigma^{cr}}{d\varepsilon^{cr}}\right|_{\varepsilon^{cr}=0} \geq -E \tag{54}$$

which can be reorganized as:

$$\varepsilon_{ult.min}^{cr} \geq -\frac{f_t}{E}\left.\frac{dy}{dx}\right|_{x=0} \tag{55}$$

this is the minimum value of the ultimate crack strain. If this condition is violated, a reduction of the tensile strength will occur, increasing the material ductility.

The reduction of the tensile strength is justified because the probability of a reduced strength is larger if the sampling area is larger. Therefore, the tensile strength will be reduced in larger elements, because stress concentrations are not captured within these elements (HENDRIKS, DE BOER & BELLETTI, 2017).

For the exponential stress-strain diagram, the ultimate crack strain is given by Equation (56) and the minimum value of ultimate crack strain is given by Equation (57).

$$\varepsilon_{ult}^{cr} = \frac{G_f^I}{h f_t} \tag{56}$$

$$\varepsilon_{ult.min}^{cr} = \frac{f_t}{E} \tag{57}$$

Substituting Equation (56) into Inequality (54) and reorganizing, one obtains the reduced tensile strength for the exponential diagram in case the condition on Equation (54) is violated:

$$f_{t.red}^2 = \frac{G_f^I E}{h} \tag{58}$$

To avoid the tensile strength reduction, the maximum element size must be limited, the maximum element area can be obtained reorganizing Equation (58):

$$A_{max} = \begin{cases} \frac{1}{2}\sqrt{\frac{G_f^I E}{f_t^2}} & for\ linear\ 2D\ elements \\ \sqrt{\frac{G_f^I E}{f_t^2}} & for\ higher-order\ 2D\ elements \end{cases} \tag{59}$$

The tower chosen for the application is discretized with 200 vertical divisions and 36 divisions in the circumferential direction, totaling 7200 shell elements, based on the mesh used by Zyl (2014). It is important to mention that a less refined mesh has been analyzed (36 circumferential and 100 vertical divisions) and has provided similar results for the tower's global behavior. Table 9 gives the element size at various vertical coordinates.

Table 9 – Element size

Vertical coordinate (m)	Element area (m^2)	Maximum element area (m^2)	
		Linear elements	Quadratic elements
0 m	0.292	0.197	0.394
50 m	0.227		
100 m	0.161		

Source: elaborated by the author.

Therefore, using linear elements will lead to a reduction of the concrete tensile strength in most elements of the tower, because stress concentrations will not be captured with precision within these elements. The element sizes are kept the same for linear and quadratic element for comparison purposes, as it was the same size adopted by Zyl (2014).

Element dimensions are similar to the 0.5 m by 0.5 m elements adopted by Tomczak (2021), but more refined than the one adopted by Kenna & Basu (2015), which used only 200 elements for a similar tower.

The prestressing tendons are composed of 16 cable elements each, to properly represent the eigenmodes that the tendons might suffer during the analysis and allow the deviators to be applied.

As for the foundation, 10912 solid pyramid elements has been used to properly represent the structure's geometry (Figure 45).

Figure 45 – Foundation mesh

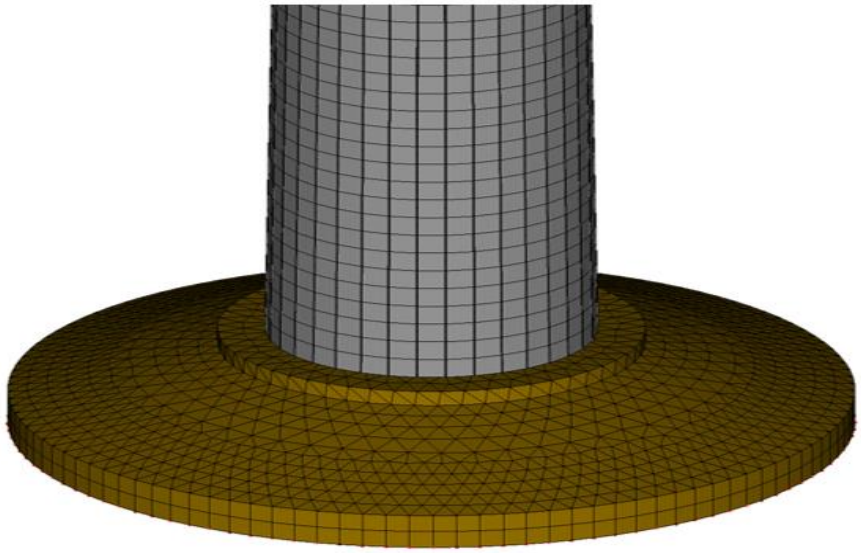

Source: elaborated by the author.

3.9 Fundamental frequency

A static nonlinear analysis is used for the FEM structural strength analysis, with geometric and material nonlinearity being considered. The fundamental frequency of the tower is evaluated using an eigenvalue analysis.

In DIANA, the first step is to model the uncracked tower. That is done by solving an eigenproblem, adding the geometric stress-stiffness matrix $\mathbf{K_G}$ with initial stresses specified, which is important for prestressed structures.

$$(\mathbf{K} + \mathbf{K_G})\phi = \omega^2 \mathbf{M}\phi \tag{60}$$

where ω is the natural angular speed of the generalized eigenproblem, $\mathbf{K}$ is the stiffness matrix, ϕ is the free vibration modes and $\mathbf{M}$ is the mass matrix.

The second step is to use a nonlinear analysis involving a Newton-Raphson iteration method. Then, the fundamental frequency of the tower in the cracked state is computed using the tangent stiffness of the tower, which has been constructed in the previous steps.

The nonlinear stiffness free vibration analysis applies the tangential stiffness matrix $\mathbf{K_T}$ from a previously executed nonlinear analysis and solves the eigenproblem:

$$\mathbf{K_T}\phi = \omega^2 \mathbf{M}\phi \tag{61}$$

The cyclic frequency *f*, expressed in hertz, is obtained by using the following equation:

$$f = \frac{\omega}{2\pi} \tag{62}$$

4 APPLICATION

This chapter presents the tower used for the application of this study, describing its geometry, material properties and foundation. The tower is based on the reinforced concrete tower in LaNier (2005) and Zyl (2014), which is a tapered tube concrete tower. The reinforced concrete tower has been analyzed by Barroso Filho (2018) and an optimal solution has been found by Duarte (2019) using a beam model. For the present study, the structure has been adapted for a prestressed application with the addition of external tendons, which is similar to the methodology adopted in Lana *et al*. (2021) and Tomczak (2021).

4.1 Wind turbine tower geometry

The maximum bending moment and shear force are located at the bottom of the tower and reduce to the top. Thus, the tower has a tapered tube shape, with the diameter and wall thickness linearly reducing with height, saving unnecessary weight and cost.

The tower model has a steel ring at the top that prevents ovalization of the tower, representing the interaction with the nacelle, and it is used to apply the turbine loads, being an efficient method to model the effect that the steel turbine structure (nacelle) has at the top of the tower. The steel ring has a cylinder shape with the same diameter and wall thickness as the tower wall at the top, with a height of 0.5 m. Table 10 shows the bottom, center and top diameter and wall thickness, varying linearly with the height.

Table 10 – Tower dimensions

	H = 0 m	**H = 50 m**	**H = 100 m**
Outside diameter (m)	7.10	5.55	4.00
Wall thickness (m)	0.40	0.35	0.30

Source: LaNier (2005).

The model is divided into four sections, to properly restrain the cables to the tower wall, avoiding that the tendons at the leeward touch the inside of the tower (Figure 46).

Figure 46 – Tower FEM schematization

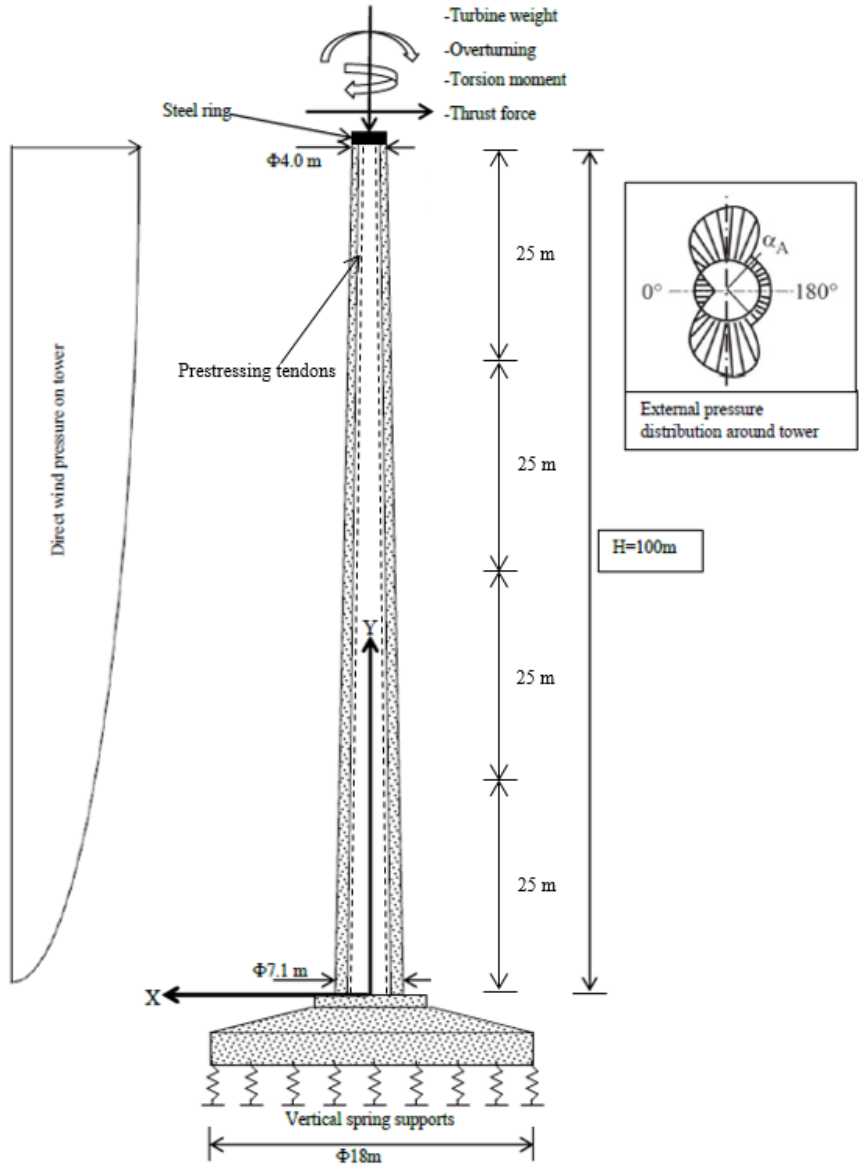

Source: Zyl (2014, adapted).

4.2 Materials properties and turbine characteristics

The 2010 edition of the Model Code is used to evaluate the material properties of the High Strength Concrete adopted in the tower model. The chosen strength class of the HSC is the C80/95, the same as the concrete of Zyl (2014) tower, which has a characteristic cube compressive strength ($f_{ck,cube}$) of 95 MPa and the characteristic cylinder compressive strength (f_{ck}) of 80 MPa.

The first concrete property needed to evaluate is the mean compressive strength, which can be obtained by the following equation (CEB-FIB, 2010):

$$f_{cm} = f_{ck} + \Delta f \tag{63}$$

where Δf = 8 MPa.

Following next the tensile strength for normal weight concrete can be evaluated using the characteristic compressive strength, by using the following equation for concrete grades above C50 (CEB-FIB, 2010):

$$f_{ctm} = 2.12 ln\big(1 + 0.1(f_{ck} + \Delta f)\big) \tag{64}$$

where f_{ck} is the characteristic compressive strength in MPa. Then the lower and upper bound values of the characteristic tensile strength are required (CEB-FIB, 2010):

$$f_{ctk,min} = 0.7 f_{ctm} \tag{65}$$

$$f_{ctk,max} = 1.3 f_{ctm} \tag{66}$$

The fracture energy of the concrete, G_F (N/m), is then evaluated, which is defined as the energy required to propagate a tensile crack of unit area, using the following equation for ordinary normal weight concretes (CEB-FIB, 2010):

$$G_F = 73 f_{cm}^{0.18} \tag{67}$$

where f_{cm} is the mean compressive strength in MPa.

The tangent modulus of elasticity at the origin of the stress-strain diagram, or the modulus of elasticity E_{ci} in MPa at a concrete age of 28 days can be estimated from the characteristic compressive strength, using the following equation for normal weight concretes (CEB-FIB, 2010):

$$E_{ci} = E_{c0} \alpha_E \left(\frac{f_{ck} + \Delta f}{10} \right)^{1/3} \tag{68}$$

where E_{c0} = 21.5 GPa and the coefficient α_E varies depending on the aggregate used, for quartzite aggregates the value is 1.0, for different types of aggregates the values can be obtained in the Model Code CEB-FIB (2010).

According to CEB-FIB (2010), for the range of stress $-0.6f_{ck} < \sigma_c < 0.8f_{ctk}$ the Poisson's ratio of concrete ν_c has a value between 0.14 and 0.26. The value for Poisson's ratio is estimated at 0.2.

The material characteristics of the HSC in the tower, obtained using the Model Code, are summarized in Table 11.

Table 11 – Concrete properties

f_{ck}	80 MPa
$f_{ck,min}$	3.4 MPa
G_F	163.4 N/m
E_{ci}	44.4 GPa
ν_c	0.2

Source: elaborated by the author.

Table 12 shows the reinforcing steel properties adopted in this research, using ideal plasticity model. It is important to mention that the equivalent thickness of reinforcing is kept constant through the height of the tower based on the reference values, but the sensitivity analysis of the prestressed tower with respect to the vertical reinforcing steel will be evaluated.

Table 12 – Reinforcing steel properties

Density	7850 kg/m³
Modulus of elasticity	200 GPa
Poisson's ratio	0.3
Yield strength	450 MPa
Concrete cover	40 mm
Number of layers (horizontal and vertical)	2
Vertical reinforcing steel	5068 mm²/m per layer
Horizontal reinforcing steel	1636 mm²/m per layer

Source: Zyl (2014).

For the prestressed reinforcement, 56 tendons, symmetrically distributed along the tower main axes, with 12 of the 7-wire low-relaxation prestressing strands each were chosen as

reference values based on the suggestions of LaNier (2005). Table 13 provides the prestressed strand properties.

Table 13 – Prestressed steel properties for 7-wire low-relaxation strands

Strand tensile strength (0.6 in. or 15.25 mm diameter – 7 wire low relaxation strands)	$f_{pu} = 1862$ MPa
Characteristic 0.1% proof stress	$f_{p0.1k} = 1675$ MPa
Nominal strength	$f_{ps} = 1693$ MPa
Effective stress after losses	$f_{se} = 1103$ MPa
Nominal yielding strain (according to Figure 48, for the 270 ksi strand stress-strain curve)	$\varepsilon_{ps} = 0.0086$
Nominal strand area	$A = 140$ mm^2
Elastic modulus	$E_S = 196500$ MPa
Ultimate strain	$\varepsilon_{pu} = 0.035$
Density	$\rho = 7850$ kg/m^3

Source: LaNier (2005, adapted).

The tendons' transversal displacements need to be restrained to the tower wall according to Figure 47. For compatibility with the mesh model, the number of tendons must be the same or a divisor of the number of circumferential divisions made on the tower element grid, maintaining the same total prestressing steel area.

Figure 47 – Tendons to tower restraints

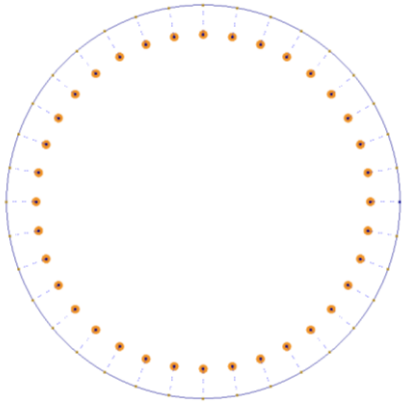

Source: elaborated by the author.

The idealized stress-strain curves for 270 ksi (1862 MPa) 7-wire low-relaxation prestressing strand can be approximated by the following equations (LANIER, 2005):

$$\varepsilon_{ps} \leq 0.0086 \rightarrow f_{ps} = 196500\varepsilon_{ps} \text{ (MPa)} \quad (69)$$

$$\varepsilon_{ps} > 0.0086 \rightarrow f_{ps} = 1862 - \frac{0.27579}{\varepsilon_{ps} - 0.007} \text{ (MPa)} \quad (70)$$

Figure 48 – Idealized stress-strain curve for 270 ksi 7-wire low-relaxation prestressing strand

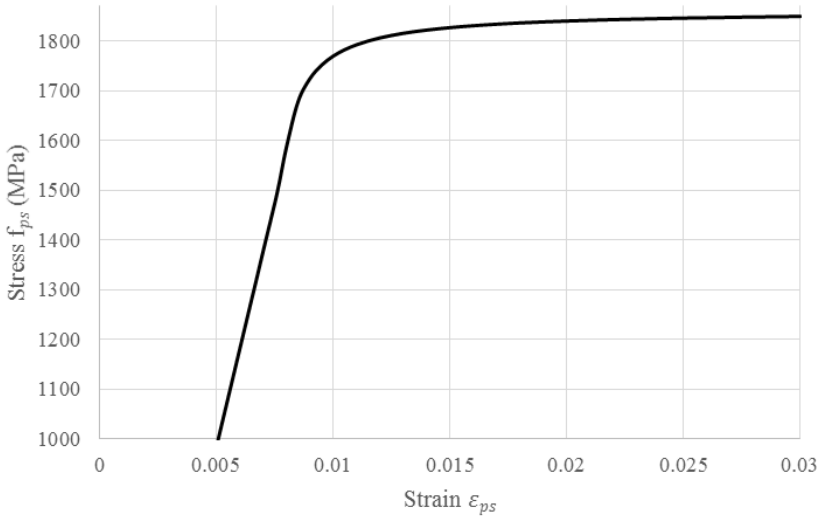

Source: elaborated by the author.

The rigid disc used to simulate the anchorage of some tendons is made of steel (200 GPa modulus of elasticity) and 40 cm thick, to properly distribute the stress from the tendons to the concrete wall. It is important to mention that the disc is only used to simulate the anchorage effects on the concrete. In practice, a more localized study is necessary to determine an adequate anchorage structure for the design.

The working frequency of the turbine being used in this study is given in Table 14.

Table 14 – Working frequency of 3.6 MW turbine

	Operation speed – 1P (rpm)	**1P (Hz)**	**3P (Hz)**	**Working frequency limits**	
				1.1P (Hz)	**2.7P (Hz)**
3.6 MW constant speed	13.2	0.220	0.660	0.242	0.594

Source: Zyl (2014).

5 RESULTS AND DISCUSSION

The results presented in the following sections were obtained for a reinforced concrete tower and a prestressed concrete tower using various configurations by modifying different parameters, such as: element type, circumferential pressure, application models for torsion and thrust load, ring material, turbine mass, vertical reinforcing steel, prestress load, tendons placement, nonlinearity effect, wind and load combination, tendon distribution over the tower height and half-length cables anchorage.

The study for each configuration consists of evaluating: the deflection at the top of the tower, because large deflections will cause the efficiency of the turbine to decrease; the uncracked and after-loading fundamental frequencies, as they are important to determine the tower stiffness reduction that it might suffer from the applied loads and to ensure that the fundamental frequency of the structure does not coincide with the blades' frequencies; wind load for crack initiation in each limit state; the concrete and cable stresses, in some analyses, which is the Cauchy stress at the integration points. Although some results are more important for service limit state, some of them are presented for the ultimate limit state for comparison and research purposes only and discussions are included.

The top horizontal deflections are evaluated at 75% and 100% of the wind load applied for the SLS, and 30% and 100% for the ULS. The 75% and 30% marks are important because it is often when the cracking initiation occurs based on previous researches for this reinforced concrete tower (ZYL, 2014; BARROSO FILHO, 2018; DUARTE, 2019), thus, until this point, the concrete can be modeled like a linear elastic material. As the concrete cracks, the tensile forces then start to get resisted almost exclusively by the steel, causing a reduction in stiffness and an increase in the tower deflection.

Some results obtained in this research were also used as a comparison and to validate the beam model developed by Melo (2021), which is utilized for optimization purposes.

5.1 Reinforced concrete tower

This section presents the results obtained from the reinforced concrete tower FEM analysis. The example chosen was presented in Chapter 4 and all the results are obtained according to the methods discussed in Chapters 2 and 3. The comparison between the results obtained in this research and the ones obtained in previous works is important to determine the

accuracy of the method. The reinforced concrete tower is used to verify and compare several methodological aspects.

Table 15 summarizes the adopted and investigated model configurations during the analysis of the reinforced concrete tower. The Total Langragian method for geometric nonlinearity has been chosen for this research because anisotropic effects of cracking and embedded reinforcements are not handled correctly in Update Lagrangian analysis in DIANA, since the rotations are not accounted for in the current implementation (DIANA FEA 10.3, 2019).

Table 15 – Configurations used in the analysis of the reinforced concrete tower

Description	**Configurations**	
Iterative method	Standard Newton-Raphson	
Geometrical nonlinearity formulation	Total Lagrangian	
Convergence norm	Displacement and force	
Solution method	Parallel direct sparse	
Wind and load combination model	Zyl (2014)	
	Configurations investigated	
Element type	Linear (Q20SH)	Quadratic (CQ40S)
Circumferential pressure distribution	Linear	Quadratic
Torsion load model	Zyl's method	Average shear stress
Thrust load model	Top nodes	All nodes
Turbine mass distribution	Concentrated	Distributed

Source: elaborated by the author.

The standard reinforced concrete tower in analysis has the following configuration, except when stated otherwise: quadratic approximated radial pressure distribution, quadratic elements for the shell model, torsion load applied using the average shear stress method, thrust load applied on all nodes at the steel ring, distributed turbine mass at the top of the ring, fixed base with no foundation included in the model.

To verify the convergence of the FEM, the final solution must be well-converged, therefore the energy variation of each step has to be less than $1x10^{-5}$ and the relative out-of-balance force has to be less than $1x10^{-3}$ (DIANA FEA 10.3, 2019). Both criteria are met for all load steps.

A practical way to verify the FEM accuracy is to compare the applied forces to the FEM reaction forces. The difference for both SLS and ULS are presented in Table 16, which is relatively small, thus, the forces are correctly applied in the FEM.

Table 16 – Difference for reinforced tower equilibrium

Forces	SLS (%)	ULS (%)
Axial force	0.01	0.02
Overturning moment	-0.79	-0.81
Thrust force	-0.61	-0.65
Torsional moment	0.01	0.02

Source: elaborated by the author.

Whenever available, the results of Zyl (2014) and Melo (2021) are presented for comparison and validation.

5.1.1 Circumferential pressure distribution model

The results for the linear and quadratic circumferential pressure distribution approximation models at SLS are presented in Table 17, whereas Figure 49 illustrates the tower top deflection versus wind load for various configurations.

Table 17 – Results for circumferential pressure analysis (SLS)

Source	Configuration		Uncracked frequency		After-loading frequency		Cracking initiation	Top deflection at 75%		Top deflection at 100%	
			Value (Hz)	Diff.[a] (%)	Value (Hz)	Diff.[a] (%)	Value[b] (%)	Value (mm)	Diff.[a] (%)	Value (mm)	Diff.[a] (%)
Zyl (2014)	Shell model		0.445	-	0.241	-	75	168.0	-	549.0	-
Melo (2021)	Beam model		0.449	0.90	0.225	-6.64	88	152.5	-9.23	535.5	-2.46
The present study	Linear pressure	Linear elements	0.440	-1.12	0.215	-10.79	70	154.9	-7.80	657.1	19.68
		Quadratic elements	0.440	-1.12	0.238	-1.24	75	154.5	-8.06	564.4	2.81
	Quadratic pressure	Linear elements	0.440	-1.12	0.217	-9.96	70	154.6	-7.99	647.6	17.96
		Quadratic elements	0.440	-1.12	0.241	0.00	75	154.2	-8.23	553.0	0.72

[a] Comparison to the results obtained from Zyl (2014); [b] Percentage of the total wind load.

Source: elaborated by the author.

Figure 49 – Deflection for circumferential pressure analysis (SLS)

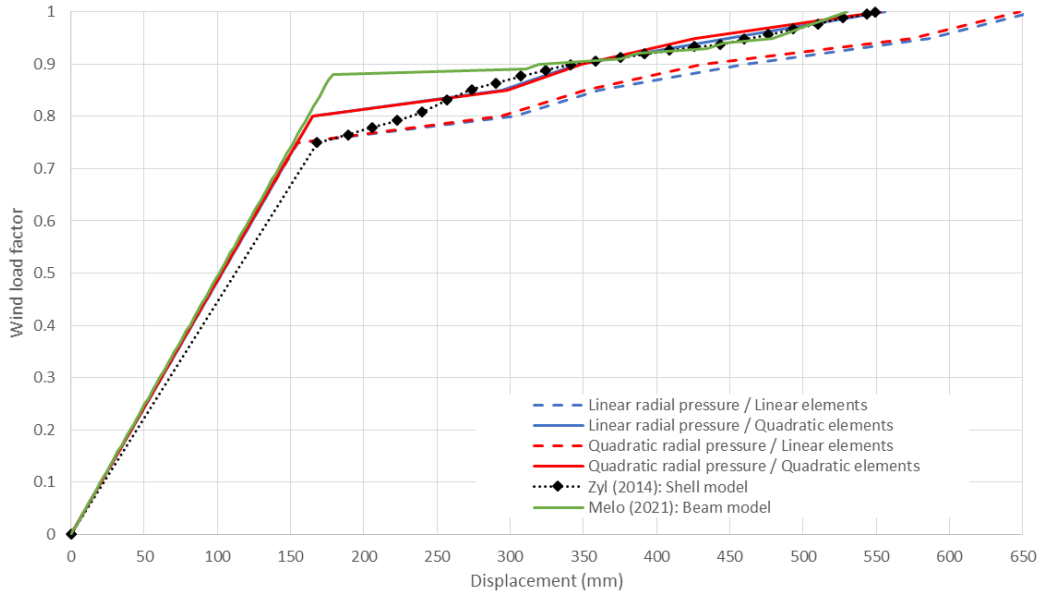

Source: elaborated by the author.

The results for the circumferential pressure distribution approximation models at ULS are presented in Table 18, whereas Figure 50 illustrates tower top deflection versus wind load for various configurations.

Table 18 – Results for circumferential pressure analysis (ULS)

Source	**Configuration**		**Uncracked frequency**		**After-loading frequency**		**Cracking initiation**	**Top deflection at 30%**		**Top deflection at 100%**	
			Value (Hz)	Diff.[a] (%)	Value (Hz)	Diff.[a] (%)	Value[b] (%)	Value (mm)	Diff.[a] (%)	Value (mm)	Diff.[a] (%)
Zyl (2014)	Shell model		0.445	-	0.228	-	30	155.0	-	1808.0	-
Melo (2021)	Beam model		0.450	1.12	0.214	-6.14	30	166.4	7.35	2125.3	17.55
The present study	Linear pressure	Linear elements	0.440	-1.12	0.206	-9.65	30	164.1	5.88	2228.8	23.27
		Quadratic elements	0.440	-1.12	0.205	-10.09	30	163.9	5.77	2232.1	23.46
	Quadratic pressure	Linear elements	0.440	-1.12	0.201	-11.84	30	162.6	4.89	2198.6	21.61
		Quadratic elements	0.440	-1.12	0.200	-12.28	30	162.4	4.77	2201.7	21.77

[a] Comparison to the results obtained from Zyl (2014); [b] Percentage of the total wind load.

Source: elaborated by the author.

Figure 50 – Deflection for circumferential pressure analysis (ULS)

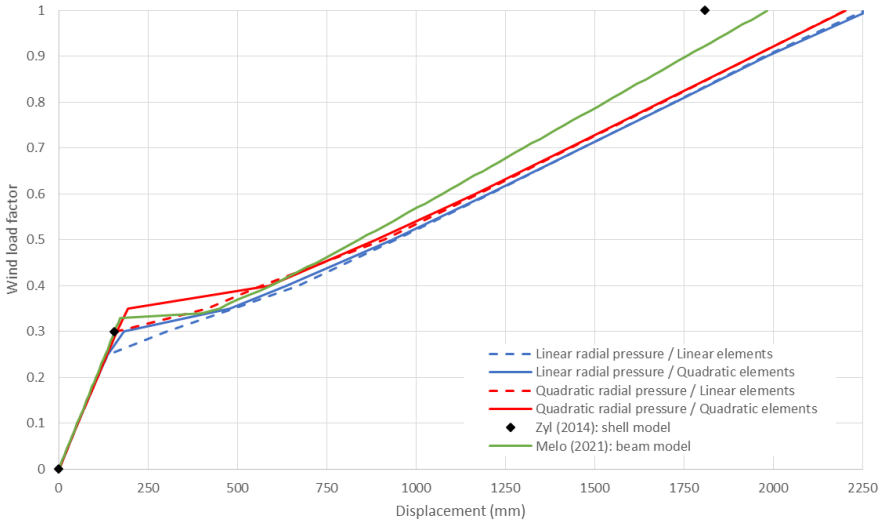

Source: elaborated by the author.

There is no significant difference between the linear and quadratic approximation for the radial pressure, probably because of the mesh fine refinement on the circumferential direction and the wind load applied on the turbine has a greater order of magnitude than the wind load applied on the tower. Therefore, the changes between the approximations for the wind load on the tower are too small to present any significant difference on the result for the global behavior of the structure.

The difference between the linear and quadratic elements results is due to the reduction of the concrete tensile strength on the linear elements, whose stress concentrations are not captured with precision within the element, increasing the material ductility. This occurred because the elements at the bottom half of the tower have larger dimensions than the maximum element size required for the linear elements. Linear elements also caused the tower to crack within a lower wind load magnitude.

The quadratic elements model with a quadratic approximation for the radial pressure presented a smaller difference in comparison to the results obtained in Zyl (2014), particularly at SLS. The ULS difference is larger, especially after cracking, because of the greater sensitivity to the software settings and various methodology aspects, such as how the turbine loads are applied and the reinforcing steel grid model, which leads to a much smaller reinforcement ratio than the bar model adopted by Zyl (2014).

The beam model on Melo (2021) presented a less than 3.5% difference to the deflection on the top at both SLS and ULS in comparison to the quadratic elements model with a quadratic approximation for the radial pressure analysis. The beam model detected cracking at 88% of the wind load for the SLS, which is 13% more than the shell model. One reason for

this may be the peak of concrete stress at the windward bottom of the tower which can be easily detected by shell elements, but not beam elements, since it is a more localized occurrence. That peak of concrete stress results in an earlier cracking initiation on these areas.

The cracking initiation occurs earlier for the ULS than for the SLS, which is expected because for the ULS the self-weight partial load factor is smaller than for the SLS in comparison to the wind loads (1.0 ratio for the SLS and 0.56 ratio for the ULS), more so, the wind pressure at ULS is much greater than at SLS.

An important aspect to mention is that cracking initiation occurs earlier than observed on the figures for some cases, in comparison to the values presented on the tables. The actual cracking initiation can be observed on a few elements at the windward base of the tower, which is not yet enough to produce a significant change in the tower's global behavior.

5.1.2 Torsion load model

The results of the SLS analysis for the torsion forces distribution based on the thin-walled tube average shear stress method and Zyl's method are presented in Table 19 and Figure 51.

Table 19 – Results for the torsion force distribution analysis (SLS)

Source	**Configuration**		**Uncracked frequency**		**After-loading frequency**		**Cracking initiation**	**Top deflection at 75%**		**Top deflection at 100%**	
			Value (Hz)	Diff.[a] (%)	Value (Hz)	Diff.[a] (%)	Value[b] (%)	Value (mm)	Diff.[a] (%)	Value (mm)	Diff.[a] (%)
Zyl (2014)	Shell model		0.445	-	0.241	-	75	168.0	-	549.0	-
Melo (2021)	Beam model		0.449	0.90	0.225	-6.64	88	152.5	-9.23	535.5	-2.46
The present study	Zyl's method	Linear elements	0.440	-1.12	0.215	-10.79	70	154.6	-7.98	655.7	19.44
		Quadratic elements	0.440	-1.12	0.241	0.00	75	154.2	-8.23	555.0	1.10
	Average shear stress method	Linear elements	0.440	-1.12	0.217	-9.96	70	154.6	-7.99	647.6	17.96
		Quadratic elements	0.440	-1.12	0.241	0.00	75	154.2	-8.23	553.0	0.72

[a] Comparison to the results obtained from Zyl (2014); [b] Percentage of the total wind load.

Source: elaborated by the author.

Figure 51 – Deflection for the torsion force distribution analysis (SLS)

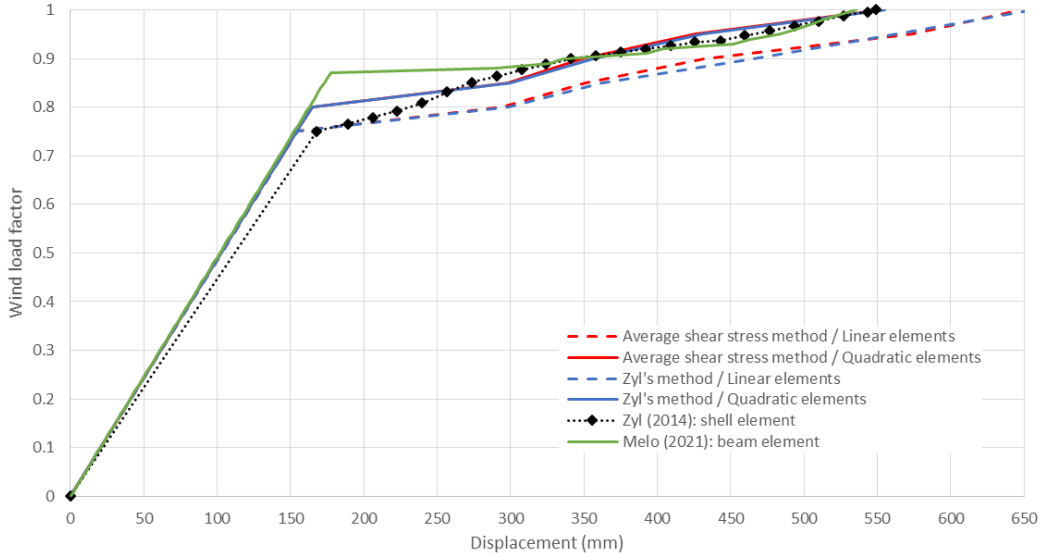

Source: elaborated by the author.

Both methods present similar results for SLS global behavior and can be used interchangeably for this type of analysis, although the thin-walled tube average shear stress method is more accurate and might avoid shear stress concentrations within the ring.

5.1.3 Thrust load model

The results for the thrust load location analysis at SLS are presented in Table 20, whereas Figure 52 illustrates tower top deflection versus wind load for various configurations.

Figure 52 – Deflection for the thrust force distribution analysis (SLS)

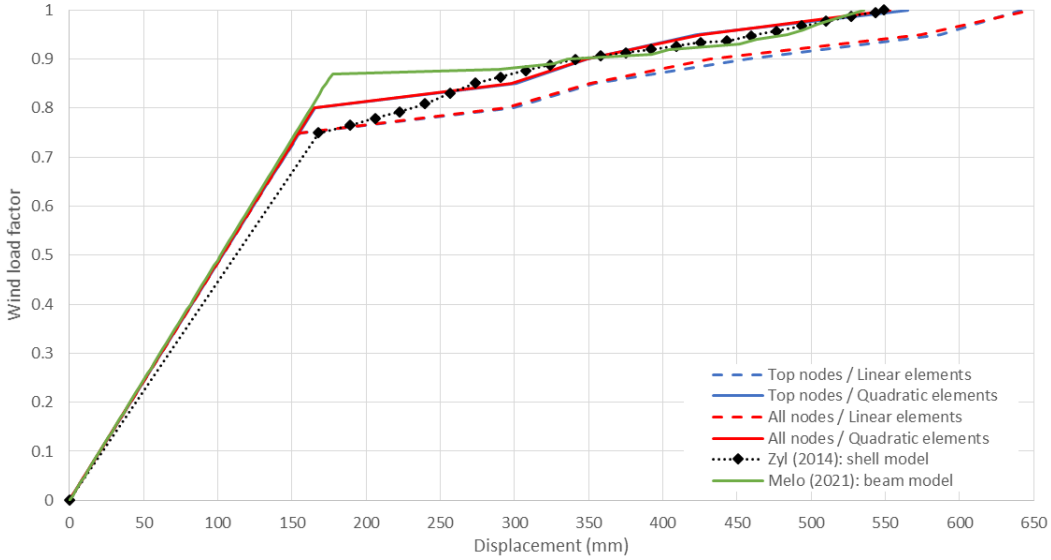

Source: elaborated by the author.

Table 20 – Results for the thrust force distribution analysis (SLS)

Source	Configuration		Uncracked frequency		After-loading frequency		Cracking initiation	Top deflection at 75%		Top deflection at 100%	
			Value (Hz)	Diff.[a] (%)	Value (Hz)	Diff.[a] (%)	Value[b] (%)	Value (mm)	Diff.[a] (%)	Value (mm)	Diff.[a] (%)
Zyl (2014)	Shell model		0.445	-	0.241	-	75	168.0	-	549.0	-
Melo (2021)	Beam model		0.449	0.90	0.225	-6.64	88	152.5	-9.23	535.5	-2.46
The present study	Applied on top nodes of the steel ring	Linear elements	0.440	-1.12	0.219	-9.13	70	155.2	-7.61	641.7	16.88
		Quadratic elements	0.440	-1.12	0.238	-1.24	75	154.8	-7.88	565.0	2.92
	Applied on all nodes of the steel ring	Linear elements	0.440	-1.12	0.217	-9.96	70	154.6	-7.99	647.6	17.96
		Quadratic elements	0.440	-1.12	0.241	0.00	75	154.2	-8.23	553.0	0.72

[a] Comparison to the results obtained from Zyl (2014); [b] Percentage of the total wind load.

Source: elaborated by the author.

Both methods presented similar results, with a maximum of 2.17% difference for deflection. These results are expected, as there is a small difference for the momentum generated at the base of the tower by distributing the thrust force on the vertical axis along the 0.5 m length of the ring, which is relatively small in comparison to the length of the tower.

The nacelle has the yaw mechanism, which is important for an upwind turbine, because it is used to keep the rotor facing into the wind as the wind direction changes. The yaw mechanism is located in the lowest part of the nacelle and on top of the tower, where the steel ring considered in this study is supposed to be located (Figure 53).

Although the results of both methods are similar, the presence of the yaw mechanism connection on the tower and the outer ring associated with it makes it more realistic to apply the thrust load as a distributed force at every node of the steel ring.

Figure 53 – Nacelle and tower connection

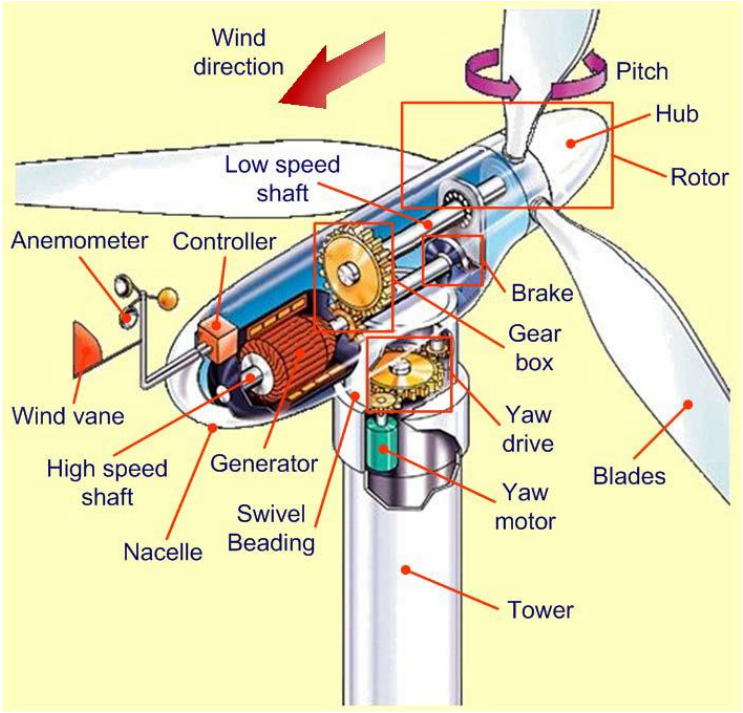

Source: Molina & Mercado (2011).

5.1.4 Ring material

For this analysis, two different materials have been chosen for the ring on top of the tower: steel and a rigid material with Young's modulus equal to 100 times the value of the steel. The ring is a strategy to ensure the undeformed shape of the top section and is used to receive and transfer the turbine loads to the tower. It is important to mention that, in practice, the connector between the tower and the turbine is usually made of steel, but the details are unknown. Thus, this analysis focus on the effect of the material stiffness for the ring.

The results for the ring material analysis at SLS are presented in Table 21, whereas Figure 54 illustrates tower top deflection versus wind load for various configurations.

Both ring materials present similar results for the global behavior of the structure, but the rigid material could lead to numerical errors in the analysis, specifically for the internal stresses in the nodes on the tower and ring interface, caused by the great difference in material stiffness in this section.

Table 21 – Results for the ring material analysis (SLS)

Source	Configuration		Uncracked frequency		After-loading frequency		Cracking initiation	Top deflection at 75%		Top deflection at 100%	
			Value (Hz)	Diff.[a] (%)	Value (Hz)	Diff.[a] (%)	Value[b] (%)	Value (mm)	Diff.[a] (%)	Value (mm)	Diff.[a] (%)
Zyl (2014)	Shell model		0.445	-	0.241	-	75	168.0	-	549.0	-
Melo (2021)	Beam model		0.449	0.90	0.225	-6.64	88	152.5	-9.23	535.5	-2.46
The present study	Rigid ring	Linear elements	0.440	-1.12	0.214	-11.20	70	154.6	-7.99	659.3	20.09
		Quadratic elements	0.440	-1.12	0.244	1.24	75	154.2	-8.23	541.6	-1.35
	Steel ring	Linear elements	0.440	-1.12	0.217	-9.96	70	154.6	-7.99	647.6	17.96
		Quadratic elements	0.440	-1.12	0.241	0.00	75	154.2	-8.23	553.0	0.72

[a] Comparison to the results obtained from Zyl (2014); [b] Percentage of the total wind load.

Source: elaborated by the author.

Figure 54 – Deflection for the ring material analysis (SLS)

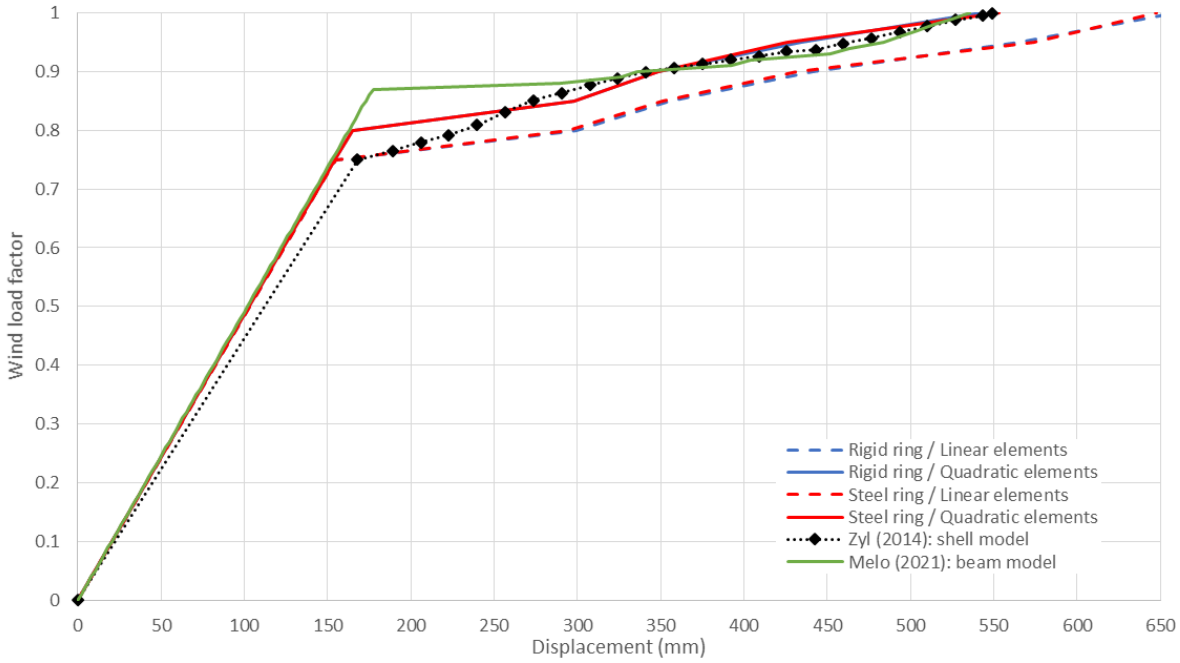

Source: elaborated by the author.

5.1.5 Turbine mass distribution

The results of the SLS and ULS analysis for the distributed turbine mass and the concentrated turbine mass are presented in Table 22, Table 23, Figure 55 and Figure 56.

Figure 55 – Deflection for the turbine mass analysis (SLS)

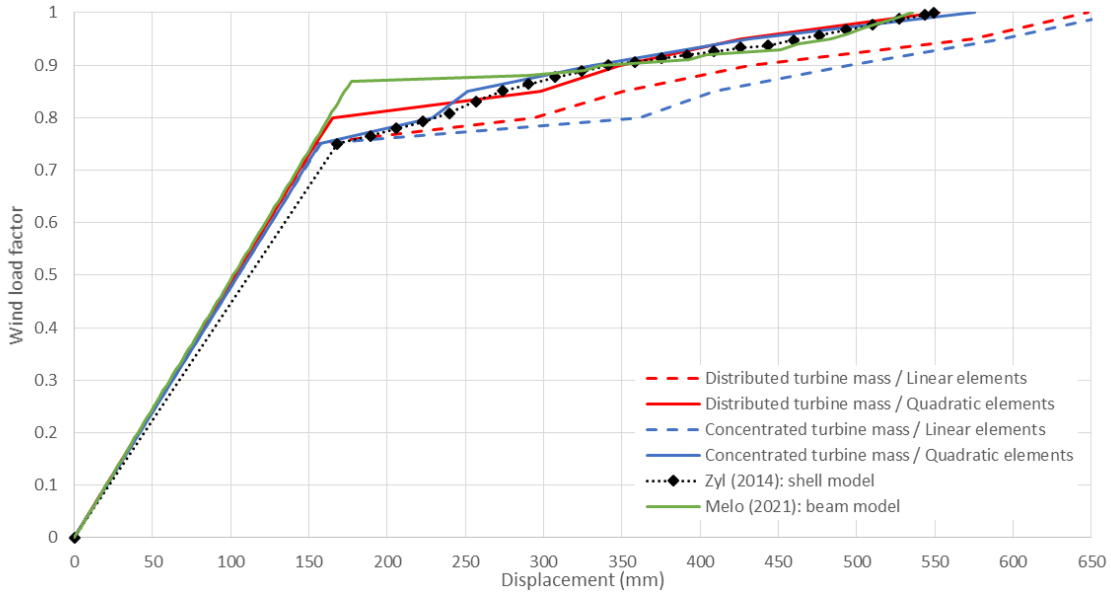

Source: elaborated by the author.

Figure 56 – Deflection for the turbine mass analysis (ULS)

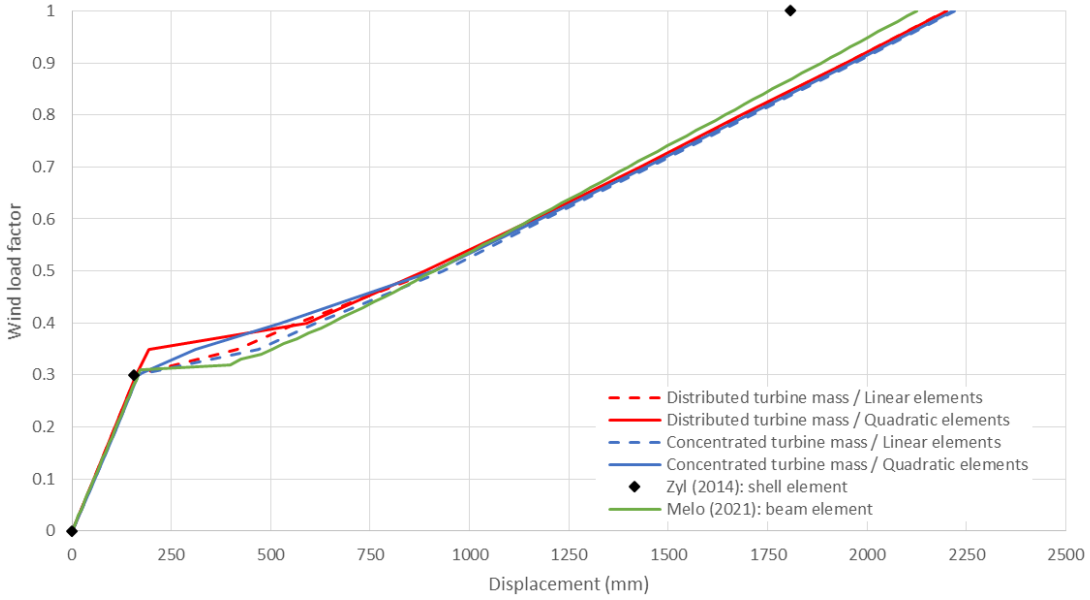

Source: elaborated by the author.

Table 22 – Results for the turbine mass analysis (SLS)

Source	Configuration		Uncracked frequency		After-loading frequency		Cracking initiation	Top deflection at 75%		Top deflection at 100%	
			Value (Hz)	Diff.[a] (%)	Value (Hz)	Diff.[a] (%)	Value[b] (%)	Value (mm)	Diff.[a] (%)	Value (mm)	Diff.[a] (%)
Zyl (2014)	Shell model		0.445	-	0.241	-	75	168.0	-	549.0	-
Melo (2021)	Beam model		0.449	0.90	0.225	-6.64	88	152.5	-9.23	535.5	-2.46
The present study	Concentrated turbine mass	Linear elements	0.444	-0.22	0.215	-10.79	70	157.3	-6.36	671.5	22.31
		Quadratic elements	0.444	-0.22	0.237	-1.66	70	156.7	-6.72	575.3	4.79
	Distributed turbine mass	Linear elements	0.440	-1.12	0.217	-9.96	70	154.6	-7.99	647.6	17.96
		Quadratic elements	0.440	-1.12	0.241	0.00	75	154.2	-8.23	553.0	0.72

[a] Comparison to the results obtained from Zyl (2014); [b] Percentage of the total wind load.

Source: elaborated by the author.

Table 23 – Results for the turbine mass analysis (ULS)

Source	Configuration		Uncracked frequency		After-loading frequency		Cracking initiation	Top deflection at 30%		Top deflection at 100%	
			Value (Hz)	Diff.[a] (%)	Value (Hz)	Diff.[a] (%)	Value[b] (%)	Value (mm)	Diff.[a] (%)	Value (mm)	Diff.[a] (%)
Zyl (2014)	Shell model		0.445	-	0.228	-	30	155.0	-	1808.0	-
Melo (2021)	Beam model		0.450	1.12	0.214	-6.14	30	166.4	7.35	2125.3	17.55
The present study	Concentrated turbine mass	Linear elements	0.444	-0.22	0.201	-11.84	30	166.4	7.34	2220.1	22.79
		Quadratic elements	0.444	-0.22	0.202	-11.40	30	166.2	7.22	2214.6	22.49
	Distributed turbine mass	Linear elements	0.440	-1.12	0.201	-11.84	30	162.6	4.89	2198.7	21.61
		Quadratic elements	0.440	-1.12	0.200	-12.28	30	162.4	4.77	2201.7	21.77

[a] Comparison to the results obtained from Zyl (2014); [b] Percentage of the total wind load.

Source: elaborated by the author.

The methods presented a maximum of 4.35% difference for deflection on SLS and 1.18% on ULS, with no apparent significant change to the global behavior of the structure. The distributed mass method divides the mass of the nacelle equally between the top nodes of the ring, on the other hand, the concentrated mass method applies the nacelle mass on a node along the tower axis. The translations of this node are then linked with distributed connections to the top edge of the ring.

5.1.5.1 Tower natural frequencies

A modal analysis of the uncracked tower clamped at the bottom is done. Due to the axisymmetric shape of the uncracked tower, some modes' shapes occur twice at the same frequency. Figure 57 illustrates the first ten modal shapes and eigenfrequencies of the tower obtained when analyzing the tower with a concentrated nacelle mass on top of it.

Figure 57 – Concentrated head mass tower frequencies

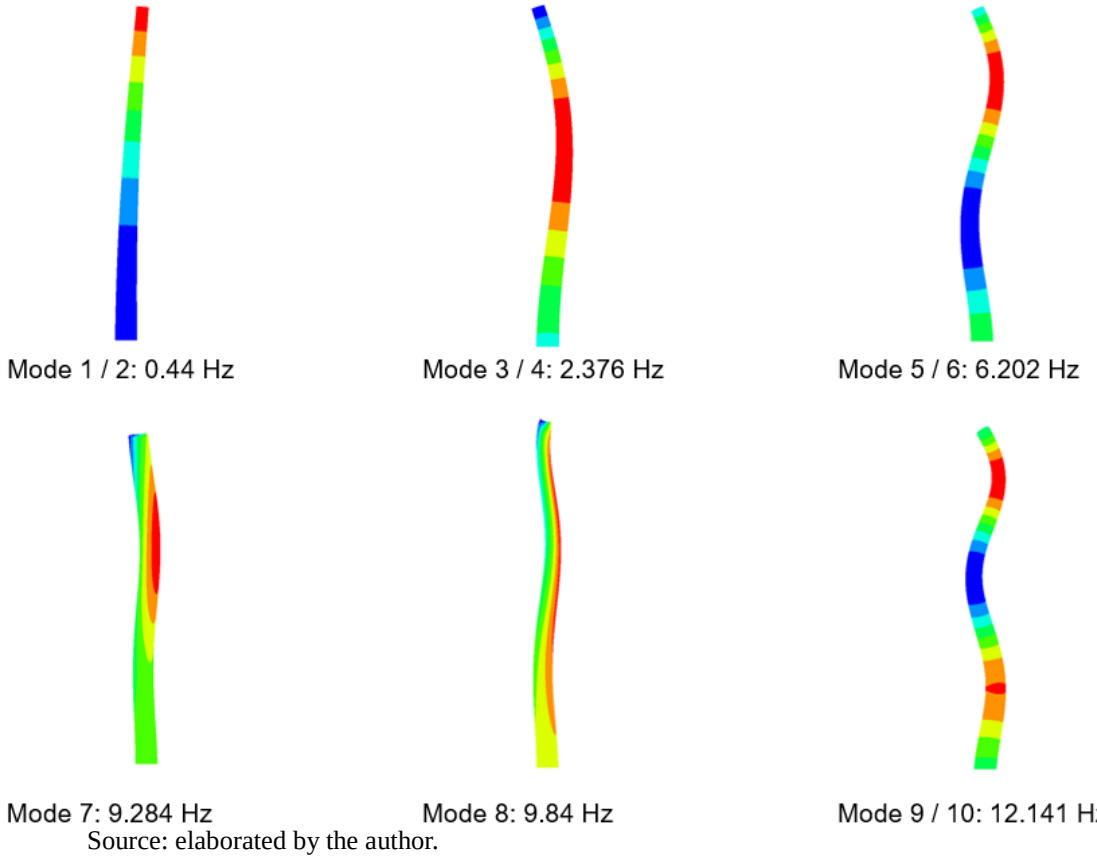

Source: elaborated by the author.

Figure 58 illustrates the first ten modes' shapes and eigenfrequencies of the tower obtained when analyzing the tower with a distributed nacelle mass on top of it.

Figure 58 – Distributed head mass tower frequencies

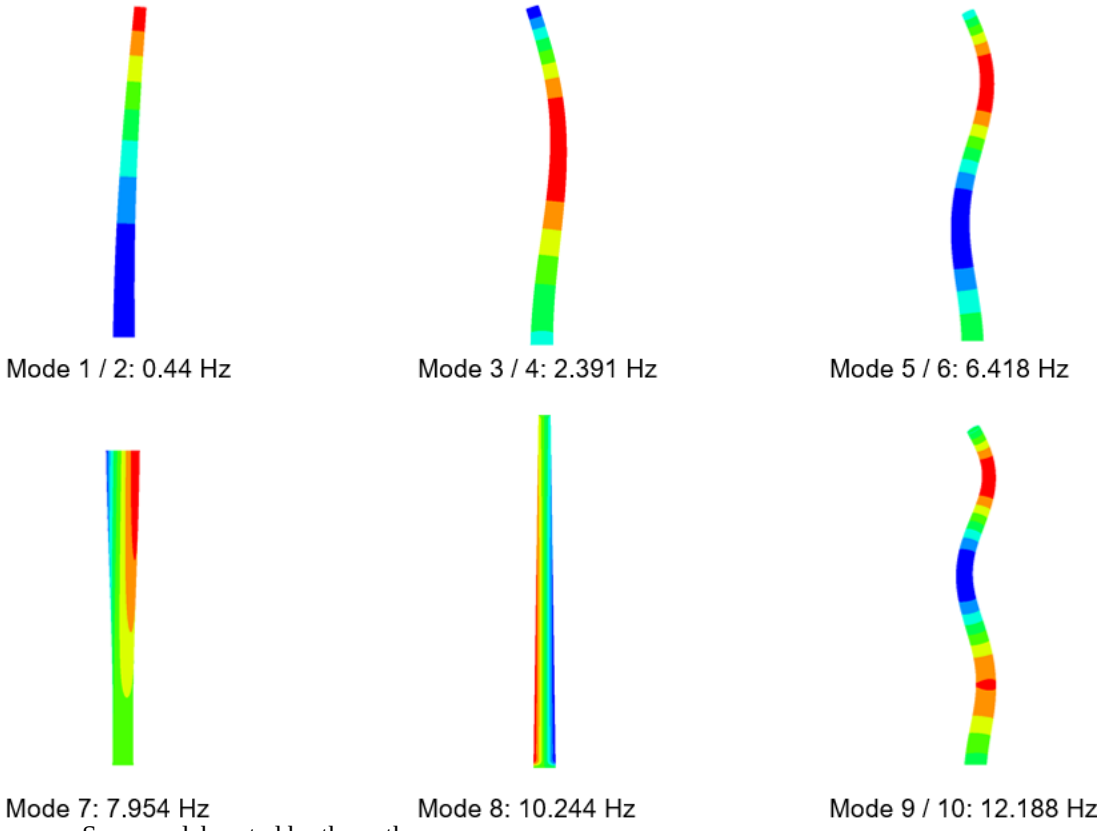

Source: elaborated by the author.

Most of the mode shapes and eigenfrequencies in both analyses are similar, with the exception of modes 7 and 8. That is explained by the connections on the top nodes of the ring that are necessary for the concentrated mass analysis, since these connections prevent the seventh and eighth modes that appear on the distributed mass analysis to be computed. Therefore, the concentrated mass method may lead to inaccurate results.

It is important to observe that the seventh mode and eigenfrequency on the distributed analysis cannot be computed in less refined models, such as beam models.

5.1.6 Concrete stress

An important aspect to investigate for the wind tower is the concrete stress. The results in this section are obtained when applying 100% of the wind load for every case. The maximum stress for the concrete in the vertical direction, as a function of the tower height during the SLS, is illustrated in Figure 59 for the leeward and windward.

Stress peaks are observed at the base of the tower, where the boundary conditions restraint the rotations in two axes and displacement in all three axes. The concrete will tend to

expand perpendicular to the principal compressive stress direction due to the Poisson effect, but the rigid boundary condition restricts this expansion, causing a large stress concentration (ZYL, 2014).

Figure 59 – Concrete vertical normal stress at SLS for the reinforced tower: a) Leeward, b) Windward

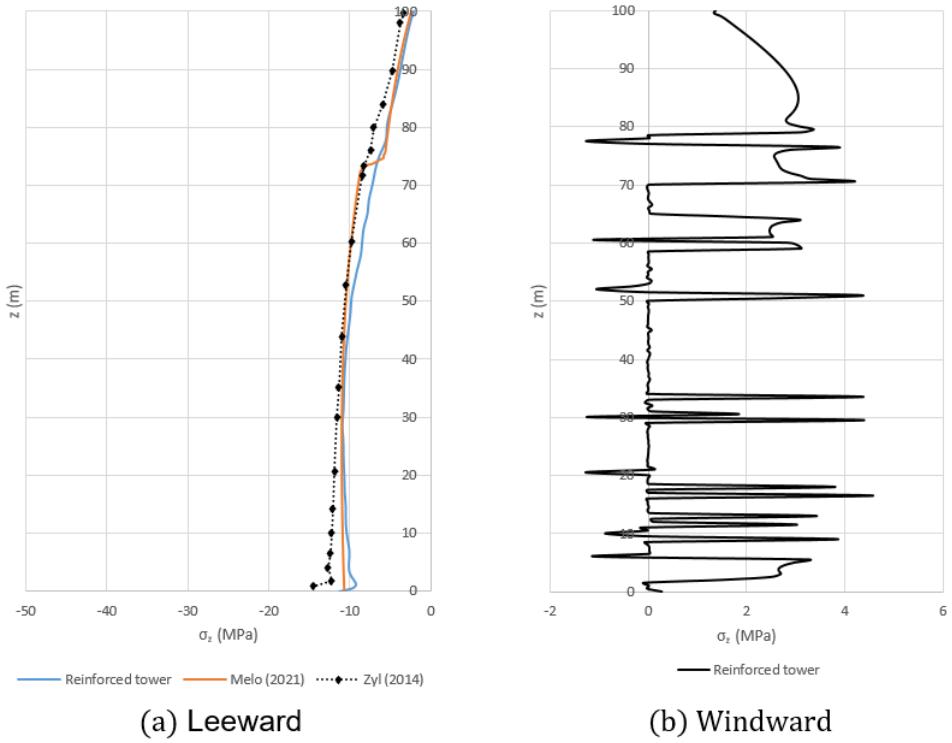

Source: elaborated by the author.

The figure shows that most of the concrete section at windward does not have the capacity to resist tensile stress after-loading (the sudden drops on stress caused by cracking) and that the tower is mostly failing due to the great tensile stress caused by the wind load. Although there are few sections along the tower height that are still able of resisting tensile stress, therefore did not reach the concrete tensile strength.

In this case, the maximum concrete stress is still well below the concrete compressive strength during the SLS, which indicates that a lower strength class of concrete or a thinner section might be used in this tower.

The maximum stress for the concrete in the vertical direction at leeward and windward, as a function of the tower height, is illustrated in Figure 60 for ULS. It is possible to observe that the whole concrete at windward reached concrete tensile strength, leading to cracking, which causes a great reduction of the structure stiffness and an increase of the tower deflection.

Figure 60 – Concrete vertical normal stress at ULS for the reinforced tower: a) Leeward, b) Windward

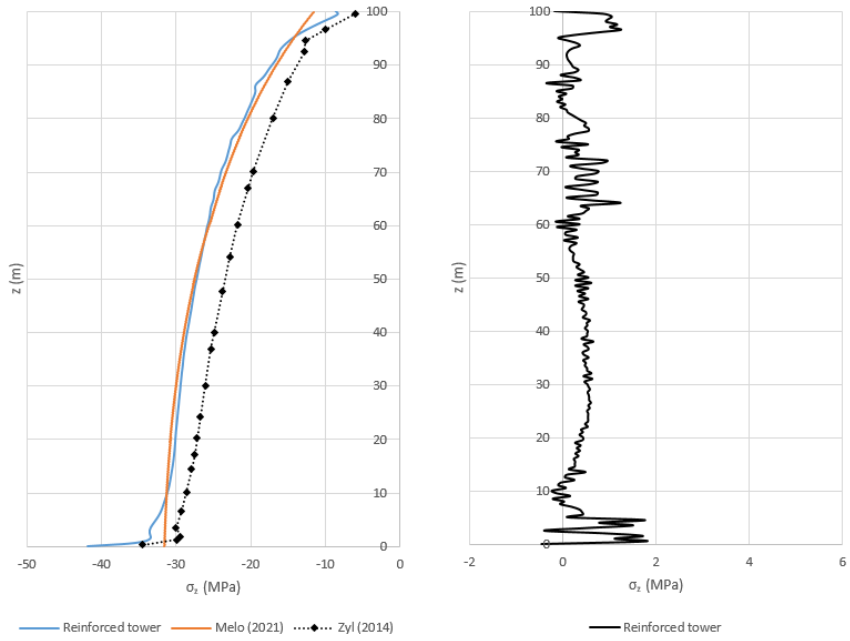

(a) Leeward (b) Windward

Source: elaborated by the author.

5.1.7 Crack pattern

For reinforced concrete towers, cracks initiate in both SLS and ULS and transfer tensile stress from the concrete to the reinforcing steel. Figure 61 and Figure 62 illustrate the crack pattern forming for SLS and ULS, respectively.

Figure 61 – Crack pattern at windward for the SLS on the reinforced tower

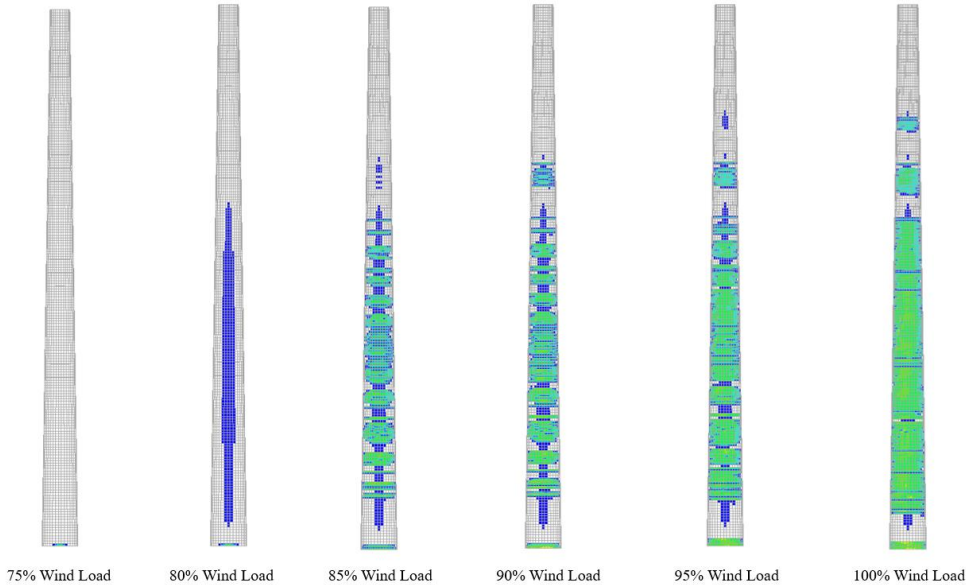

Source: elaborated by the author.

Figure 62 – Crack pattern at windward for the ULS on the reinforced tower

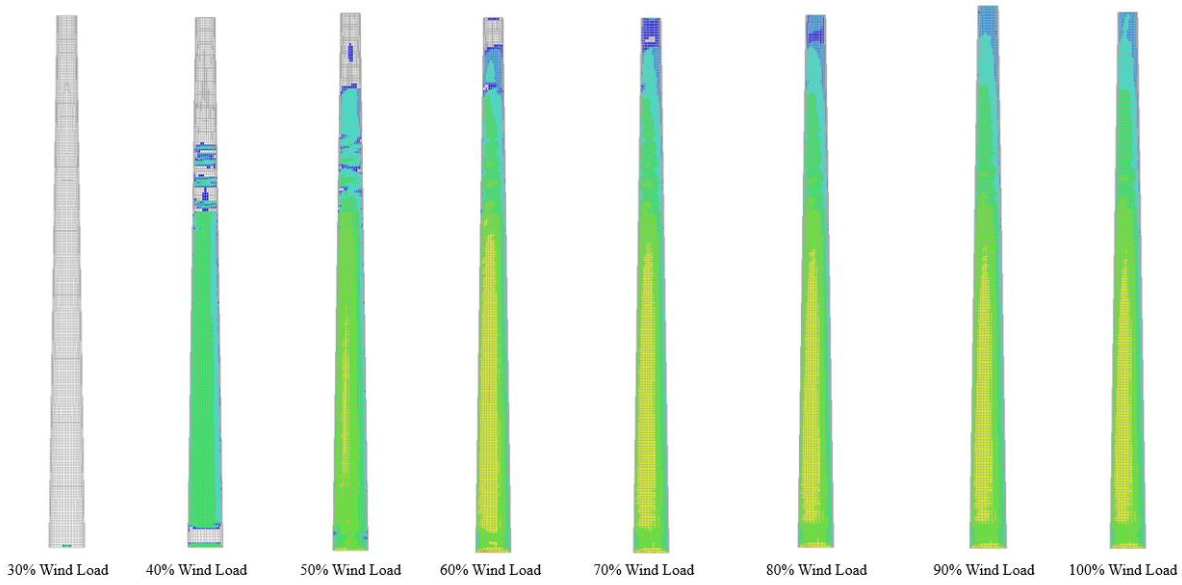

Source: elaborated by the author.

Crack initiation occurs at approximately 75% of the total wind load for SLS and 30% for ULS. The maximum crack width obtained for SLS and ULS is shown in Table 24, in addition to the recommended maximum crack width at SLS specified by the ACI 224 (2007), as there is no specific guideline for wind towers.

Table 24 – Maximum and computed crack widths for the reinforced tower analysis

FEM		
Limit State	**Wind load (%)**	**Crack Width (mm)**
Serviceability	75	0.024
	80	0.083
	85	0.588
	90	0.614
	95	0.680
	100	0.685
Ultimate	100	1.930
ACI 224 (2007)		
Exposure condition		**Crack Width (mm)**
Dry air		0.41
Humidity, moist air, soil		0.30
Deicing chemical		0.18
Seawater and seawater spray, wetting and drying		0.15
Water-retaining structures		0.10

Source: elaborated by the author.

The crack width is limited in the SLS to avoid loss of stiffness which reduces the fundamental frequency of the tower. The maximum wind load where the crack width is within the limits recommended by the ACI 224 (2007) is 80%, therefore, it is recommended to reduce the crack width. One can increase the reinforcing steel section or decrease the spacing of the bars for this purpose, which may reduce the tensile stress in reinforcing.

A cost-effective method of reducing the crack width of the concrete without increasing the percentage of reinforcing steel is inserting prestressing, while also decreasing the reinforcing steel.

5.1.8 Soil-structure interaction

An important aspect to take into consideration during the wind tower analysis is the soil type that the tower is built upon, the foundation itself and its effects on the structure global behavior. The soil-structure interaction can have significant effects on the structure behavior, such as the fundamental frequency, which in turn changes the wind pressure on the tower.

The results for the soil-structure interaction analysis for various soil types at SLS are presented in Table 25, whereas Figure 63 illustrates the tower deflection for various soil types and using the equivalent vertical translational springs model presented on Section 3.7.

Table 25 – Results for the soil-structure interaction analysis on reinforced tower (SLS)

Soil type and foundation configuration		**Uncracked frequency**		**After-loading frequency**		**Cracking initiation**	**Top deflection at 75%**		**Top deflection at 100%**	
		Value (Hz)	Diff.[a] (%)	Value (Hz)	Diff.[a] (%)	Value[b] (%)	Value (mm)	Diff.[a] (%)	Value (mm)	Diff.[a] (%)
No foundation / Fixed base		0.440	-	0.241	-	75	154.2	-	553.0	-
With foundation	Fixed	0.421	-4.32	0.236	-2.07	80	165.2	7.17	569.9	3.06
	Fine sand	0.355	-19.32	0.218	-9.54	75	215.7	39.89	653.8	18.23
	Sand	0.375	-14.77	0.225	-6.64	80	198.0	28.42	620.3	12.18
	Coarse sand	0.381	-13.41	0.225	-6.64	80	193.1	25.25	622.6	12.59
	Gravel	0.393	-10.68	0.232	-3.73	80	183.8	19.21	591.1	6.90
	Soft clay	0.270	-38.64	0.188	-21.99	75	340.1	120.61	848.4	53.43
	Clay	0.320	-27.27	0.208	-13.69	75	255.3	65.58	713.7	29.06
	Stiff clay	0.361	-17.95	0.219	-9.13	75	210.0	36.21	647.3	17.06

[a] Comparison to the no foundation / fixed base analysis; [b] Percentage of the total wind load.

Source: elaborated by the author.

Figure 63 – Deflection for the soil-structure interaction analysis on reinforced tower (SLS)

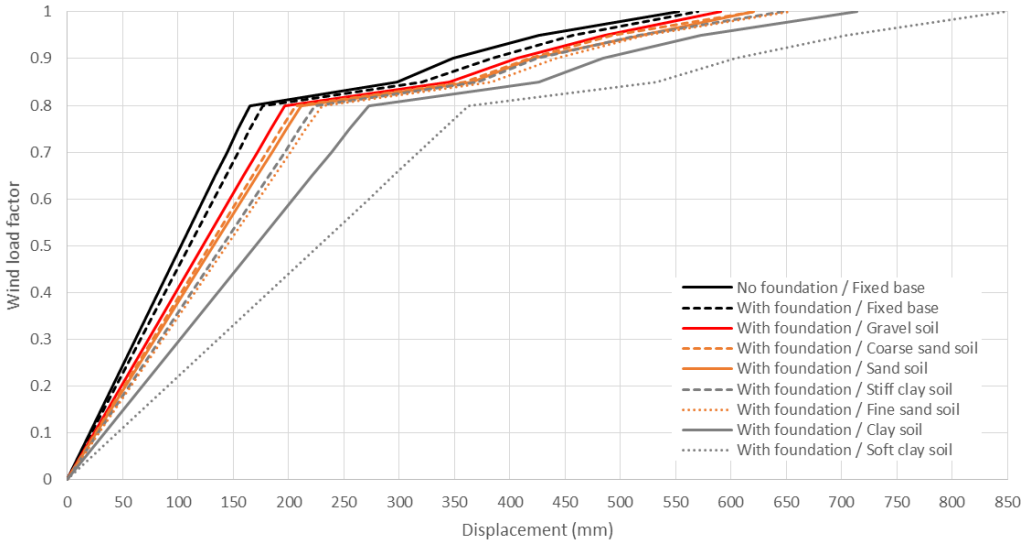

Source: elaborated by the author.

The foundation itself is responsible for a 2.07% reduction in fundamental frequency for the SLS. There is an increase in the wind load percentage for crack initiation in some cases, since the stress concentration on the tower base is relieved by the tower-foundation interface, where the crack initiation occurs.

The percentage reduction on fundamental frequencies is significant for some types of soils, such as soft clay, with a 21.99% reduction on SLS, which emphasize the importance of detailed geotechnical studies to determine the soil stiffness and extensive soil preparation before the structure is constructed.

Table 26 presents a comparison between the fundamental frequencies obtained during this research and the ones obtained by Zyl (2014).

Table 26 – Fundamental frequencies for the reinforced tower soil-structure interaction

Limit State	**Soil type**	**Frequency (Hz)**		**Difference**
		Present study	**Zyl (2014)**	**(%)**
Serviceability (Uncracked)	Fine sand	0.355	0.343	3.50
	Sand	0.375	0.361	3.88
	Coarse sand	0.381	0.367	3.81
	Gravel	0.393	0.378	3.97
	Soft clay	0.270	0.273	-1.10
	Clay	0.320	0.320	0.00
Ultimate (Cracked)	Sand	0.191	0.161	18.63

Source: elaborated by the author.

The fundamental frequencies for the SLS present similar results to the ones obtained by Zyl (2014), with a difference of less than 3.97%. The difference is higher for the ULS (18.63%), which is expected, as observed in the previous analysis comparison to Zyl's results.

5.2 Prestressed tower

This section presents the results obtained from the prestressed tower FEM analysis. All the results are obtained according to the methods discussed in Chapters 2 and 3 and the example chosen was presented in Chapter 4. The comparison between the results obtained in this research and the ones obtained in previous works is important to determine the accuracy of the method and to validate less refined models. The prestressed tower model is used to verify and compare several methodological aspects, while also being used in a parametric study.

The standard prestressed tower in analysis has the following configuration, except when stated otherwise: no vertical reinforcing steel, 36 full-length parallel to the wall prestressing tendons, deviator-guided, 100% prestress load, geometric and material nonlinearity, fixed base with no foundation included in the model.

The reinforced concrete tower used in this section is the same as the standard one presented in the previous section, which is useful to verify and compare the changes in the global behavior of the tower caused by the insertion of prestressing forces, even if there is an absence of vertical reinforcing steel on the prestressed tower.

Table 27 summarizes the finite element configuration used for this analysis, the design parameters subjected to the parametric study and the different methods configurations that are studied in this section.

An important aspect to take into consideration is the processing time required for the analysis. Using a computer with the following hardware specifications: Intel(R) Core(TM) i5-9400F CPU @ 2.90GHz, 64 bits operating system and 16.00 GB RAM, for the SLS standard prestressed tower analysis, it took 123 and 153 seconds for the linear and nonlinear material cases, respectively, whereas, for the ULS, it took 144 and 187 seconds for the linear and nonlinear material cases, respectively. The free-vibration analysis is taken into consideration for the processing time.

The modified Newton-Raphson iterative method has also been applied for the prestressed tower and presented almost identical results to the regular method, with a reduction of 3.94% and 2.14% in the total processing time for SLS and ULS, respectively.

Table 27 – Finite element, methods and parameters configurations for the prestressed tower

Description	**Configurations**		
Iterative method	Standard Newton-Raphson		
Geometrical nonlinearity formulation	Total Lagrangian		
Convergence norm	Displacement and force		
Solution method	Parallel direct sparse		
Element type	Quadratic		
Circumferential pressure distribution	Quadratic		
Torsion load	Average shear stress		
Thrust load	All nodes		
Ring material	Steel		
Turbine mass	Distributed		
	Configurations investigated		
Vertical reinforcing steel	0% to 100% (Based on the value present in Table 12)		
Prestress load	30% to 160% (Based on the value present in Table 13)		
Tendons placement	Vertical and parallel to the tower wall. Distributed in various radius.		
Nonlinearity	Geometric	Material	-
Deviators	No deviators	Deviator-guided	-
Number of prestressing tendons	9	18	36
Tendon distribution over the tower height	24 whole-length and 12 half-length	30 whole-length and 6 half-length	-
Half-length cables anchorage	Steel disc	Tower wall	-

Source: elaborated by the author.

One must verify the FEM accuracy by comparing the applied forces to the FEM reaction forces. The difference for both SLS and ULS are presented in Table 28 and it is possible to observe that it is relatively small, thus, the forces are correctly applied in the FEM.

Table 28 – Difference for prestressed tower FEM equilibrium

Forces	**SLS (%)**	**ULS (%)**
Axial force	-0.16	-0.16
Overturning moment	1.50	1.05
Thrust force	0.35	0.24
Torsional moment	1.58	1.76

Source: elaborated by the author.

Both energy variation and relative out-of-balance force criteria mentioned in the previous section are met for all load steps.

5.2.1 Deviators and amount of prestressing tendons

In this section, one presents the results for the tower with tendons without deviators and deviator-guided, while also investigating the effect of changing the number of tendons, while maintaining the same total prestressed steel area.

The results for tower top deflection and fundamental frequency for SLS are presented in Table 29 and Figure 64 illustrates the tower top deflection versus wind load for various tendons configurations.

Table 29 – Results for the deviators and amount of prestressing tendons analysis (SLS)

Tower configuration			Uncracked frequency		After-loading frequency		Cracking initiation	Top deflection at 75%		Top deflection at 100%	
			Value (Hz)	Diff.[a] (%)	Value (Hz)	Diff.[a] (%)	Value[b] (%)	Value (mm)	Diff.[a] (%)	Value (mm)	Diff.[a] (%)
Reinforced Tower			0.440	-	0.241	-	75	154.2	-	553.0	-
Prestressed Tower	Without deviators	9, 18 and 36 tendons	0.380	-13.64	0.378	56.85	-	181.5	17.75	242.0	-56.23
	Deviator-guided	9, 18 and 36 tendons	0.418	-5.00	0.416	72.61	-	165.4	7.29	220.5	-60.12

[a] Comparison to the reinforced tower; [b] Percentage of the total wind load.

Source: elaborated by the author.

Figure 64 – Deflection for the deviators and amount of prestressing tendons analysis (SLS)

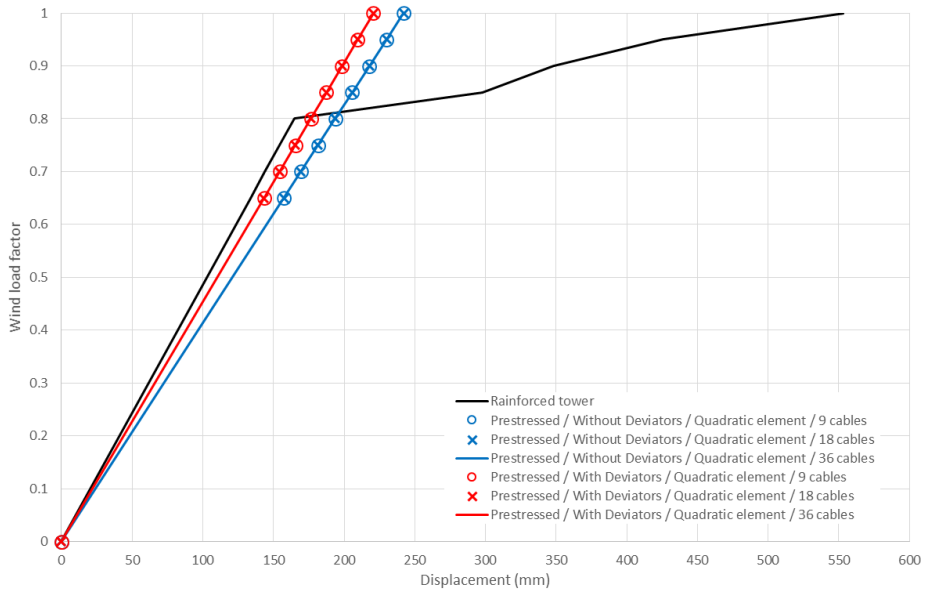

Source: elaborated by the author.

The maximum lateral deflection (in mm) according to the ACI-307 (2008) is $3.33h$, where h is the chimney height (m). The lateral deflection limit for this tower during the SLS is 333 mm, thus, the standard prestressed tower in analysis is within the limit allowed by the code.

Comparing the deviator-guided configuration to the case without deviators, there has been a 10% increase in the uncracked and after-loading frequencies and an 8.88% decrease for the top deflection at 75% and 100% of the wind load. Considering the cracked concrete, the increase on the fundamental frequency is higher than 50% with prestressing in comparison to the reinforced concrete case.

Figure 65 illustrates the problem that might appear if one analyzes the tendons without deviators (using amplification factors), where the unrestrained tendons go through the tower wall because the model does not compute where the tendons come into contact with the tower, while in reality, the tendons would be touching the inner wall, such as the example described by Grünberg & Göhlmann (2013) in Figure 15. That may invalidate all results obtained on the prestressed tower without deviators and shows the importance of implementing deviator-guided tendons.

Figure 65 – The lack of deviators problem

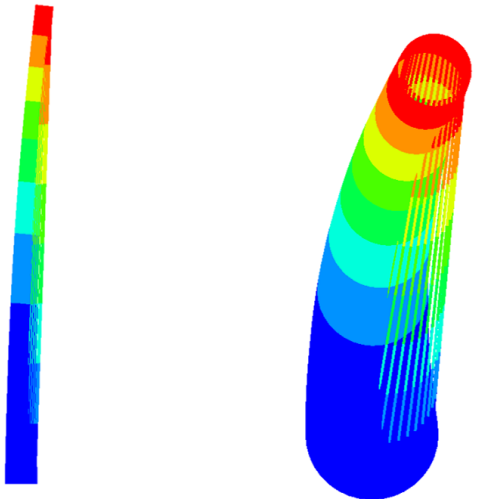

Source: elaborated by the author.

The results show that the presence of deviators increases the tower stiffness, because of the restoring component on the deviators. The number of tendons makes little to no difference on the tower global behavior, if the same total prestressed steel area is maintained, but using fewer cables generate stress concentration at anchorage points. The deviators are applied by connecting the tendons nodes' transversal displacements to the nearest nodes at the tower, therefore the number of tendons is limited by the number of elements on the

circumferential direction. This analysis is important to validate the model, since LaNier (2005) adopted 56 tendons originally for a similar tower.

Even though a divisor of the number of circumferential sections on the tower mesh can be used to determine the number of tendons in the model, it is recommended to use as many tendons as possible to properly distribute the prestress load across the tower section.

It is important to observe that, although the prestressed tower presents a great increase in the after-loading frequency and a decrease in the final deflection in comparison to the reinforced tower, due to the wind load for cracking initiation being higher, the uncracked frequency is lower and the deflection at 75% for SLS. This effect is further studied in section 5.2.3.

5.2.1.1 Tower natural frequencies

It is important to investigate the prestressed tower fundamental frequency to verify the changes that the prestress might cause on the tower's behavior. Figure 66 illustrates the first ten modes' shapes and eigenfrequencies of the prestressed tower obtained when using deviator-guided tendons.

Figure 66 – Tower frequencies for the deviator-guided prestressed tower

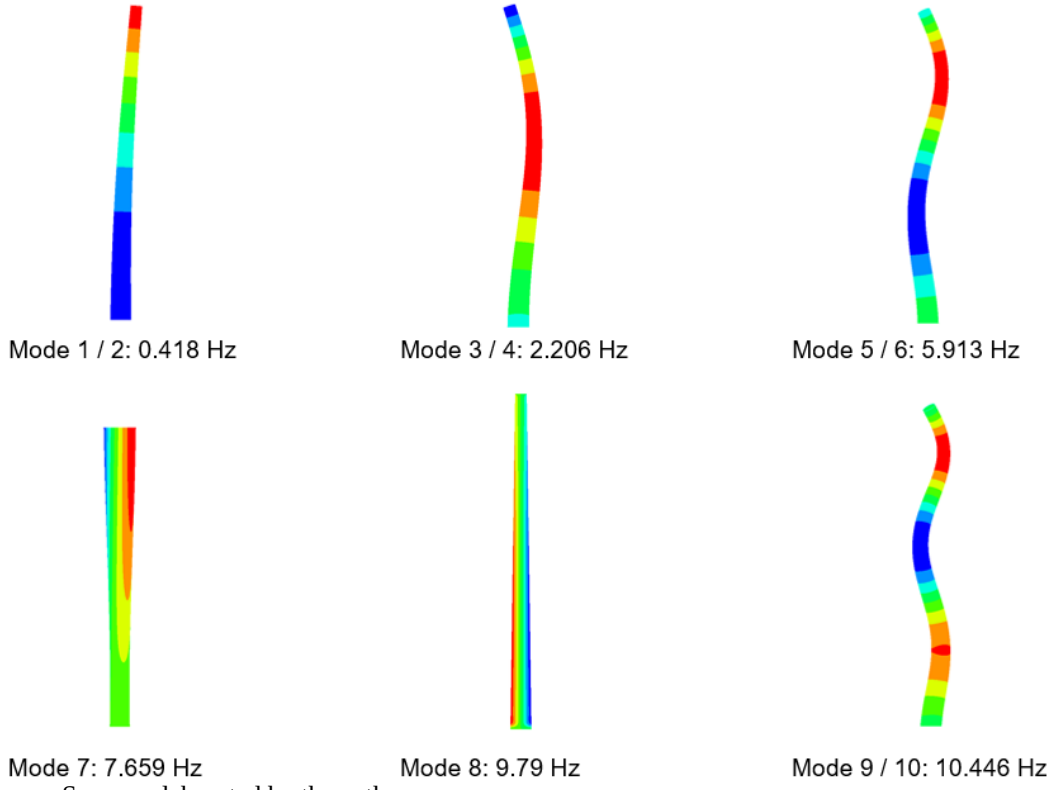

Source: elaborated by the author.

Some modes' shapes that are the same but occur around different axes are grouped. The modes' shapes are similar to the ones obtained for the reinforced tower with the distributed mass in section 5.1.5.1, but the eigenfrequencies for the prestressed tower are overall lower than the reinforced.

5.2.2 Vertical reinforcing steel

In this section, one analyzes the effects of the vertical reinforcing steel for the prestressed tower. Although the standard prestressed tower in this study does not consider vertical reinforcing steel (similar to Kenna & Basu (2015), Lana *et al*. (2021) and Tomczack (2021)) , ACI-307 (2008) recommends a minimum reinforcing steel for chimney design, which also serves for practical purposes during the construction stages of the tower.

Figure 67 shows the tower top deflection versus wind load for various vertical reinforcing steel ratios at SLS. The tower uncracked and after-loading fundamental frequencies for the vertical reinforcing steel analysis at SLS are illustrated in Figure 68-a, whereas Figure 68-b shows the deflection on the top at 75% and 100% wind load.

Figure 67 – Deflection for the vertical reinforcing analysis (SLS)

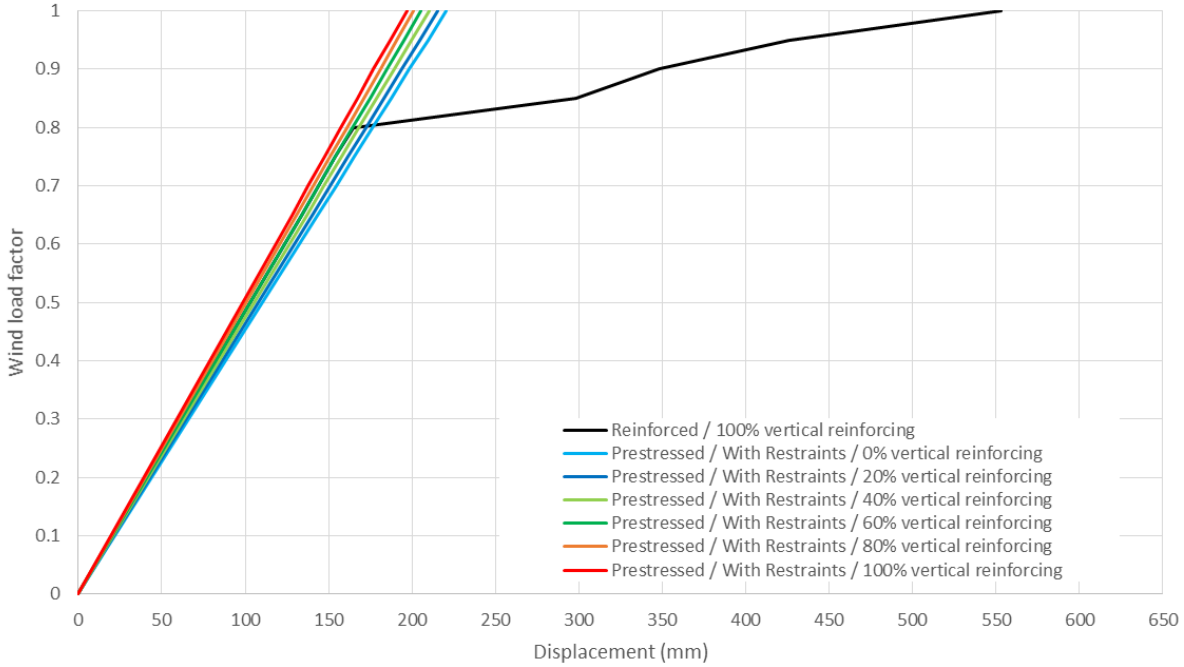

Source: elaborated by the author.

Figure 68 – Tower's behavior versus vertical reinforcing at SLS (100% vertical reinforcing = 5068 mm²/m): a) fundamental frequency, b) top displacement

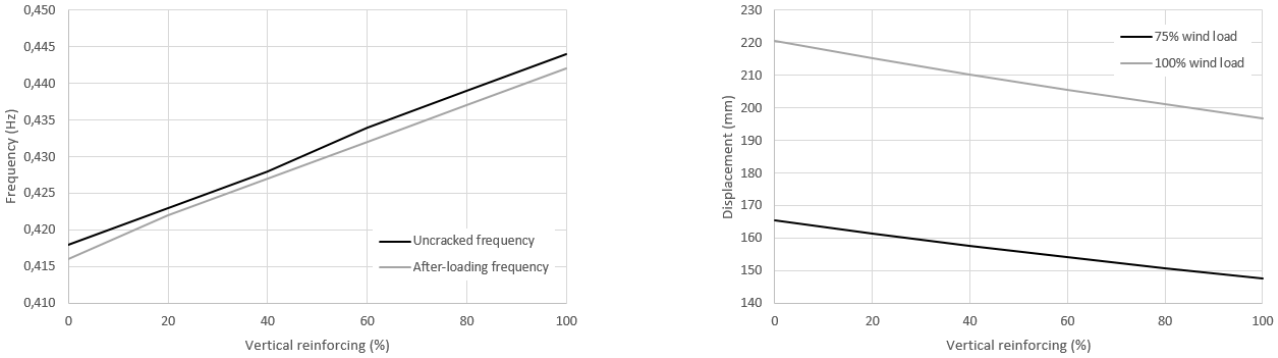

(a) (b)

Source: elaborated by the author.

When one compares the reinforced tower and the prestressed tower, both with 100% vertical reinforcing, it is possible to observe that the prestress load increased the wind load for cracking initiation, but offered only a little increase on the tower stiffness at the linear portion of the curve at SLS. On the other hand, the prestress offered a great increase in the stiffness after 75% and of the wind load.

The vertical reinforcing steel did not change the cracking initiation wind load, as the tower did not crack at SLS and cracked at 90% wind load for ULS. It did increase the tower fundamental frequency and, therefore, also increased the tower stiffness. In comparison to the 0% case, the 100% vertical reinforcing steel case: increased 6.22% of the uncracked frequency and decreased 10.77% deflection on the top at SLS.

5.2.3 Prestress load

This section shows the effects of the prestress load level on the tower, by analyzing the same tower subjected to various values for prestress load. The comparisons made in this section are based on the reinforced tower with 100% vertical reinforcing to verify and analyze the differences between feasible solutions. The prestress load is based on the value present in Table 13. The results for tower top deflection and fundamental frequency for SLS are presented in Table 30, whereas Figure 69 illustrates a portion of the wind load-tower top deflection curve for various prestress levels.

Table 30 – Results for the prestress load analysis (SLS)

Tower configuration	Prestress load[a]	Uncracked frequency		After-loading frequency		Cracking initiation	Top deflection at 75%		Top deflection at 100%	
		Value (Hz)	Diff.[b] (%)	Value (Hz)	Diff.[b] (%)	Value[c] (%)	Value (mm)	Diff.[b] (%)	Value (mm)	Diff.[b] (%)
Reinforced tower		0.440	-	0.241	-	75	154.2	-	553.0	-
Prestressed tower	30%	0.419	-4.77	0.418	73.44	-	164.8	6.89	219.7	-60.27
	60%	0.419	-4.77	0.417	73.03	-	165.1	7.09	220.1	-60.20
	100%	0.418	-5.00	0.416	72.61	-	165.4	7.28	220.5	-60.12
	130%	0.416	-5.45	0.415	72.20	-	165.9	7.61	221.2	-60.00
	160%	0.406	-7.73	0.405	68.05	-	168.3	9.16	225.2	-59.28

[a] Based on the value present in Table 13; [b] Comparison to the reinforced tower; [c] Percentage of the total wind load.

Source: elaborated by the author.

Figure 69 – Detail of top deflection for the prestress load analysis (SLS)

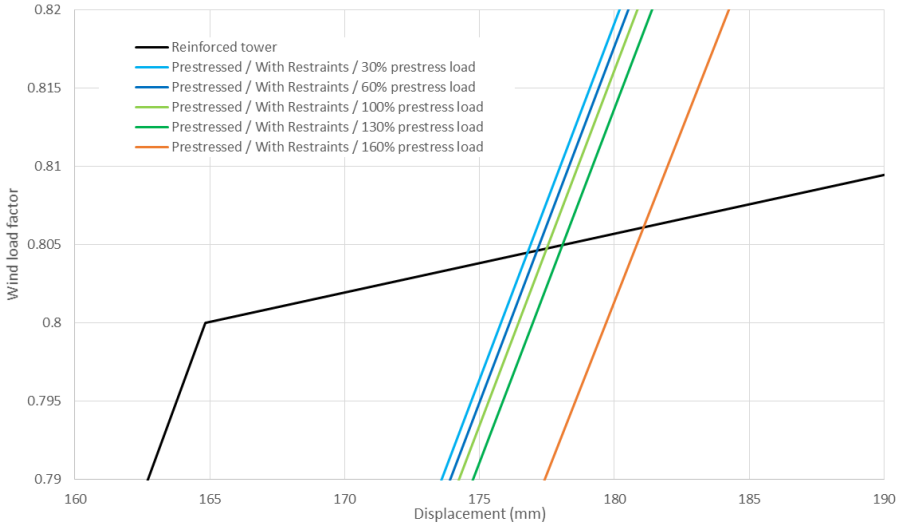

Source: elaborated by the author.

For the SLS prestressed tower analysis, the tower remains uncracked during the wind load actions even with the lowest prestress load applied. The reinforced tower cracked at 75% of the wind load, greatly reducing the tower stiffness after 75% wind load in comparison to the prestressed tower, whose deflection curves remain linear. Comparing the 30% prestress load case to the reinforced tower, there was a 73.44% increase in the after-loading frequency and a 60.27% decrease in deflection at 100% wind load.

The results for tower top deflection and fundamental frequency for ULS are presented in Table 31, whereas Figure 70 illustrates the tower top deflection versus wind load for various prestress loads.

Table 31 – Results for the prestress load analysis (ULS)

Tower configuration	Prestress load[a]	Uncracked frequency		After-loading frequency		Cracking initiation	Top deflection at 30%		Top deflection at 100%	
		Value (Hz)	Diff.[b] (%)	Value (Hz)	Diff.[b] (%)	Value[c] (%)	Value (mm)	Diff.[b] (%)	Value (mm)	Diff.[b] (%)
Reinforced tower		0.440	-	0.200	-	30	162.4	-	2201.7	-
Prestressed tower	30%	0.419	-4.77	0.088	-56.10	45	200.0	23.15	7886.1	258.18
	60%	0.419	-4.77	0.109	-45.50	70	202.8	24.85	1578.6	-28.30
	100%	0.418	-5.00	0.411	105.50	90	203.2	25.11	678.3	-69.19
	130%	0.416	-5.45	0.413	106.50	-	203.8	25.49	679.4	-69.14
	160%	0.406	-7.73	0.405	102.50	-	206.1	26.94	696.3	-68.37

[a] Based on the value present in Table 13; [b] Comparison to the reinforced tower; [c] Percentage of the total wind load.

Source: elaborated by the author.

Figure 70 – Deflection for the prestress load analysis (ULS)

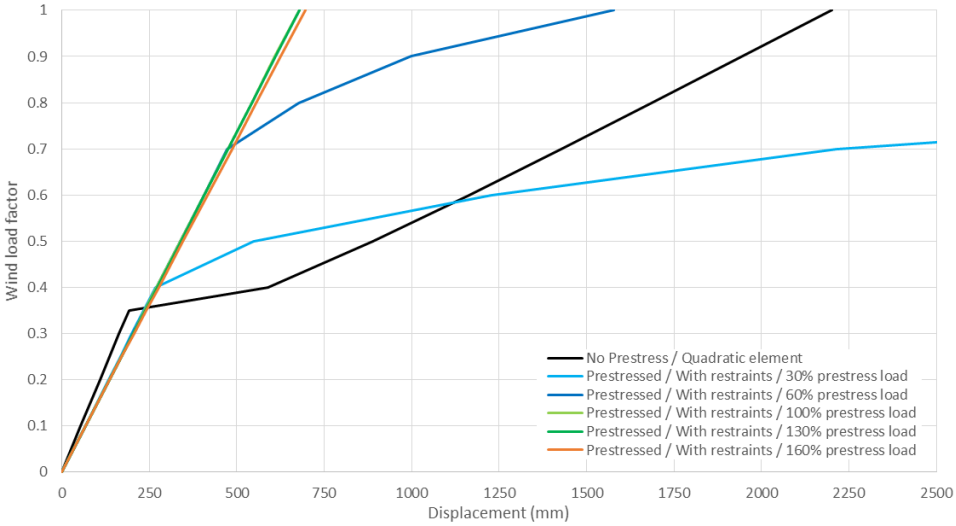

Source: elaborated by the author.

From the ULS prestressed tower analysis, it is possible to observe the prestress load improvements on the tower, as it increases the wind load level for cracking initiation. The 60% prestress load case is already enough to justify the prestress application on the tower, it increased the cracking initiation to 70% of the wind load, in comparison to the 30% for the reinforced tower, even though the effects of the wind load after the cracking initiation is great, as observed by the large deflection at 100% wind load and frequency decrease after loading.

The great increase in the top deflection of the 30% prestress case in comparison to the reinforced tower is caused by the absence of vertical reinforcement. When one analyzes the same prestressed tower case using the vertical reinforcement present on the reinforced concrete

tower, the top deflection is reduced to 1398.8 mm (36.46% decrease in comparison to the reinforced tower). It is important to mention that the ULS for the 30% prestress case did not meet all convergence criteria and it is kept here for research purposes only.

For the 100% prestress load case, cracking initiation occurs at 90% of the wind load, therefore the after-cracking effects are small enough to maintain the deflection curve at a relatively linear behavior. It greatly increased the after-loading frequency and decreased deflection at 100% wind load in comparison to the reinforced tower. Further increases of prestress load above 100% lead to no cracking occurring during ULS analysis, which is not necessary for the design of the tower.

Increases in the prestress load lead to lower tower stiffness (decrease in the tower frequency and increases in the deflection), which is further investigated in section 5.2.4.

5.2.3.1 Concrete stress

It is important to investigate the concrete stress to verify what happens to the tower when the prestress load is applied. This section is used to analyze the concrete stress along the height of the tower for the prestress tower subjected to 30%, 60% and 100% of the prestress load and compare to the reinforced tower. The results in this section are obtained when applying 100% of the wind load for every case.

Figure 71 and Figure 72 illustrate the concrete vertical normal stress for SLS and ULS, respectively. The presence of deviators on the tendons, which are connected to the tower wall, causes little peaks at the curve every 25 m. The peak on the top of the tower is where the prestressing tendons are anchored.

At SLS, it is possible to observe that the compressive stress is still far from the concrete compressive strength for all the cases and, as expected, an increase in the prestress load leads to an increase in the compressive stress. Cracking occurs only for the reinforced tower, but the 30% prestress load case presents tensile stress at windward, which is not ideal for the prestressed tower, as there can be no tensile stress for the serviceability limit state on prestressed structures.

Figure 71 – Concrete vertical normal stress at SLS for the prestress load analysis: a) Leeward, b) Windward

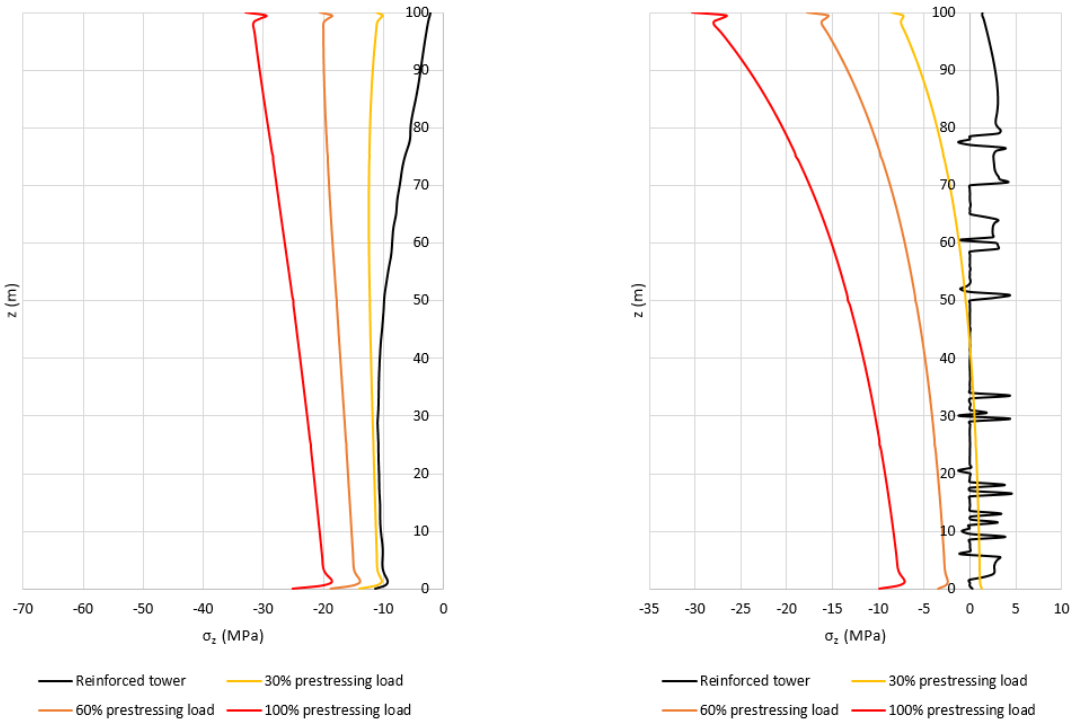

(a) Leeward (b) Windward

Source: elaborated by the author.

Figure 72 – Concrete vertical normal stress at ULS for the prestress load analysis: a) Leeward, b) Windward

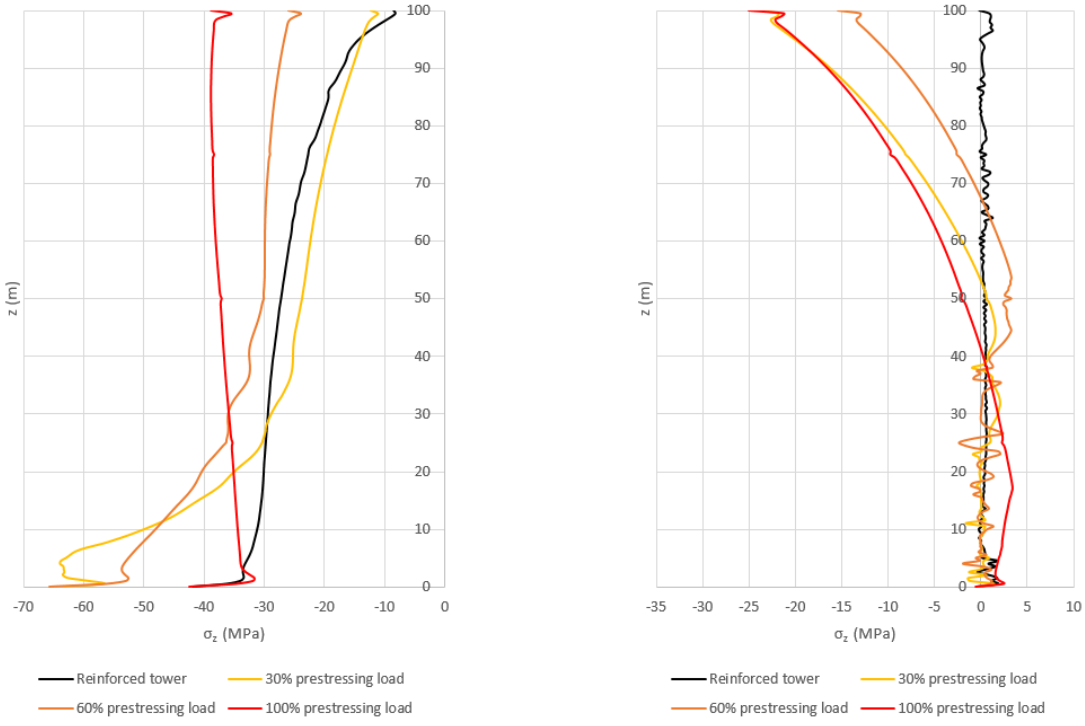

(a) Leeward (b) Windward

Source: elaborated by the author.

For the ULS analysis, cracking occurs at the windward, leading to greater deflection of the tower, increasing the compressive stress at leeward, which is further increased by the prestress load. On the 30% and 60% prestress load cases, the increase on compressive stress was enough to surpass the concrete compressive strength at the bottom half of the tower.

Cracking initiation is observed for all cases on the ULS analysis, as the tensile stress surpassed the concrete tensile strength. The 30% and 60% prestress load cases were not enough to mitigate the after-cracking effects on the tower, which lead to great tensile stress at the bottom half of the tower.

Another important aspect to observe on the concrete stress is how the compressive stress increase with the tower height, this is because the tower section reduces with the height and the prestress force remains the same. This effect is further investigated in section 5.2.6.

5.2.3.2 Crack pattern

Cracking did not occur for the prestressed tower during SLS, thus, the cracking pattern for the ULS is shown in this section for research and comparison purpose, as cracking pattern and width during ULS is not important for the analysis.

Figure 73 illustrates the crack pattern formed at ULS for the reinforced tower, 30%, 60% and 100% prestress load cases, which further highlight the importance of prestressing and choosing the appropriate prestress load for the tower.

Figure 73 – Crack pattern at windward for the ULS on the prestressed tower analysis (100% wind load)

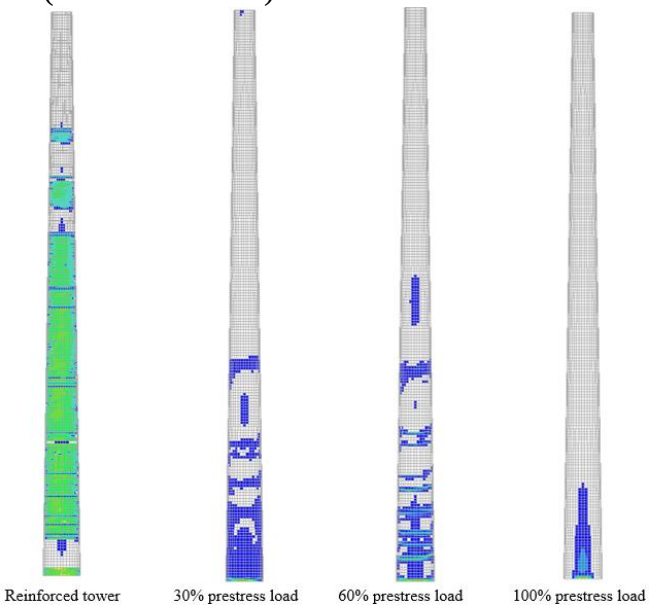

Source: elaborated by the author.

Table 32 shows how the crack width is greatly reduced when choosing the correct prestress load.

Table 32 – Maximum crack widths for the prestressed tower analysis

Limit State	Prestress load (%)	Crack Width (mm)
Ultimate (100% wind load)	Reinforced	1.930
	30	133.000
	60	26.600
	100	0.256

Source: elaborated by the author.

For all prestressed tower cases, cracking only occurred at the bottom half of the tower, whereas it appear along almost all tower length for the reinforced case.

5.2.4 Nonlinearity effects

It has been observed from previous analysis that an increase in the prestress load leads to lower tower fundamental frequency, which is actually lower than the ones obtained on the reinforced tower. Higher prestress load levels are adopted in this section for research purposes only, as 100% of the prestress load has already been proven appropriate for this tower.

When one analyzes the tower using a geometric and material linear model (Table 33), the increase in prestress loads actually increases the fundamental frequency, by generating greater restoring forces and compressive stress on the concrete.

Table 33 – Effects of the nonlinearity in the fundamental frequency

Fundamental Frequency Comparison (Hz)				
Configuration	Material	Linear	Linear	Nonlinear
	Geometric	Linear	Nonlinear	Nonlinear
Reinforced tower		0.442	0.442	0.440
Prestress Loads	30%	0.447	0.419	0.419
	60%	0.469	0.419	0.419
	100%	0.487	0.418	0.418
	300%	0.566	0.413	0.405
	400%	0.726	0.410	0.405

Source: elaborated by the author.

For the lower levels prestress loads applied on the tower (≤ 100%), stress levels in the material are lower than the concrete or steel strength, therefore, there's little influence of the material nonlinearity.

For higher levels of prestress load analyzed, the geometric nonlinearity is still the primary cause for the frequency reduction, but the nonlinear concrete and steel behavior also begins to influence the tower stiffness.

5.2.5 Tendons placement

This section investigates the placement of the prestressing tendons. The tendons in the other sections have been placed parallel to the tower wall, here it will also consider the tendons placed in the vertical direction. Tendons are placed at a distance *d*: 15, 30, 45, 60 and 120 cm from the inside of the wall (on top of the tower, for the vertical tendons), according to Figure 74.

Figure 74 – Tendons placement

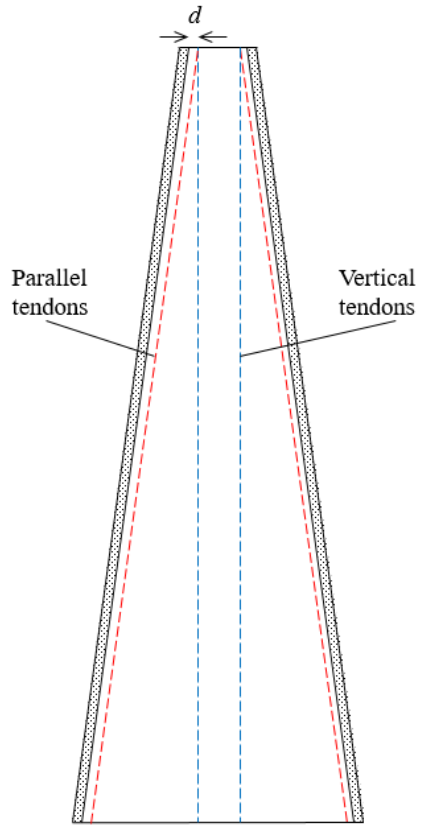

Source: elaborated by the author.

The results from Melo (2021) are presented in Table 34 for the SLS analysis, where the tower has been modeled as a beam element, with vertical tendons 15 cm from inside the wall on top of the tower, to validate and verify the feasibility of using beam models to analyze the prestressed tower. Results from similar tower configurations (15 cm from the inside of the wall) also presented in Table 34 and the results for tower top deflection and fundamental frequency for various configurations at SLS are in Figure 75.

Table 34 – Results for the prestressing tendons placement analysis (SLS)

Source	**Configuration**	**Uncracked frequency**		**After-loading frequency**		**Cracking initiation**	**Top deflection at 75%**		**Top deflection at 100%**	
		Value (Hz)	Diff.[a] (%)	Value (Hz)	Diff.[a] (%)	Value[b] (%)	Value (mm)	Diff.[a] (%)	Value (mm)	Diff.[a] (%)
The present study	Parallel prestressing tendons	0.418	-	0.416	-	-	165.4	-	220.5	-
	Vertical prestressing tendons	0.412	-1.44	0.411	-1.20	-	170.3	2.96	227.1	2.96
Melo (2021)	Beam model	0.408	-2.39	0.408	-1.92	-	186.0	12.45	248.0	12.46

[a] Comparison to the parallel prestressing case; [b] Percentage of the total wind load.

Source: elaborated by the author.

Figure 75 – Tower's behavior versus tendons placement (distance to the tower wall) at SLS: a) fundamental frequency, b) top displacement

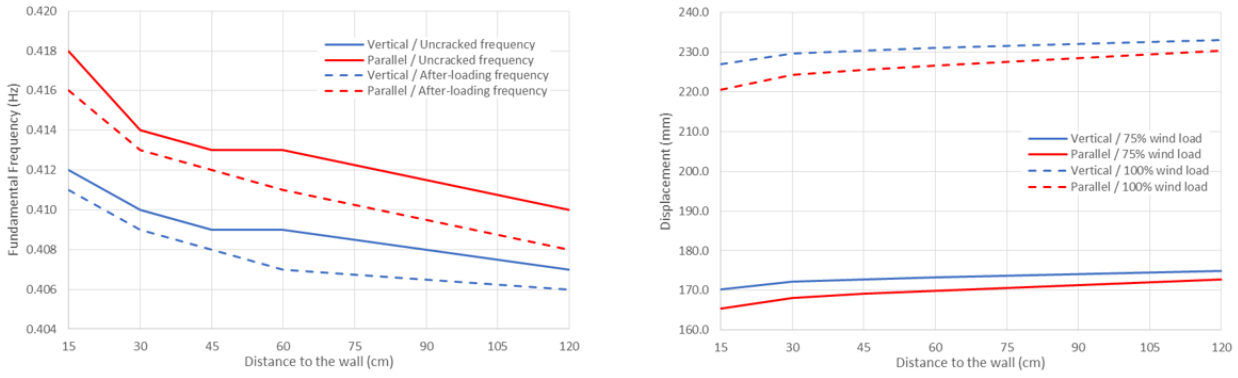

(a) (b)

Source: elaborated by the author.

Results from Melo (2021) and similar tower configurations are presented in Table 35 for the ULS analysis. All tendons placement cases using the present study model showed a cracking initiation at 90% of the wind load during the ULS analysis. The results for tower top

deflection and fundamental frequency for various configurations at ULS are presented in Figure 76.

Table 35 – Results for the prestressing tendons placement analysis (ULS)

Source	Configuration	Uncracked frequency		After-loading frequency		Cracking initiation	Top deflection at 30%		Top deflection at 100%	
		Value (Hz)	Diff.[a] (%)	Value (Hz)	Diff.[a] (%)	Value[b] (%)	Value (mm)	Diff.[a] (%)	Value (mm)	Diff.[a] (%)
The present study	Parallel prestressing tendons	0.418	-	0.411	-	90	203.2	-	678.3	-
	Vertical prestressing tendons	0.412	-1.44	0.348	-15.33	90	209.3	3.00	723.2	6.63
Melo (2021)	Beam model	0.407	-2.63	0.405	-1.46	-	205.5	1.15	685.0	0.99

[a] Comparison to the parallel prestressing case; [b] Percentage of the total wind load.

Source: elaborated by the author.

Figure 76 – Tower's behavior versus tendons placement (distance to the tower wall) at ULS: a) fundamental frequency, b) top displacement at 30% wind load, c) top displacement at 100% wind load

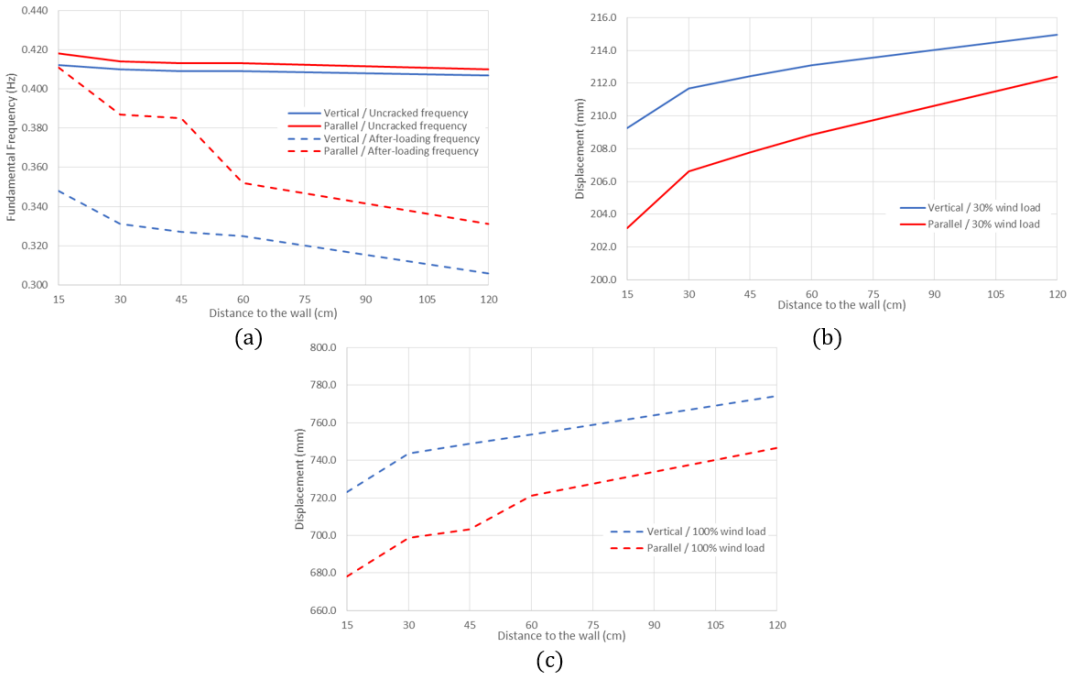

Source: elaborated by the author.

From the results, it can be observed that the distance from the tower wall did not influence significantly the global behavior of the tower. The rotation on top of the tower by the end of the analysis is little enough so that the different distances of the tendons from the

longitudinal axis of the tower did not cause significant strain differences on the tendons between the analyzed cases. In practice, it is recommended to install the tendons near the tower wall, as it offers a greater stiffness for the tower and to avoid long deviators components that might generate greater bending stresses at the anchorage support elements, which is not cost-efficient for the tower design.

Parallel tendons offered a greater stiffness for the tower than the vertical tendons: higher uncracked and cracked frequencies and less displacement overall. There was a great decrease in the fundamental frequency after-loading for the vertical tendons at ULS. Thus, it is recommended to use tendons parallel to the tower wall.

The beam model presented on Melo (2021) offered a good approximation of the tower global behavior, with a difference of 0.97% on the fundamental frequency, 9.23% for the displacement on the top at SLS and 5.29% at ULS in comparison to the vertical tendons case. The beam model did not crack at ULS, which is expected, as the cracking initiation at 90% for the shell model is caused by stress concentrations of the boundary conditions at the base of the tower. A multi-fidelity model can be used to circumvent this problem.

5.2.5.1 Concrete and tendon stress

To further investigate the difference between the tendons placement configuration and to compare the results to the one obtained by using the method adopted in Melo (2021), concrete and tendon stresses are also presented in this section.

Figure 77 and 78 illustrate the concrete vertical normal stress at 100% wind load on the concrete of the standard prestressed tower for the SLS and ULS analyses, respectively, using the 3D model to show the stress distribution around the tower.

Figure 79 illustrates the concrete vertical normal stress along with the tower height, specifically at windward and leeward, at SLS and the difference between Melo's model and the vertical tendons case. The shell model curves present peaks at the bottom, caused by the boundary conditions, and the top of the tower, generated by the applied loads (particularly the prestress load) and the steel ring.

Figure 80 illustrates the concrete vertical normal stress along with the tower height, specifically at windward and leeward, at ULS. It is possible to observe that the tensile stress surpassed the concrete tensile strength at the bottom of the tower for the vertical tendon configuration (Figure 80–b), which caused cracking to occur and increased the compressive stress at leeward (Figure 80–a).

Figure 77 – Concrete vertical normal stress at SLS for the standard prestressed tower: a) Leeward, b) Side view, c) Windward

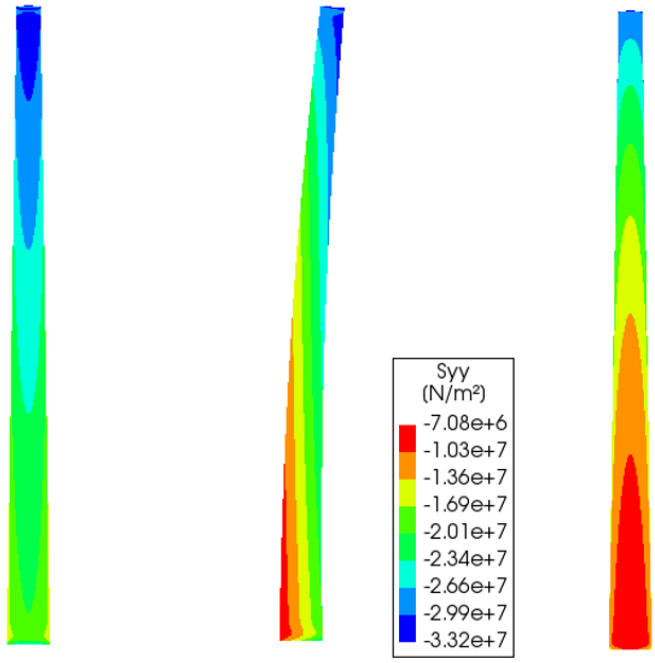

(a) Leeward (b) Side view (c) Windward

Source: elaborated by the author.

Figure 78 – Concrete vertical normal stress at ULS for the standard prestressed tower: a) Leeward, b) Side view, c) Windward

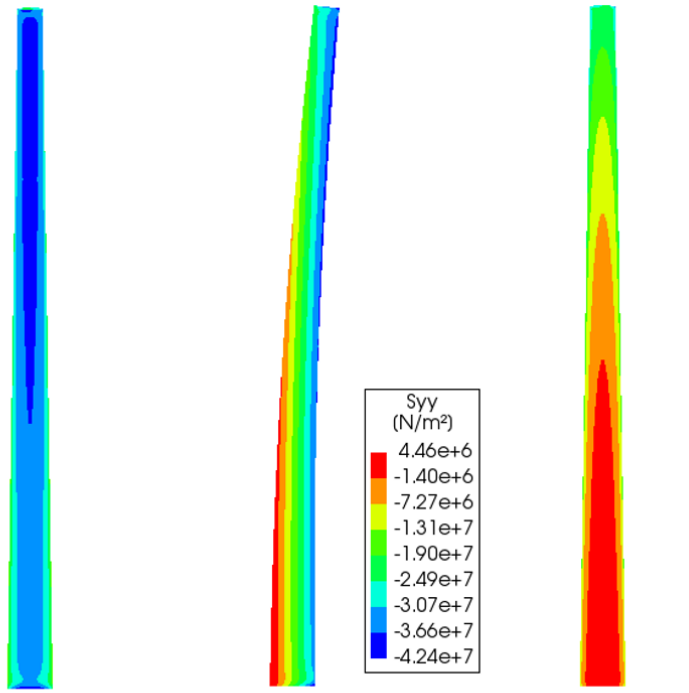

(a) Leeward (b) Side view (c) Windward

Source: elaborated by the author.

Figure 79 – Concrete vertical normal stress at SLS for the prestressing tendons placement analysis: a) Leeward, b) Windward, c) Difference

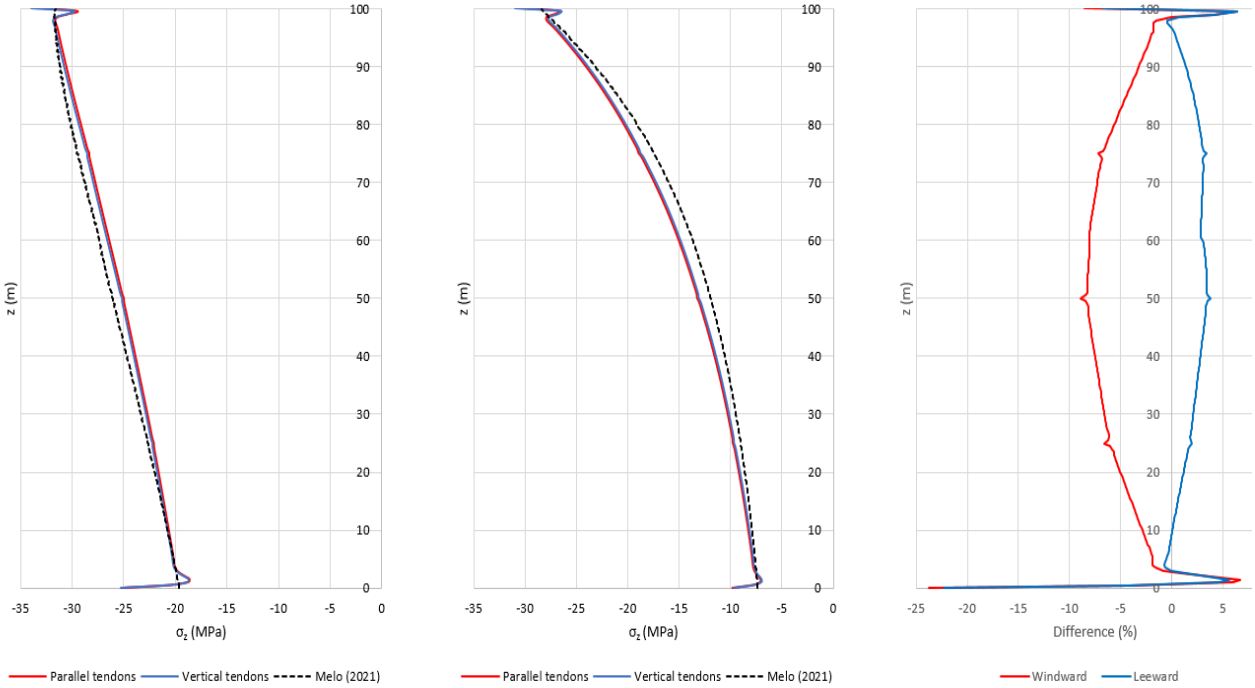

(a) Leeward (b) Windward (c) Difference

Source: elaborated by the author.

Figure 80 – Concrete vertical normal stress at ULS for the prestressing tendons placement analysis: a) Leeward, b) Windward

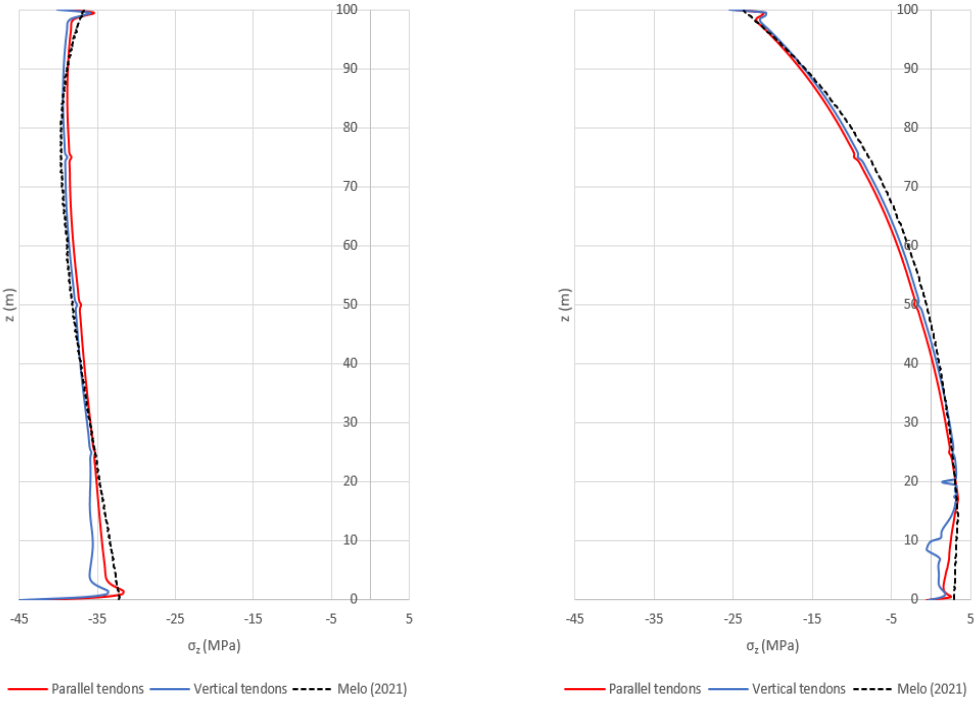

(a) Leeward (b) Windward

Source: elaborated by the author.

Concrete stress curves obtained by Melo (2021) model follows the same behavior as the ones obtained on the shell models, with the exception of the concentrated stresses at the bottom and top of the tower, but overall presenting a small numerical difference.

The vertical tendon stress is presented in Table 36 for the shell model in this present study and the beam model developed by Melo (2021). The difference between both models is small, therefore the beam model can accurately represent the prestressing tendons in this case and compute the correct stresses within a reasonable margin of error.

Table 36 – Vertical tendon stress at 100% wind load

Limit State	**Location**	**Tendon stress (MPa)**		**Difference**
		Present study	**Melo (2021)**	**(%)**
Serviceability	Windward	1116.6	1117.9	0.12
	Leeward	1079.9	1087.6	0.71
Ultimate	Windward	1151.4	1143.1	0.72
	Leeward	1042.7	1059.7	1.63

Source: elaborated by the author.

Figure 81 and Figure 82 illustrate the SLS and ULS tendons tensile stress, respectively, for both tendon configurations at the maximum wind load.

Figure 81 – Tendon stress for the SLS tendons placement analysis at 100% wind load: a) Vertical, b) Parallel

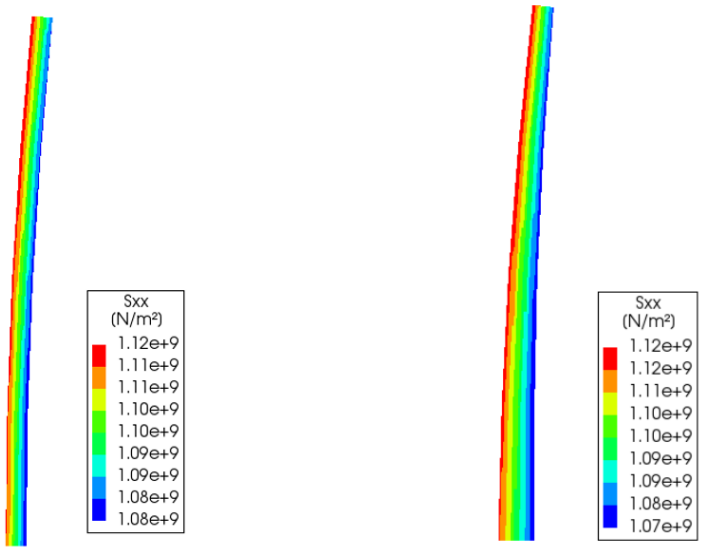

(a) Vertical (b) Parallel

Source: elaborated by the author.

Figure 82 – Tendon stress for the ULS tendons placement analysis at 100% wind load: a) Vertical, b) Parallel

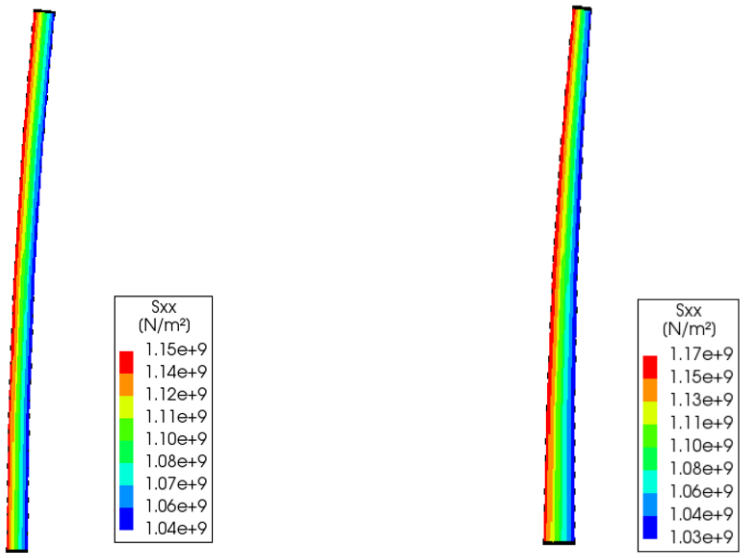

(a) Vertical (b) Parallel

Source: elaborated by the author.

Tendons' tensile for the parallel tendons, in comparison to the vertical cases, are lower at leeward and higher at windward.

5.2.6 Tendons distribution overt the tower height

From the previous analysis, it has been noted that the compressive stress on the concrete increase with the tower height, due to the tower section reduction with the height and the prestress force remaining the same, since all the prestressing tendons are anchored at the bottom and top of the tower. The main issue is that cracking usually occurs at the bottom of the tower, where the prestressing is actually needed. Thus, having greater compressive stress at the top of the tower is not cost-effective and may also surpass the concrete compressive strength on some occasions.

A practical and cost-effective method to reduce the compressive stress on top of the tower is to anchor some tendons along with the tower height, therefore, reducing the total prestress load on higher sections of the tower. This section is used to analyze the possibility of anchoring a portion of the tendons at half height of the tower, these are called half-length tendons, and the importance of properly distributing the prestress load across the tower section.

Figure 83 and Figure 84 illustrate a portion of the deflection curve for the SLS and ULS analysis, respectively, using various tendon distribution configurations. The figures show a small difference between them.

Figure 83 – Deflection for the prestressing tendons distribution analysis (SLS)

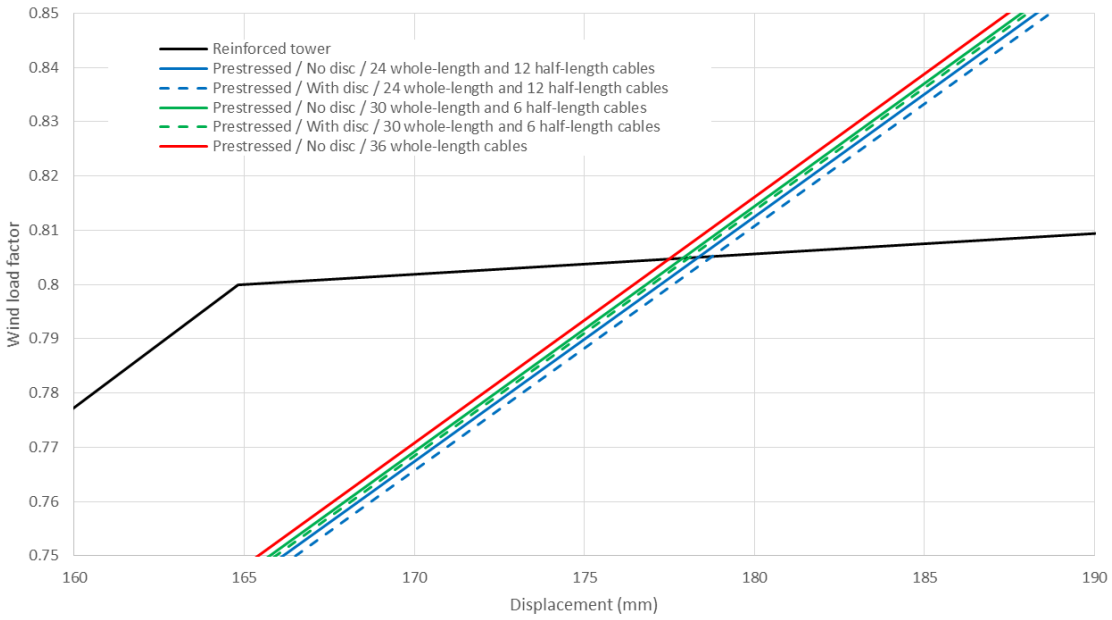

Source: elaborated by the author.

Figure 84 – Deflection for the prestressing tendons distribution analysis (ULS)

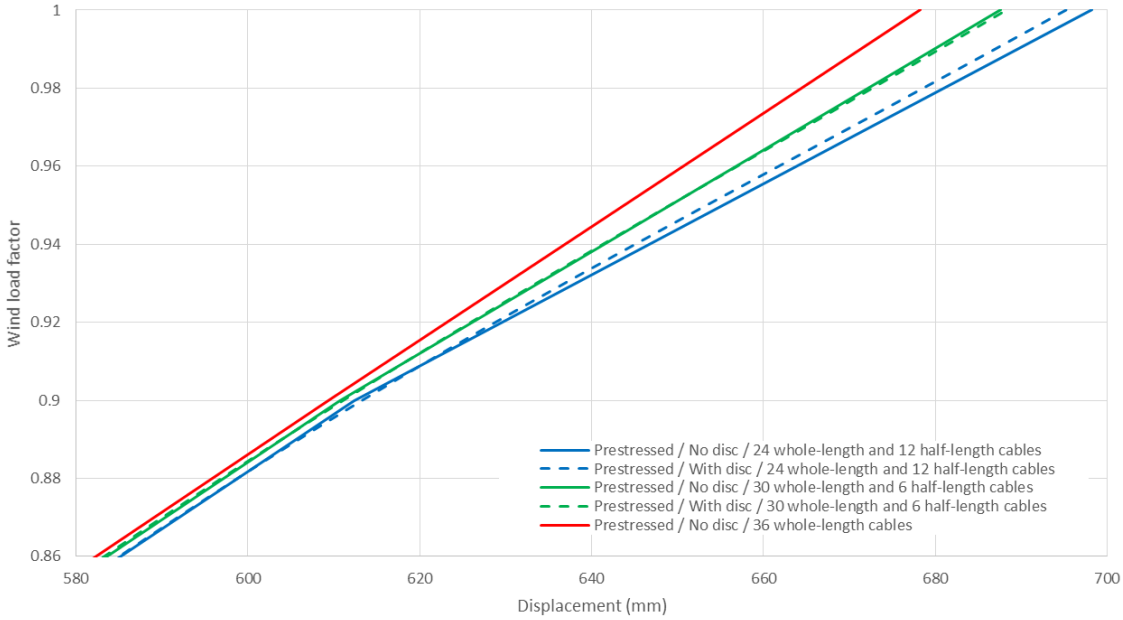

Source: elaborated by the author.

Table 37 and Table 38 show the frequency for uncracked and after-loading, wind load for cracking initiation and deflection on the top for the SLS and ULS analysis, respectively, using various tendon distribution configurations.

Table 37 – Results for the prestressing tendons distribution analysis (SLS)

Configuration		Uncracked frequency		After-loading frequency		Cracking initiation	Top deflection at 75%		Top deflection at 100%	
		Value (Hz)	Diff.[a] (%)	Value (Hz)	Diff.[a] (%)	Value[b] (%)	Value (mm)	Diff.[a] (%)	Value (mm)	Diff.[a] (%)
Reinforced tower		0.440	-	0.241	-	75	154.2	-	553.0	-
Prestressed tower without disc	36 whole-length tendons	0.418	-5.00	0.416	72.61	-	165.4	7.28	220.5	-60.12
	30 whole-length / 6 half-length tendons	0.419	-4.77	0.417	73.03	0	165.8	7.51	221.0	-60.04
	24 whole-length / 12 half-length tendons	0.420	-4.55	0.418	73.44	0	166.2	7.76	221.5	-59.94
Prestressed tower with disc	30 whole-length / 6 half-length tendons	0.418	-5.00	0.417	73.03	-	165.9	7.61	221.2	-60.00
	24 whole-length / 12 half-length tendons	0.419	-4.77	0.418	73.44	-	166.5	7.99	222.0	-59.86

[a] Comparison to the reinforced tower; [b] Percentage of the total wind load.

Source: elaborated by the author.

Table 38 – Results for the prestressing tendons distribution analysis (ULS)

Configuration		Uncracked frequency		After-loading frequency		Cracking initiation	Top deflection at 30%		Top deflection at 100%	
		Value (Hz)	Diff.[a] (%)	Value (Hz)	Diff.[a] (%)	Value[b] (%)	Value (mm)	Diff.[a] (%)	Value (mm)	Diff.[a] (%)
Reinforced tower		0.440	-	0.200	-	30	162.4	-	2201.7	-
Prestressed tower without disc	36 whole-length tendons	0.418	-5.00	0.411	105.50	90	203.2	25.11	678.3	-69.19
	30 whole-length / 6 half-length tendons	0.419	-4.77	0.392	96.00	0	203.6	25.37	687.6	-68.77
	24 whole-length / 12 half-length tendons	0.420	-4.55	0.382	91.00	0	204.0	25.63	698.2	-68.29
Prestressed tower with disc	30 whole-length / 6 half-length tendons	0.418	-5.00	0.390	95.00	90	203.8	25.49	688.3	-68.74
	24 whole-length / 12 half-length tendons	0.419	-4.77	0.383	91.50	70	204.5	25.94	695.3	-68.42

[a] Comparison to the reinforced tower; [b] Percentage of the total wind load.

Source: elaborated by the author.

When one analyzes the half-length tendon configuration without the steel disc, the cracking initiation occurs at 0% of the wind load, which is when the prestress loads are applied during the analysis, generating high concentrated stress on the tower wall.

The presence of the steel disc functions as an anchorage structure that properly distributes the half-length tendons prestress load across the tower section, instead of connecting all the displacements of the half-tendons' top nodes to the tower wall, which cause stress concentrations and cracking when applying the prestress load.

The 24 whole-length and 12 half-length tendons configuration reduced the cracking initiation to 70% of the wind load at ULS, whereas the 30 whole-length and 6 half-length cases maintained the 90% wind load. Thus, both are considered feasible configurations.

5.2.6.1 Concrete stress

To observe what happens in the tower during the tendon distribution analysis, it is important to analyze the concrete stress at leeward and windward. Figure 85 illustrates the concrete vertical normal stress along with the tower height at leeward, where the highest compressive stress occurs.

Figure 85 – Concrete vertical normal stress at leeward for the prestressing tendons distribution analysis: a) SLS, b) ULS

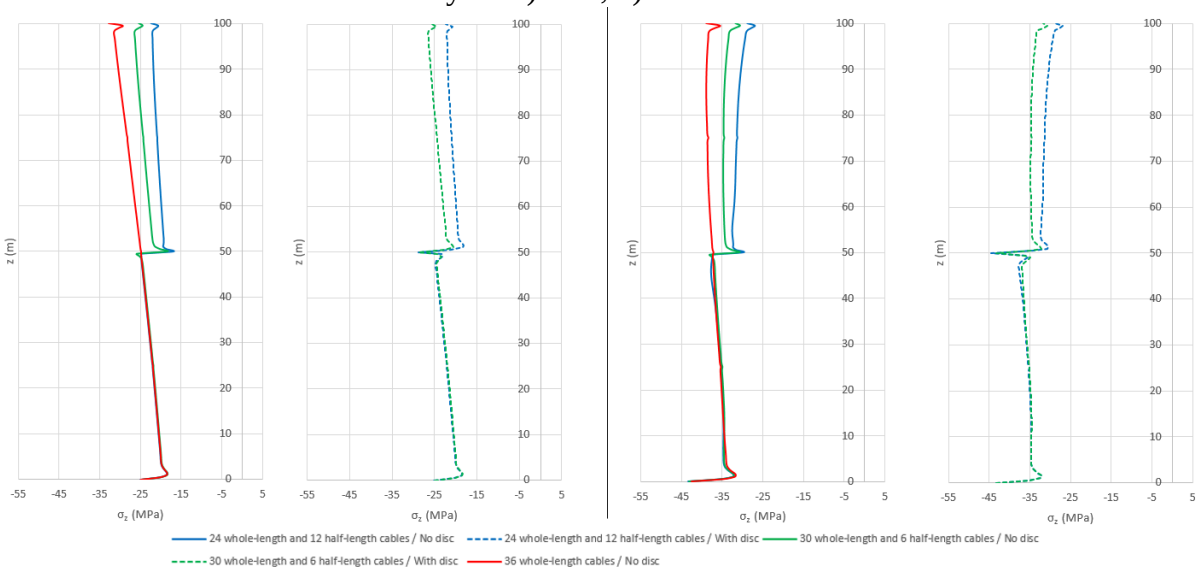

(a) SLS (b) ULS

Source: elaborated by the author.

The half-tendon cases managed to reduce the compressive stress at the top half of the tower, whereas the bottom half remained the same across all configurations. Figure 86

illustrates the concrete vertical normal stress along with the tower height at windward, where the lowest compressive stress or highest tensile stress occurs.

Figure 86 – Concrete vertical normal stress at windward for the prestressing tendons distribution analysis: a) SLS, b) ULS

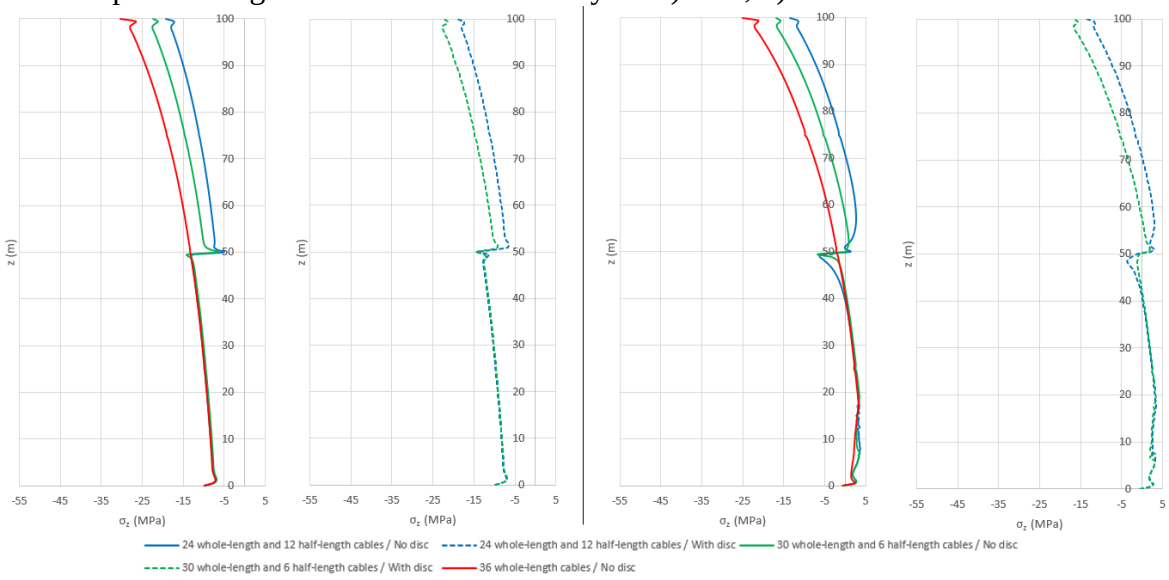

(a) SLS (b) ULS

Source: elaborated by the author.

The prestress load reduction at the top half of the tower also generated greater tensile stress at windward during the ULS analysis, by reducing the compressive stress on that section of the tower. The structural engineer must be careful not to reduce the prestress load, which could result in some sections of the tower cracking before expected when the tensile stress surpass the concrete tensile strength. A solution for this problem is to create more anchorage points along with the tower height, thus, gradually reducing the prestress load wherever necessary.

It is important to mention that thinner steel discs have been tested, but it lead to concrete cracking while the prestressing was being applied. Thus, demonstrating the importance of a well-designed anchorage structure and a more localized study.

5.2.7 Soil-structure interaction

This section analyzes the soil type that the tower will be built upon, the foundation itself and its effects on the prestressed tower global behavior.

The results for tower top deflection and fundamental frequency for SLS are presented in Table 39, whereas Figure 87 illustrates the tower top deflection versus wind load for various soil types.

Table 39 – Results for the soil-structure interaction analysis on prestressed tower (SLS)

Soil type and foundation configuration		**Uncracked frequency**		**After-loading frequency**		**Cracking initiation**	**Top deflection at 75%**		**Top deflection at 100%**	
		Value (Hz)	Diff.[a] (%)	Value (Hz)	Diff.[a] (%)	Value[b] (%)	Value (mm)	Diff.[a] (%)	Value (mm)	Diff.[a] (%)
No foundation / Fixed base		0.418	-	0.416	-	-	165.4	-	220.5	-
With foundation	Fixed	0.401	-4.07	0.401	-3.61	-	175.6	6.41	234.1	6.16
	Fine sand	0.349	-16.51	0.349	-16.11	-	218.6	32.16	291.4	32.15
	Sand	0.364	-12.92	0.364	-12.50	-	204.4	23.58	272.5	23.58
	Coarse sand	0.368	-11.96	0.368	-11.54	-	200.4	21.13	267.1	21.12
	Gravel	0.378	-9.57	0.378	-9.13	-	192.4	16.31	256.5	16.30
	Soft clay	0.288	-31.10	0.288	-30.77	-	298.6	80.54	398.1	80.51
	Clay	0.323	-22.73	0.323	-22.36	-	247.5	49.63	329.9	49.61
	Stiff clay	0.353	-15.55	0.353	-15.14	-	214.2	29.47	285.5	29.46

[a] Comparison to the no foundation / fixed base analysis; [b] Percentage of the total wind load.

Source: elaborated by the author.

Figure 87 – Deflection for the soil-structure interaction analysis on prestressed tower (SLS)

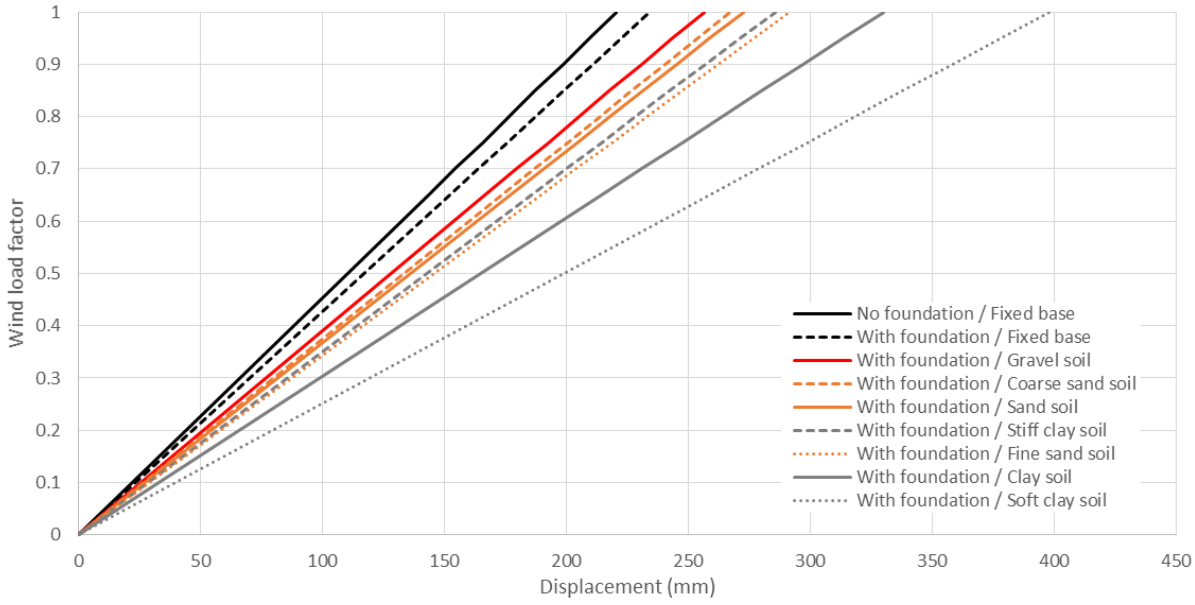

Source: elaborated by the author.

Overall, the prestressed tower presented a higher sensitivity to the soil types than the reinforced tower. The foundation itself is responsible for a 4.07% reduction in fundamental frequency due to its weight.

The percentage reduction on fundamental frequencies is significant for some types of soils, such as soft clay, with a 31.10% reduction in comparison to not considering the foundation and the soil-structure interaction. Although the prestressed tower suffers a great stiffness reduction caused by the soil-structure interaction, in none of the cases the fundamental frequency falls outside the turbine working frequency interval, which is important to avoid resonance. It is important to note that, in practice, the foundations are not the same for all those soils, but it was kept the same for comparison and research purposes only.

Table 40 presents a comparison between the fundamental frequencies obtained during this research and the ones obtained by Melo (2021). It is possible to observe that, for the SLS, the difference remains within a reasonable error, with a maximum of 4.51% difference on the uncracked fundamental frequency. For the ULS, cracking occurs within a smaller wind load for the shell model, due to the stress concentrations at the base. Thus, earlier cracking generates a greater decrease in the fundamental frequency, which explains the difference between the models.

Table 40 – Fundamental frequencies for the prestressed tower soil-structure interaction analysis

Limit State	**Soil type**	**Frequency (Hz)**		**Difference (%)**
		Present study	**Melo (2021) / 1 spring (rocking)**	
Serviceability (Uncracked)	Fine sand	0.349	0.348	-0.29
	Sand	0.364	0.367	0.82
	Coarse sand	0.368	0.373	1.36
	Gravel	0.378	0.383	1.32
	Soft clay	0.288	0.275	-4.51
	Clay	0.323	0.327	1.24
Ultimate (Cracked)	Fine sand	0.308	0.342	11.04
	Sand	0.322	0.362	12.42
	Coarse sand	0.325	0.368	13.23
	Gravel	0.352	0.379	7.67
	Soft clay	0.258	0.262	1.55
	Clay	0.286	0.319	11.54

Source: elaborated by the author.

5.3 Wind load analysis

This section presents the results obtained from the various wind load analysis on the reinforced concrete and prestressed tower. In the following topics, one investigates: an alternative to the wind and load combination model based on the ABNT NBR 6123 (2013) and ABNT NBR 6118 (2014), respectively; the importance of the direct wind load on the tower, to verify the reasons some researchers do not take into consideration during the analysis; a wind turbine with greater power output, therefore, with different wind turbine loads and working frequency; failure by excessive deformation.

The reinforced concrete and prestressed tower used in this section are the same as the standard ones presented in the previous sections.

5.3.1 Wind and load combination models

The results for tower top deflection and fundamental frequency for SLS are presented in Table 41, whereas Figure 88 illustrates the tower top deflection versus wind load for both wind and load combination models.

Figure 88 – Deflection for the wind and load combination models analysis (SLS)

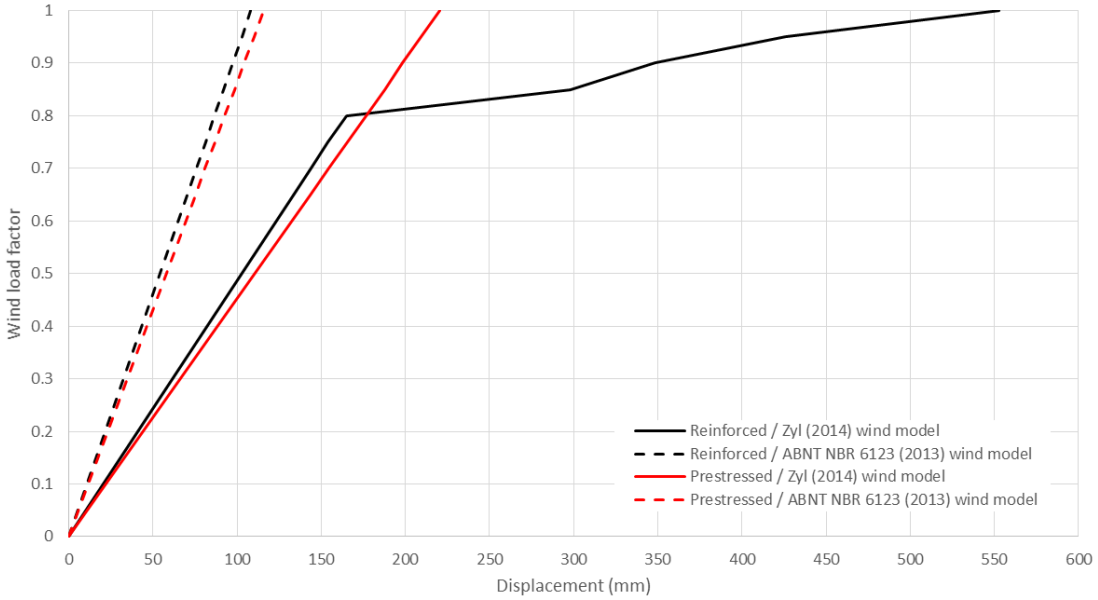

Source: elaborated by the author.

Table 41 – Results for the wind and load combination models analysis (SLS)

Type of tower	Wind and load combination model	Uncracked frequency		After-loading frequency		Cracking initiation	Top deflection at 75%		Top deflection at 100%	
		Value (Hz)	Diff.[a] (%)	Value (Hz)	Diff.[a] (%)	Value[b] (%)	Value (mm)	Diff.[a] (%)	Value (mm)	Diff.[a] (%)
Reinforced Tower	ABNT NBR	0.437	-0.68	0.437	81.33	-	81.1	-47.37	108.2	-80.43
	Zyl (2014)	0.440	-	0.241	-	75	154.2	-	553.0	-
Prestressed Tower	ABNT NBR	0.415	-0.72	0.413	-0.72	-	86.9	-47.49	115.8	-47.50
	Zyl (2014)	0.418	-	0.416	-	-	165.4	-	220.5	-

[a] Comparison to Zyl's model; [b] Percentage of the total wind load.

Source: elaborated by the author.

The SLS analysis results demonstrate a great difference between both wind models, particularly for the reinforced tower, since it cracked at 75% of the wind load at Zyl's model, whereas for the ABNT it did not crack. The after-loading frequency of the reinforced tower subjected to the ABNT NBR wind model is still the uncracked frequency, due to the much smaller wind load factor adopted in this model.

For the prestressed tower at SLS, both models presented similar results for the afer-loading frequency, although there is a great difference in deflection. This is because in both cases the tower remains uncracked until the end of the analysis.

Figure 89 illustrates the wind load at the windward of the tower with its respective wind load factor for each of the models at SLS.

Figure 89 – Wind load comparison at windward (SLS)

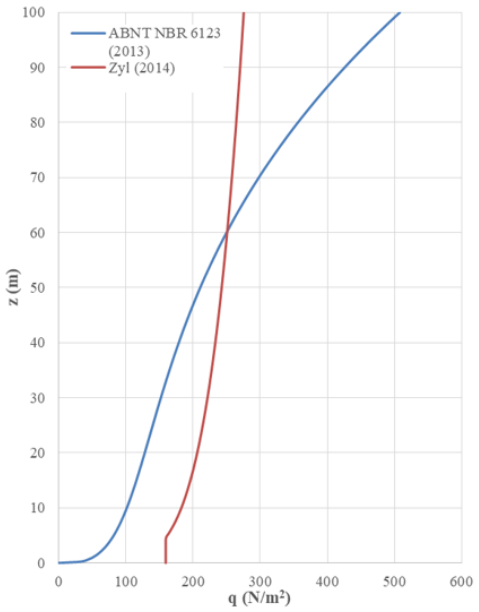

Source: elaborated by the author.

Although the difference between the SLS loads seems small, there is a greater difference on the tower global behavior results differ during the analysis. This is explained by the load factors adopted for the other loads: the load combination for the ABNT NBR model presents a greater difference between the unfavorable loads (wind) and favorable loads (structure self-weight and prestressing), decreasing the former and increasing the self-weight, whereas Zyl's model presents a more similar factor between the loads;

It is important to highlight that the wind model and load combination present on the ABNT NBR 6123 (2013) and ABNT NBR 6118 (2014), respectively, are not specified for wind towers. Zyl's model is a high fidelity model for wind and load combination in wind towers and the tower subject to this model produced results with greater deflections.

5.3.2 Effect of direct wind load on the tower

The results for tower top deflection and fundamental frequency for SLS are presented in Table 42, whereas Figure 90 illustrates the tower top deflection versus wind load with and without wind pressure on tower.

Figure 90 – Deflection for the effect of direct wind load on tower analysis (SLS)

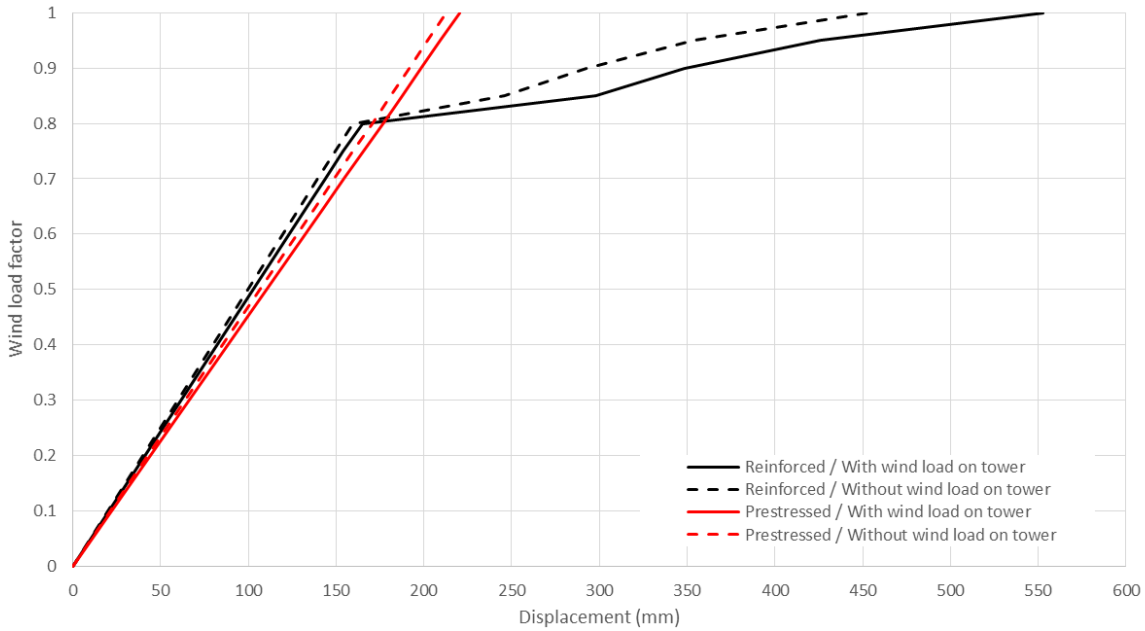

Source: elaborated by the author.

Table 42 – Results for the effect of direct wind load on tower analysis (SLS)

Type of tower	Direct wind load on tower	Uncracked frequency		After-loading frequency		Cracking initiation	Top deflection at 75%		Top deflection at 100%	
		Value (Hz)	Diff.[a] (%)	Value (Hz)	Diff.[a] (%)	Value[b] (%)	Value (mm)	Diff.[a] (%)	Value (mm)	Diff.[a] (%)
Reinforced Tower	Not considered	0.440	0.00	0.268	11.20	75	149.4	-3.08	452.2	-18.22
	Applied	0.440	-	0.241	-	75	154.2	-	553.0	-
Prestressed Tower	Not considered	0.418	0.00	0.416	0.00	-	159.7	-3.46	212.9	-3.46
	Applied	0.418	-	0.416	-	-	165.4	-	220.5	-

[a] Comparison to the applied wind load case; [b] Percentage of the total wind load.

Source: elaborated by the author.

The prestressed tower has a relatively small difference in the deflection for the SLS analysis when one does not consider the direct wind load on the tower. For the reinforced tower, the difference is greater after cracking, getting up to 18.22% smaller deflection at 100% wind load and a higher after-loading frequency, since the tower suffered less strain.

5.3.3 Tower analysis with a 5.0 MW turbine

In this topic, one presents an investigation on the tower's behavior as it is subjected to a turbine with greater power output. For this analysis, it is important to mention the new loads, working frequency and turbine specifications, which are presented in Tables 45, 43 and 44, respectively.

Table 43 – 5.0 MW turbine loads

	Thrust force (kN)	Overturning moment (kNm)	Axial force – causing tower compression (kN)	Torsional moment – about tower longitudinal axis (kNm)
EWM	578	28568	4998	5834
EOG	1065	19337	4879	3714

Source: LaNier (2005).

Table 44 – Working frequency of 5.0 MW turbine

	Operation speed – 1P (rpm)	1P (Hz)	3P (Hz)	Working frequency limits	
				1.1P (Hz)	2.7P (Hz)
5.0 MW constant speed	11.2	0.186	0.559	0.205	0.503

Source: LaNier (2005).

Table 45 – 5.0 MW turbine specifications

Power output	5.0 MW
Rotor speed	11.2 rpm
Rotor diameter	128 m
Head mass (including nacelle, hub and blades)	480076 kg
Hub height	100 m
IEC class	IIB

Source: LaNier (2005).

The results for tower top deflection and fundamental frequency for SLS are presented in Table 46, whereas Figure 91 illustrates the tower top deflection versus wind load for both turbines.

Table 46 – Results for the 5.0 MW turbine analysis (SLS)

Type of tower	**Turbine output**	**Uncracked frequency**		**After-loading frequency**		**Cracking initiation**	**Top deflection at 75%**		**Top deflection at 100%**	
		Value (Hz)	Diff.[a] (%)	Value (Hz)	Diff.[a] (%)	Value[b] (%)	Value (mm)	Diff.[a] (%)	Value (mm)	Diff.[a] (%)
Reinforced Tower	5.0 MW	0.383	-12.95	0.230	-4.56	75	158.7	2.91	509.0	-7.95
	3.6 MW	0.440	-	0.241	-	75	154.2	-	553.0	-
Prestressed Tower	5.0 MW	0.366	-12.44	0.364	-12.50	-	169.8	2.68	226.4	2.68
	3.6 MW	0.418	-	0.416	-	-	165.4	-	220.5	-

[a] Comparison to the 3.6 MW turbine; [b] Percentage of the total wind load.

Source: elaborated by the author.

Figure 91 – Deflection for the 5.0 MW turbine analysis (SLS)

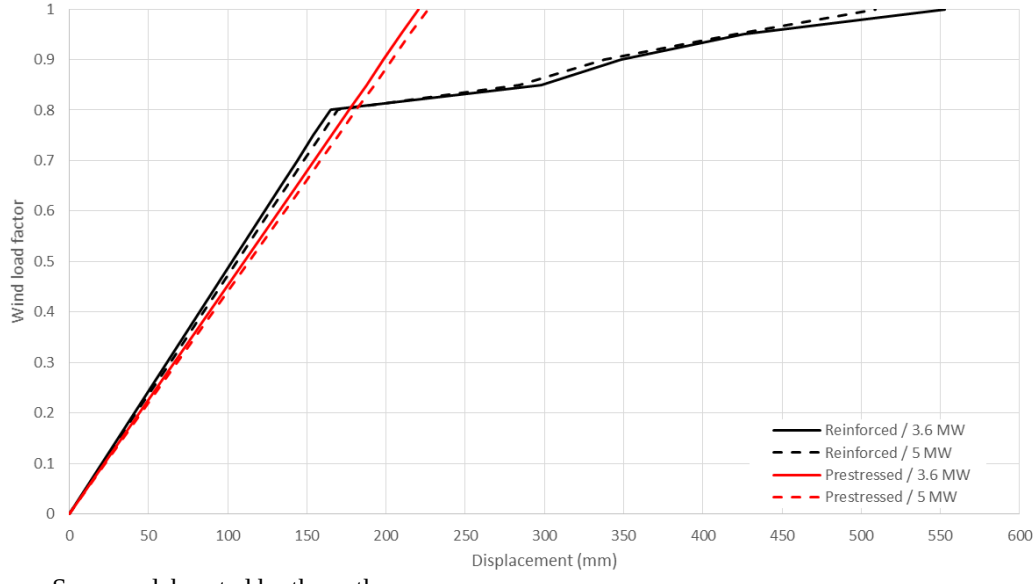

Source: elaborated by the author.

The greater head mass of the 5.0 MW turbine caused a decrease in the fundamental frequency of the tower, but, as mentioned before, the structure self-weight is actually a favorable load for wind turbines.

The linear section of the deflection curves at SLS for both reinforced and prestressed towers presented a small increase in deflection for the 5.0 MW turbine cases. The reinforced tower deflection curve maintained a similar behavior between the 5.0 MW and 3.6 MW cases after cracking. Both towers remain within the working frequency limits of the 5.0 MW turbine.

The results for tower top deflection and fundamental frequency for ULS are presented in Table 47, whereas Figure 92 illustrates the tower top deflection versus wind load for both turbines.

Table 47 – Results for the 5.0 MW turbine analysis (ULS)

Type of tower	**Turbine output**	**Uncracked frequency**		**After-loading frequency**		**Cracking initiation**	**Top deflection at 30%**		**Top deflection at 100%**	
		Value (Hz)	Diff.[a] (%)	Value (Hz)	Diff.[a] (%)	Value[b] (%)	Value (mm)	Diff.[a] (%)	Value (mm)	Diff.[a] (%)
Reinforced Tower	5.0 MW	0.383	-12.95	0.181	-9.50	40	134.2	-17.39	1740.6	-20.94
	3.6 MW	0.440	-	0.200	-	30	162.4	-	2201.7	-
Prestressed Tower	5.0 MW	0.366	-12.44	0.361	-12.17	-	166.8	-17.91	555.7	-18.07
	3.6 MW	0.418	-	0.411	-	90	203.2	-	678.3	-

[a] Comparison to the 3.6 MW turbine; [b] Percentage of the total wind load.

Source: elaborated by the author.

Figure 92 – Deflection for the 5.0 MW turbine analysis (ULS)

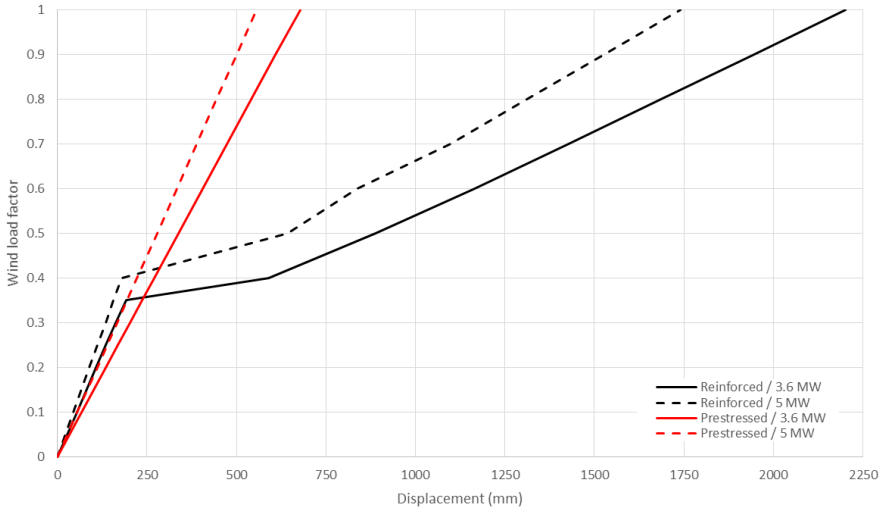

Source: elaborated by the author.

For the ULS, both reinforced and prestressed towers presented an overall decrease in the deflection for the 5.0 MW turbine cases and an increase in the wind load level for cracking initiation. The reasons for the deflection decrease might be that not every load from 5.0 MW is greater than the 3.6 MW turbine (thrust and torsion loads are actually smaller) and the greater head mass from the 5.0 MW turbine is beneficial for resisting bending.

5.3.4 Critical wind load

The standard prestressed tower did not present excessive cracking within the load limits of the wind model adopted in this study in the previous analysis. In this topic, one presents an investigation on the tower's behavior as it is subjected to greater wind loads, until the convergence criteria are not met on the software.

It is important to mention that this analysis is for research purposes only, since it is unlikely that wind loads from the tower site and conditions can reach levels beyond the 100% ULS wind load. The equilibrium path can be analyzed to identify critical points and the structure's behavior with greater loads.

Figure 93 – Deflection for the failure by excessive deformation analysis (ULS)

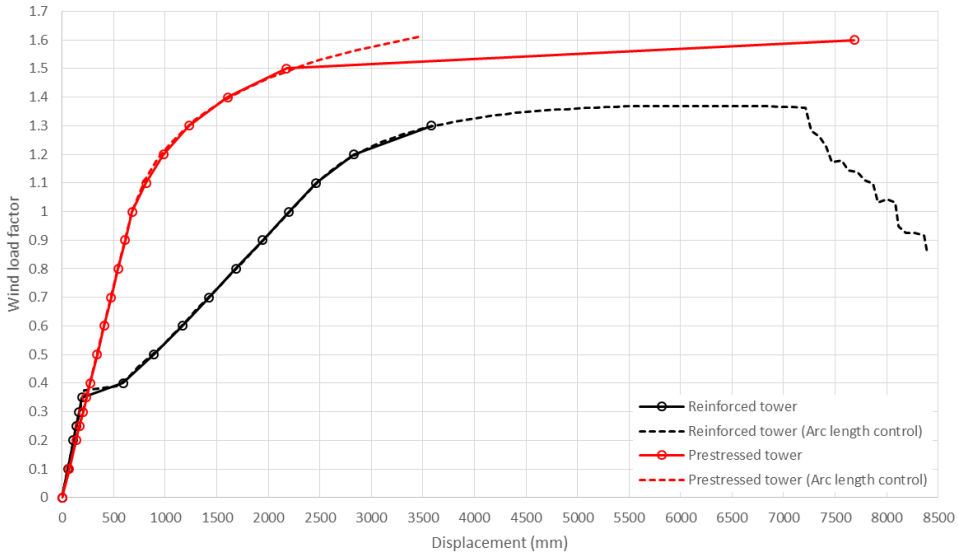

Source: elaborated by the author.

It is observed in Figure 93 that both the reinforced and prestressed tower equilibrium paths demonstrate an imperfect stable behavior, but the prestressed tower presents a higher critical point.

6 CONCLUSIONS

This study presented a geometric and material nonlinear high fidelity model and analyzed the behavior of prestressed wind towers. The finite element analysis software DIANA has been used, making use of shell, reinforcement and cable elements to accurately model the tower for various configurations and parametric analyses.

The summarization of the recommended finite element, methods and parameters configurations for the prestress tower based on the results is presented in Table 48.

Table 48 – Recommended finite element, methods and parameters configurations for the prestressed tower

Description	**Configurations**
Iterative method	Standard Newton-Raphson
Type of geometrical nonlinearity	Total Lagrangian
Convergence norm	Displacement and force
Solution method	Parallel direct sparse
Element type	Quadratic
Circumferential pressure distribution	Quadratic
Torsion load	Average shear stress
Thrust load	All nodes
Ring material	Steel
Turbine mass	Distributed
Nonlinearity	Geometric and Material
Wind and load combination models	Zyl (2014)
Deviators	Deviator-guided
Vertical reinforcing steel	Minimum value according to ACI-307 (2008)
Prestress load	Must be evaluated according to each tower design (100% for the example evaluated, based on the value present in Table 13)
Tendons placement	Parallel and closer to the tower wall
Half-length cables anchorage	Steel disc

Source: elaborated by the author.

It was possible to observe that prestressed wind turbine towers play a vital role in ensuring the progress of large-scale wind turbines. The results obtained from this research can help to further develop prestressed wind towers, revealing important points to the design of wind towers.

Even though it is known that prestressed and hybrid towers are the most adequate solutions for wind towers over 100 m, being more cost-effective and having a lower maintenance cost in comparison to the traditional steel towers, there are few researches done until the moment for prestressed towers.

It is important to observe that, for most of the reinforced tower cases analyzed, fundamental frequency after-loading falls outside the 1.1P working frequency of the turbine (<0.242 Hz) due to cracking, even for the SLS cases. This could increase the likelihood of resonance, resulting in the structure suffering large displacements or even immediate failure. That can be solved by increasing the tower stiffness or decreasing the mass of the tower. Another way to avoid the reduction of the fundamental frequency after-loading is to reduce cracking by inserting prestressing forces into the structure.

Researches on the optimization of the design of those towers have sought more economical solutions by exploring simple models, seeking efficiency in solving the optimization problem. This work has shown the importance of exploring high fidelity models before finding simpler solutions, to make sure it can be considered conservative for the problem. Making use of a shell finite element model with cables and reinforcing elements, various aspects of the tower's behavior and configurations have been explored, revealing important points to the design of prestressed wind towers and contributions to the optimization process, that could be otherwise ignored while using less refined models.

The comparison between the high fidelity method presented during this research and the improved beam element method used for optimization demonstrates the importance of a more refined analysis. Some aspects can only be observed during the high fidelity analysis, such as the correct tower frequencies and modes; the deviators and their effects on the tower's behavior; localized stresses caused by anchorage and different material interfaces; detailed crack patterns.

Melo's (2021) beam element model results offered a relatively good approximation of the tower global behavior in comparison to the high fidelity model, which is important to validate its viability to be used for optimization purposes. Also, a multi-fidelity model can be used combining high fidelity models with low fidelity simulations (RIBEIRO, 2022).

Another important aspect to take into consideration for optimization is the processing time required for the analysis, which is computationally intensive for this kind of problem. Therefore, this high fidelity model must be used for design validations or alongside a surrogate model for optimization. The modified Newton-Raphson iterative method can be used for optimization purposes without further problems.

It has been found that the best way to avoid the reduction of concrete tensile strength due to the element type and size is to use quadratic elements, which are able to capture with more precision the stress concentrations within the element.

The difference between the chosen methods to simulate the torsion load is insignificant, which is explained by the stiffness of the ring. Although the average shear stress method is more refined and accurate, the perpendicular method is simpler to implement, but might cause deformations on the ring if the material is not rigid enough.

Both methods evaluated to simulate the thrust load may also be adopted, but it is recommended to apply the loads on each node of the ring, to better represent the yaw mechanism connection on the tower.

Turbine mass must be distributed at the top nodes of the ring, since a concentrated mass at the tower axis requires to connect the translation of the top edge nodes. These connections prevent some modes that appear on the distributed mass analysis to be computed, leading to inaccurate results. If the nacelle and blade's center of mass is localized on the top of the vertical axis and the connection between the nacelle and the tower is sufficiently rigid, then the concentrated mass method can be used to model the turbine mass.

A rigid material must be avoided for the ring on top of the tower, to prevent numerical errors in the analysis caused by the great difference in material stiffness in the tower and ring interface. Therefore, it is recommended to use the steel material for the ring.

The nonlinearity used in the model is another important aspect that has been evaluated, which leads to a better understanding of how the prestress forces influence the fundamental frequency of the tower. The increase in the prestress load generates a decrease in the fundamental frequency, which, according to the results, can be caused predominantly by its effect on the structure's geometric stiffness matrix when one analyzes the tower considering the geometric nonlinearity. For higher levels of prestressing, the nonlinear nature of the steel and concrete begins to contribute to the stiffness reduction.

Zyl's (2014) model for wind and load combination is better adapted for wind towers, whereas ABNT NBR 6123 (2013) model is specified for chimneys and mostly underestimates wind loads, which leads to a significant difference between both models.

The presence of deviators on the prestressed tendons is essential for the externally prestressed wind tower design and analysis. The absence of deviator-guided tendons might produce an unrealistic physical configuration with tendons usually breaking through the tower wall.

The number of prestressed tendons modeled was limited by the amount of circumferential sections on the tower during the analysis, due to how the deviators are applied. For the case study, it has been proven that the number of modeled tendons made little to no difference in the tower's global behavior while keeping the same total steel area and axisymmetric distribution. Although, if the number of tendons designed is greater than the tower shell circumferential divisions, it is suggested a greater refinement of the tower mesh so that both must be equal.

There was little increase in the tower stiffness caused by the vertical reinforcing steel application on the tower, which is not significant for the required volume of steel. Thus, it is recommended to use the minimum vertical reinforcing steel proposed by the ACI-307 (2008).

The prestress load must be evaluated according to each case. It is important to take into consideration the following aspects when evaluating the ideal prestress load for the structure: cracking initiation at SLS; deflection on the top at SLS; fundamental frequency, as increase on the prestress load will most likely decrease the uncracked frequency; there must be no tensile stress in the concrete during SLS; compressive stress in the concrete, as to not reach concrete compressive strength; cracking pattern and maximum crack width during SLS.

Tendons parallel to the wall presented an overall better performance than the vertical placement and, although the distance to the wall did not change significantly the global behavior of the tower significantly, the tendons should be placed closer to the walls to reduce the size of deviators structures and increase the tower stiffness.

The tendon distribution must be properly evaluated for each case, but anchoring a portion of the tendons along with the tower height can be used to reduce the compressive stress at higher sections of the tower caused by the prestress load. This method can properly avoid excessive compressive stress on higher sections, but it could also lead to greater tensile stress at windward, which should also be taken into consideration during the design process. The importance of a proper anchorage structure for these tendons has also been verified for the analyzed tower, as the steel disc inserted as an anchorage structure could distribute the half-length tendons' prestress load across the tower section, avoiding stress concentrations and cracking when applying the prestress load.

The soil-structure interaction implementation for the analysis model has also been evaluated and, although it presented a significant reduction in the tower stiffness, in none of the prestressed tower cases the fundamental frequency falls outside the turbine working frequency interval, unlike what happened for the reinforced tower. This evaluation showed the importance

of the soil-structure implementation during the analysis and how the prestress is a better solution to better avoid soil-related problems that might appear during the structure lifespan.

The standard prestress tower studied in this research was suitable for the 3.6 MW turbine, avoiding tensile stresses on the concrete and staying within the limits of: 33.1 MPa maximum compressive stress from ACI-318 (2019); no tensile stress in the concrete during SLS; 1.25 m maximum horizontal drift limit from Nicholson (2011); the working frequency range of the turbine.

The presence of direct wind pressure on the tower led to a decrease in the wind load for cracking initiation and a significant increase in the tower top deflection. This effect was especially noted in the reinforced tower case, which also suffered a decrease in the after-loading frequency during SLS, falling outside the turbine working frequency interval. These results demonstrate the importance of taking into consideration the direct wind load on the tower during the analysis.

The high fidelity analysis model for wind towers is easily adapted for various situations, as demonstrated by the many investigations developed in this research. The direct wind loads on the tower and turbine can be changed to adapt to diverse wind environments, sites and turbines. Prestress tendon and loads are properly modeled and applied, as various solutions are presented to circumvent problems such as stress concentrations and compressive stress at the top of the tower. The model is also able to simulate the soil conditions the tower will be built upon.

Further investigations must be performed to obtain a more detailed design for prestressed wind towers, focusing on obtaining the actual turbine loads from manufacturers, evaluation of the fatigue limit state of prestressed towers, the use of this high fidelity model on optimization procedures alongside a surrogate model.

REFERENCES

ABEEOLICA. Associação Brasileira de Energia Eólica. **InfoVento nº 11**, Bela Vista – SP, maio, 2019. Available at: http://abeeolica.org.br/wp-content/uploads/2019/05/Infovento-11_PT.pdf. Accessed on: 21 Feb. 2020.

ABNT. **NBR 6123: Forças devidas ao vento em edificações**. Associação Brasileira de Normas Técnicas. Rio de Janeiro, 2013.

ABNT. **NBR IEC 61400-1: Aerogeradores - Parte 1: Requisitos de Projeto.** Associação Brasileira de Normas Técnicas. Rio de Janeiro, 2008.

ABNT. **NBR 6118: Projeto de Estruturas de Concreto - Procedimento.** Associação Brasileira de Normas Técnicas. Rio de Janeiro, 2014.

AMERICAN CONCRETE INSTITUTE. **ACI-224: Causes, evaluation, and repair of cracks in concrete structures**. [*S. l.*], 2007.

AMERICAN CONCRETE INSTITUTE. **ACI-307: Design and Construction of Reinforced Concrete Chimneys**. [*S. l.*], 2008.

AMERICAN CONCRETE INSTITUTE. **ACI-318: Building Code Requirements for Structural Concrete**. [*S. l.*], 2019.

AMERICAN SOCIETY OF CIVIL ENGINEERS. **ASCE 7-16: Minimum Design Loads and Associated Criteria for Buildings and Other Structures**. [*S. l.*], 2016.

ARAÚJO, T.G; DE MELO, A.M.C; ARAÚJO, T.D.P. Otimização de torres eólicas de concreto armado. **Proceedings of the XIII Simpósito de Mecânica Computacional (SIMMEC)**, Vitória, 2018.

BACHMANN, H.; AMMANN, W.J.; DEISCHL, F.; EISENMANN, J.; FLOEGL, I.; HIRSCH, G.H.; KLEIN, G.K.; LANDE, G.J.; MAHRENHOLTZ, O.; NATKE, H.G.; NUSSBAUMER, H.; PRETLOVE, A.J.; RAINER, J.H.; SAEMANN, E.U.; STEINBEISSER, L. **Vibration problems in structures**. Berlin: Birkhauser Verlag, 1995.

BAI, H; CHERFILS, J.M.; AOUES, Y.; LEMOSSE, D. Optimization of a tall Wind turbine tower. *In*: S19-Congrés Français de Mécanique, Lille, 2017.

BARROSO FILHO, N.F. **Um estudo comparativo de procedimentos de análise estrutural para torres eólicas de concreto armado**. 2018. Master's Thesis (Mestrado em Engenharia Civil) – Centro de Tecnologia, Programa de Pós-Graduação em Engenharia Civil: Estruturas e Construção Civil, Universidade Federal do Ceará, Fortaleza, 2018.

BRASIL, R.M.L.R.F.; PAULETTI, R.M.O.; CARRIL JÚNIOR, C.F.; LAZANHA, E.C. Efeito do vento sobre uma torre de telecomunicações em concreto pré-moldado. *In*: SIMPÓSIO EPUSP SOBRE ESTRUTURAS DE CONCRETO, 5. 2003. São Paulo. **Proceedings of** [...] São Paulo: USP, 2003. pp. 1-16. Available at: http://www.lmc.ep.usp.br/people/pauletti/Publicacoes_arquivos/SIMP67-Efeito%20do%20Vento.pdf. Accessed on: 14 Feb. 2020.

BRASIL, R.M.L.R.F.; SILVA, M.S.P.E. Ánalise Dinâmica Não-Linear De Torres Em Concreto Armado Submetidas Ao Vento Sintético. **Revista Interdisciplinar de Pesquisa em Engenharia**, v. 22, n. 1, 2016.

BLOOMBERG NEW ENERGY FINANCE. **Climate Changed: Clean Energy is Approaching a Tipping Point. 2017.** Available at: https://www.bloomberg.com/news/articles/2017-09-19/tipping-point-seen-for-clean-energy-as-monster-turbines-arrive. Accessed on: 17 Feb. 2020.

CEB-FIB. **Model Code 2010**. Switzerland: International Federation for Structural Concrete (fib), 2010.

COLLINS, M.P.; MITCHELL, D. **Material Properties:** *Prestressed Concrete Structures*. Prentice-Hall Inc.: NJ, 1991.

DIANA FEA 10.3. **Diana (DIsplacement ANAlyser) user's manual**. In: Denise, F. (Ed.). Netherlands: DIANA FEA $_{BV}$, 2019.

DNV; RISO. **Guidelines for the Design of Wind Turbines**. 2nd ed. Denmark: Det Norske Veritas (DNV) and Riso National Laboratory, 2002.

DUARTE, T.G.A. **Um modelo eficiente para otimização de torres eólicas de concreto armado via algoritmos genéticos**. 2019. Master's Thesis (Mestrado em Engenharia Civil) – Centro de Tecnologia, Programa de Pós-Graduação em Engenharia Civil: Estruturas e Construção Civil, Universidade Federal do Ceará, Fortaleza, 2019.

FOLSTER, K. **Influence of geometry on the dynamic behavior of steel tubular towers for onshore wind turbines**. 2016. Master's Thesis (Mestrado em Engenharia Civil) – University of Cape Town, Cape Town, 2016.

GAMA, P. V. C. N. **Contribuições ao dimensionamento de torres eólicas de concreto**. 2015. Master's Thesis (Mestrado em Engenharia Civil) – Universidade de São Paulo, São Paulo, 2015.

GAZETAS, G. Analysis of machine foundation vibrations: state of the art. **Soil Dynamics and Earthquake Engineering**, v.2, n.1, 1983.

GLOBAL WIND REPORT. **Annual Market update 2013**. [*S. l.*]: Gwec, 2013. Available at: http://www.gwec.net/wp-content/uploads/2014/04/GWEC-Global-Wind-Report_9-April-2014.pdf. Accessed on: 18 Feb. 2020.

GRÜNBERG, J.; GÖHLMANN, J. (Org.). **Concrete Structures for Wind Turbines**. Berlim: Wilhelm Ernst & Sohn, 2013.

GWEC. Global Wind Energy Council, **Global Wind Report 2018**. Bruxelas, 2019.

HAU, E. **Wind Turbines**. [s.l.]: Springer Berlin Heidelberg, 2013.

HENDRIKS, M.A.N; DE BOER, A.; BELLETTI, B. **Guidelines for Nonlinear Finite Element Analysis of Concrete Structures**. Rijkswaterstaat Centre for Infrastructure, Report RTD:1016-1:2017, 2017.

IEC. **61400-1 Wind Turbines - Part 1: Design Requirements**. International Electrotechnical Commission. Geneva, 2005.

IRENA. **Renewable energy technologies: cost analysis series**. International Renewable Energy Agency, 2012.

KENNA, A.; BASU, B. A finite element model for prestressed or post-tensioned concrete wind turbine towers. **Wind Energy**, v. 18, p. 1593-1610, 2015.

LANA, J. A.; JÚNIOR, P. A. A. M.; MAGALHÃES, C. A.; MAGALHÃES, A. L. M. A.; ANDRADE JUNIOR, A. C.; RIBEIRO, M. S. B. Behavior study of prestressed concrete wind-turbine tower in circular cross-section. **Engineering Structures**, v. 227, p. 111403. Elsevier BV, 2021.

LANIER, M. W. **LWST Phase I Project Conceptual Design Study: Evaluation of Design and Construction Approaches for Economical Hybrid Steel/Concrete Wind Turbine Towers**. June 28, 2002 -- July 31, 2004. n. Jan. 2005.

MA, H. W.; MENG, R. Optimization of prestressed concrete wind-turbine tower. **Science China Technological Sciences**, v. 57, pp. 414-422, 2014.

MANWELL, J. F.; MCGOWAN, J. G.; ROGERS, A. L. **Wind Energy Explained**. 2nd ed. Wiley Online Library, 2009.

MELO, M.A. **Otimização de torres protendidas para turbinas eólicas**. 2021. Master's Thesis (Mestrado em Engenharia Civil) – Centro de Tecnologia, Programa de Pós-Graduação em Engenharia Civil: Estruturas e Construção Civil, Universidade Federal do Ceará, Fortaleza, 2021. Unpublished manuscript.

MOLINA, M.G.; MERCADO, P.E. Modelling and control design of pitch-controlled variable speed wind turbines. **Wind Turbines**. InTech, 2011.

NICHOLSON, J. **Design of wind turbine tower and foundation systems: optimization approach**. 2011. Master's Thesis (Master in Civil and Environmental Engineering), University of Iowa, Iowa, 2011.

RAFI, M.M.; NADJAI, A.; ALI, F. Analytical Modeling of Concrete Beams Reinforced with Carbon FRP Bars. **Journal of Composite Materials**, v. 41, n. 22, p. 2675-2690, 2007.

REHMAN, S.; ALAM, M.; ALHEMS, L. M. Horizontal axis wind turbine review with emphasis on tower structural stability, failure issues, and remedial measures in practice in wind power industries. **Proceedings of the 2019 World Congress on Advances in Structural Engineering and Mechanics (ASEM19)**, Jeju Island, 2019.

RIBEIRO, L. G. **Efficient Optimization Of Composite Structures Using Multi-Fidelity Models**. 2022. Master's Thesis (Mestrado em Engenharia Civil) – Centro de Tecnologia, Programa de Pós-Graduação em Engenharia Civil: Estruturas e Construção Civil, Universidade Federal do Ceará, Fortaleza, 2022. Unpublished manuscript.

SANS 10160-3. **Basis of structural design and actions for buildings and industrial structures Part 3**: Wind actions. [*S.l.*]: SABS, 2011.

SILVEIRA, M.C.A. Torres eólicas em concreto. **Revista da Academia Cearense de Engenharia**, v.2, n.2, p. 152-161, 2017.

THE CONCRETE CENTRE & GIFFORD. **Concrete Towers for Onshore and Offshore Wind Farms**: Conceptual Design Studies. London, 2006.

THE NETHERLANDS ORGANISATION. Diana's user manual. *In*: THE NETHERLANDS ORGANISATION. **Element Library**. [*S.l.*]: Netherlands Organisation, 2012.

THORENFELDT, E.; TOMASZEWICZ, A.; JENSEN, J.J. Mechanical Properties of High-strength Concrete and Application in Design. **Proceedings of the Symposium on the Utilization of High-Strength Concrete**, Trondheim, p. 149-159, 1987.

TOMCZAK, J.S. **Finite element analysis of post-tensioned concrete wind turbine towers**. 2021. Master's Thesis (Master of Science), University of Minnesota, Minnesota, 2021.

VON DER HAAR, C.; MARX, S. Design aspects of concrete towers for wind turbines. **Journal of the South African Institution of Civil Engineering**, v. 57, n. 4, p. 30-37, 2015.

WIND TURBINE MODELS. **Vestas V126-3.45**, 2016. Available at: https://en.wind-turbine-models.com/turbines/1249-vestas-v126-3.45. Accessed on: 05 Apr. 2020.

YANG, Z. **Wind Turbine Controls in Wind Farm and Offshore Operation**, Thesis (Doctor of Philosophy in Engineering) – University of Wisconsin-Milwaukee, Milwaukee, 2013.

ZYL, W. S. V. **Concrete Wind Turbine Towers in Southern Africa**, Master's Thesis (Master in Civil Engineering) – Stellenbosch University, Stellenbosch, 2014.

ZYL, W. S.V.; ZIJL, G. P. A. G. V. Dynamic behavior of normally reinforced concrete wind turbine support structures. **Journal of the South African Institution of Civil Engineering**, v. 57, pp. 38-44, 2015.

APPENDIX A – FLOWCHART FOR BASIC WIND SPEED EVALUATION ACCORDING TO IEC 61400-1

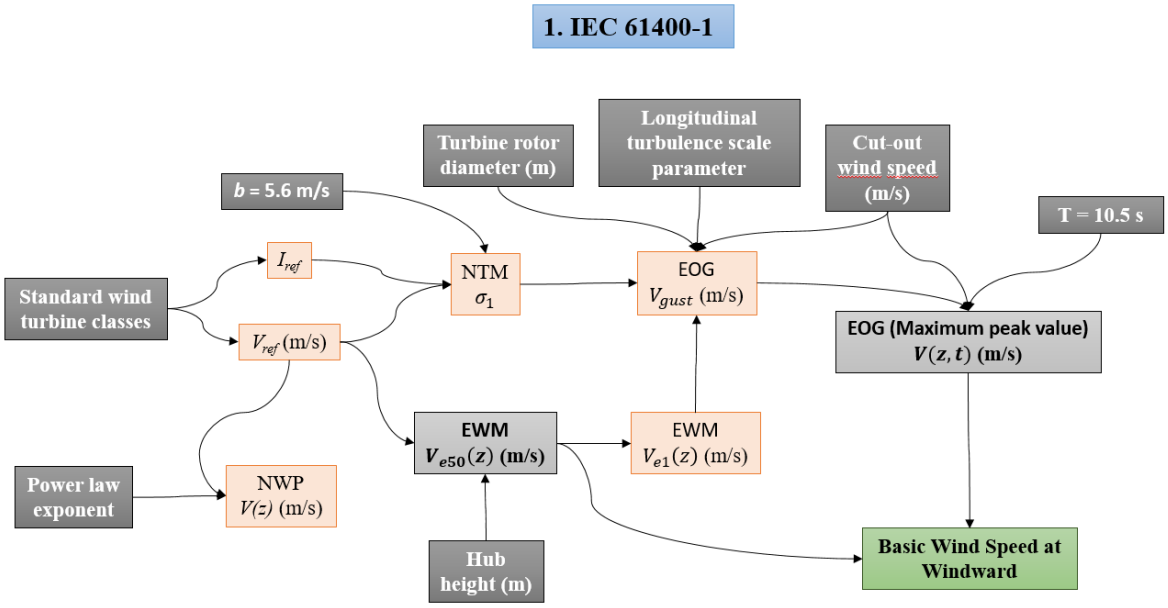

APPENDIX B – FLOWCHART FOR WIND PRESSURE AT WINDWARD ACCORDING TO ASCE 7-16

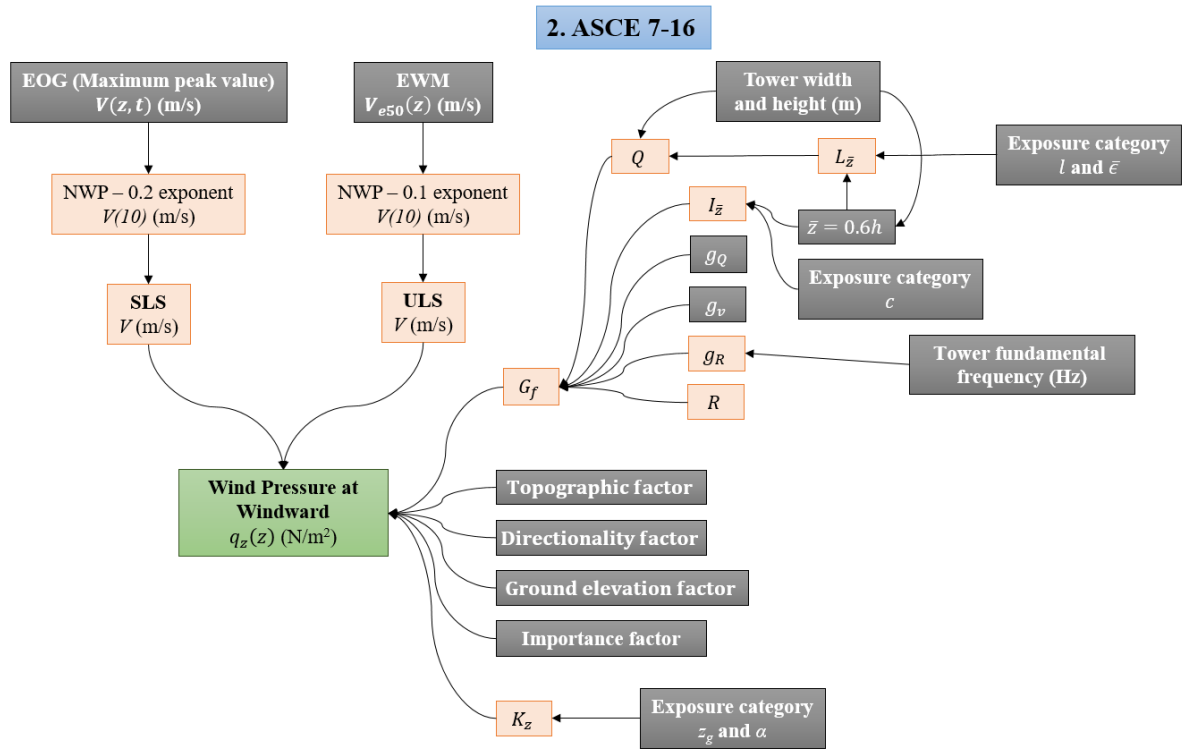

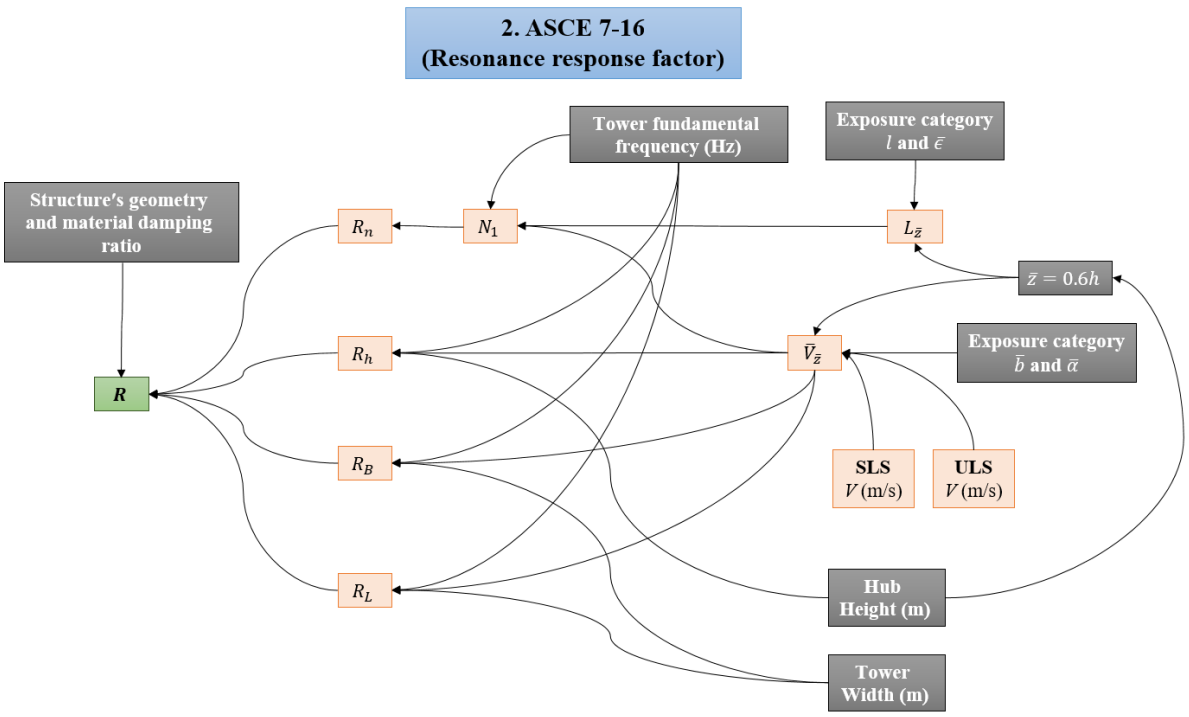

APPENDIX C – FEM FOR THE PRESTRESSED TOWER ANALYSIS

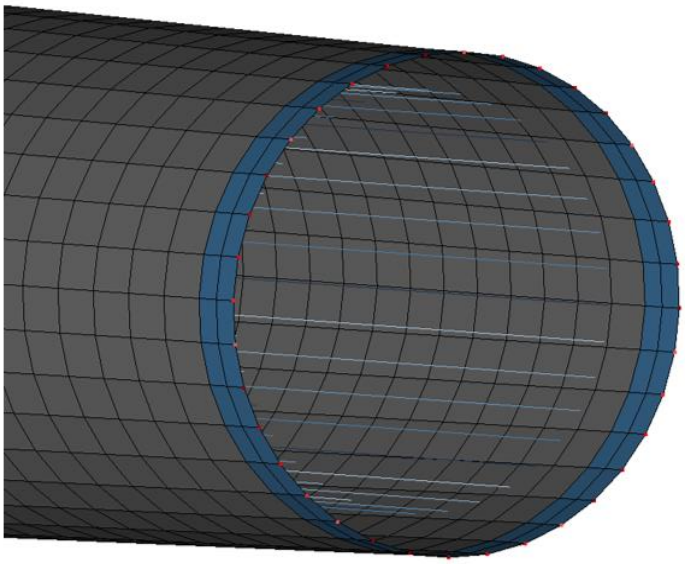

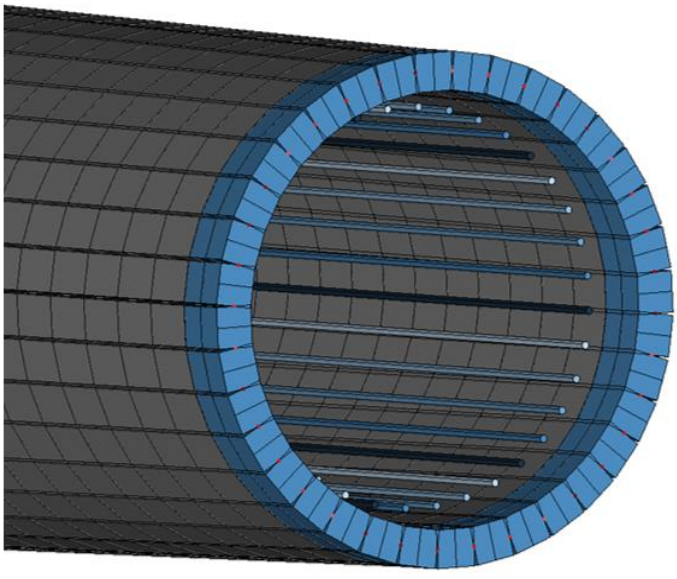

APPENDIX D – FEM FOR THE PRESTRESSED TOWER ANALYSIS WITH FOUNDATION

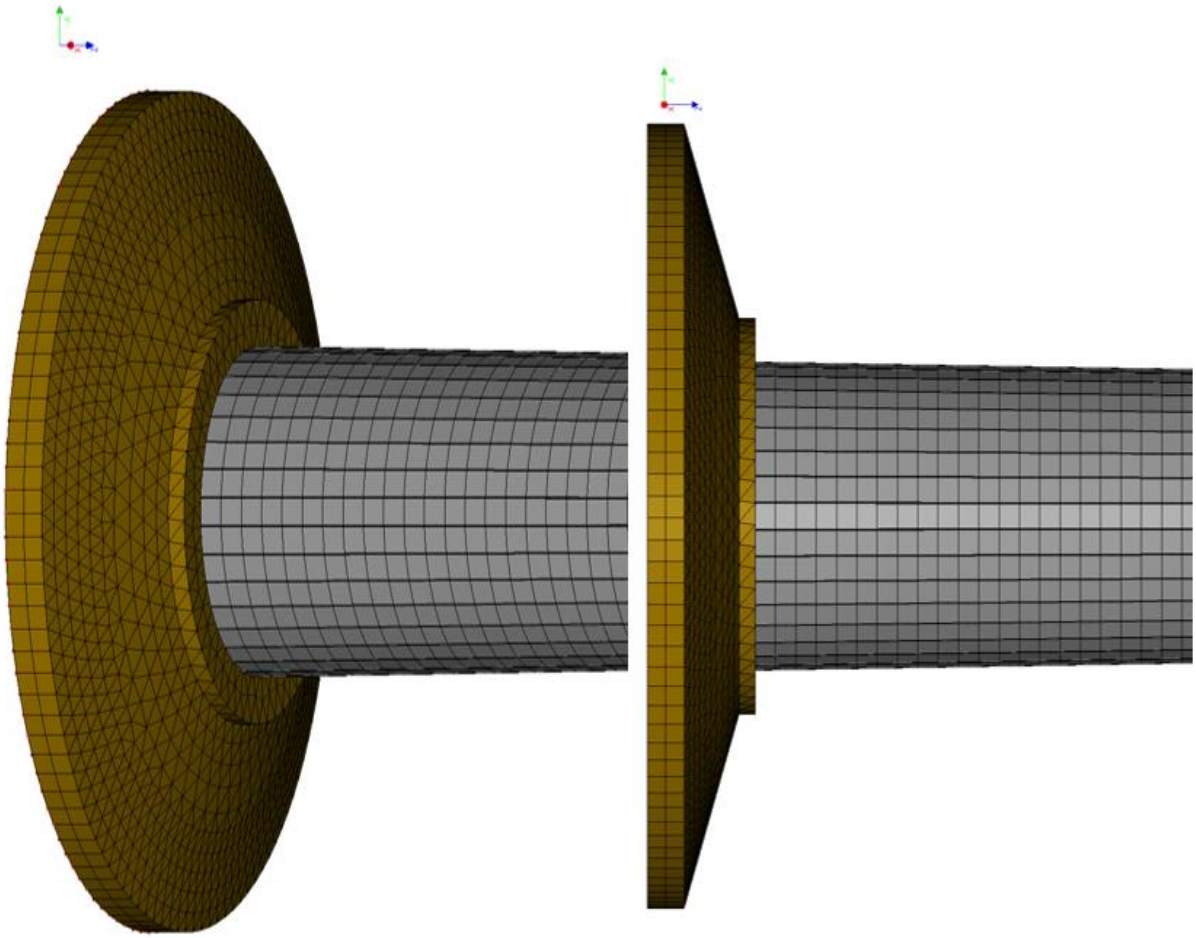

APPENDIX E – LIST OF ANALYSES DONE ON THE REINFORCED CONCRETE TOWER

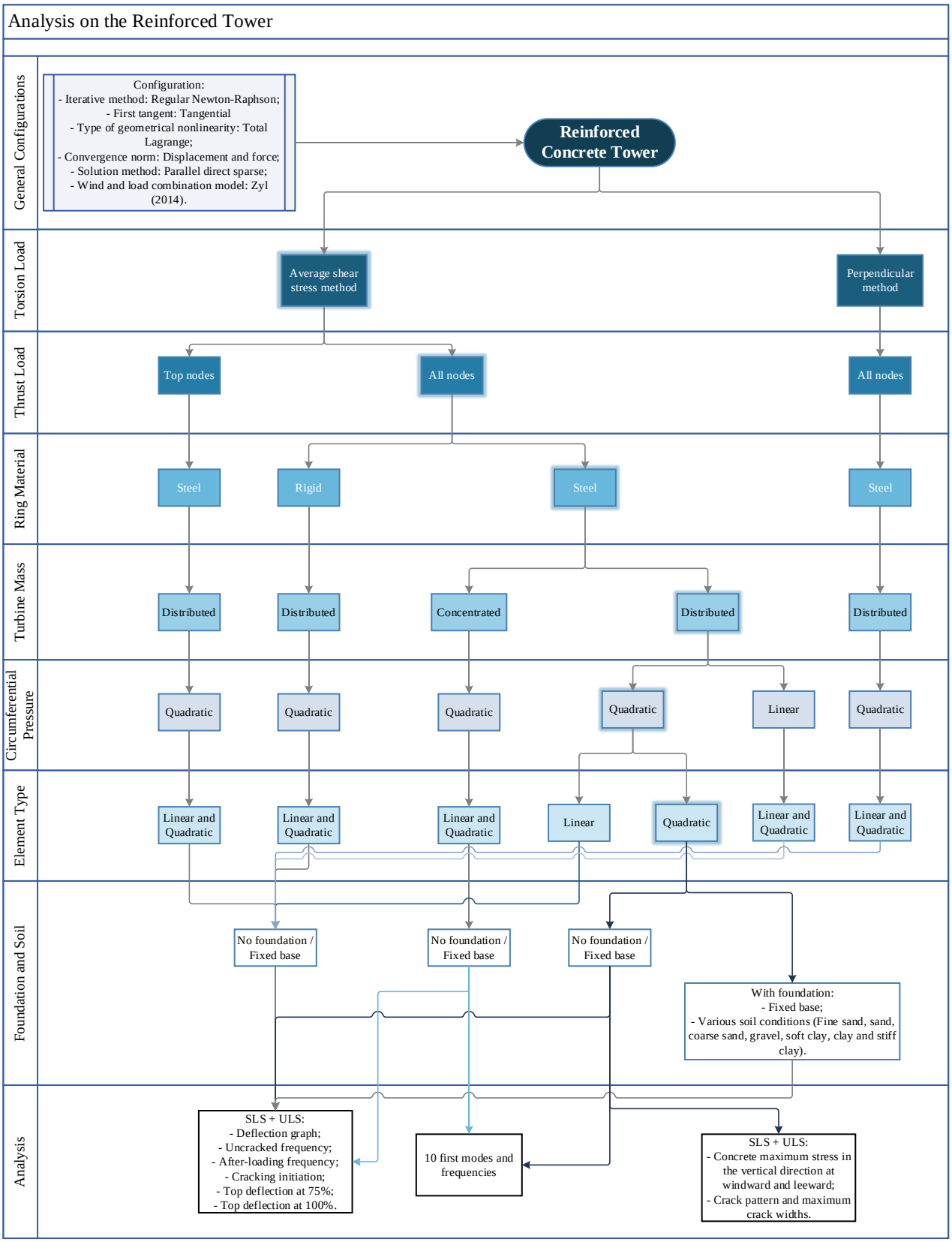

APPENDIX F – LIST OF ANALYSES DONE ON THE PRESTRESSED TOWER

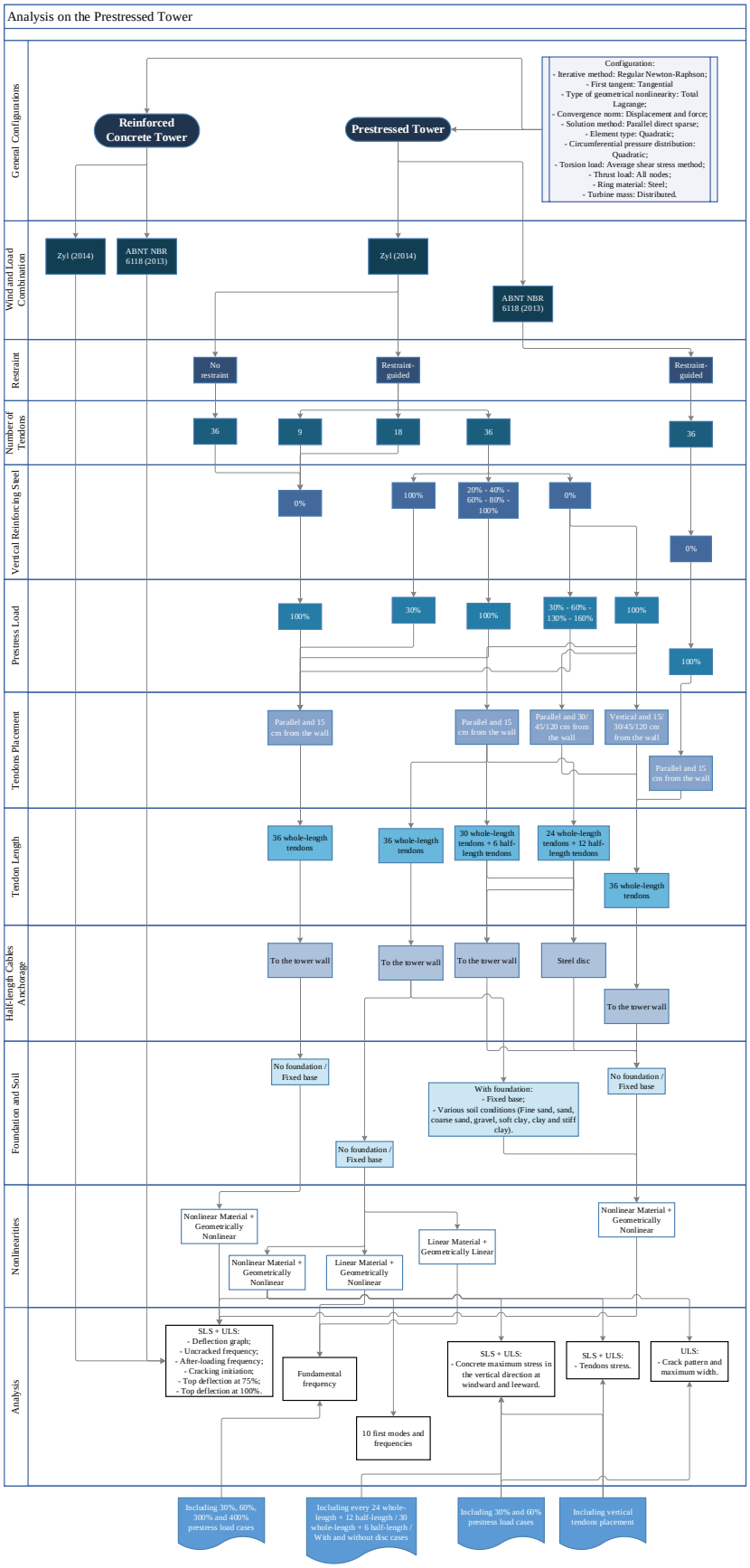

APPENDIX G – ULS RESULTS FOR REINFORCED CONCRETE TOWER ANALYSES

Results for the torsion force distribution analysis (ULS)

Source	Configuration		Uncracked frequency		After-loading frequency		Cracking initiation	Top deflection at 30%		Top deflection at 100%	
			Value (Hz)	Diff.[a] (%)	Value (Hz)	Diff.[a] (%)	Value[b] (%)	Value (mm)	Diff.[a] (%)	Value (mm)	Diff.[a] (%)
Zyl (2014)	Shell model		0.445	-	0.228	-	30	155.0	-	1808.0	-
Melo (2021)	Beam model		0.450	1.12	0.214	-6.14	30	166.4	7.35	2125.3	17.55
The present study	Zyl's method	Linear elements	0.440	-1.12	0.205	-10.09	30	162.6	4.90	2208.1	22.13
		Quadratic elements	0.440	-1.12	0.205	-10.09	30	162.4	4.78	2207.1	22.07
	Average shear stress method	Linear elements	0.440	-1.12	0.201	-11.84	30	162.6	4.89	2198.7	21.61
		Quadratic elements	0.440	-1.12	0.200	-12.28	30	162.4	4.77	2201.7	21.77

[a] Comparison to the results obtained from Zyl (2014); [b] Percentage of the total wind load.

Figure 47 – Deflection for the torsion force distribution analysis (ULS)

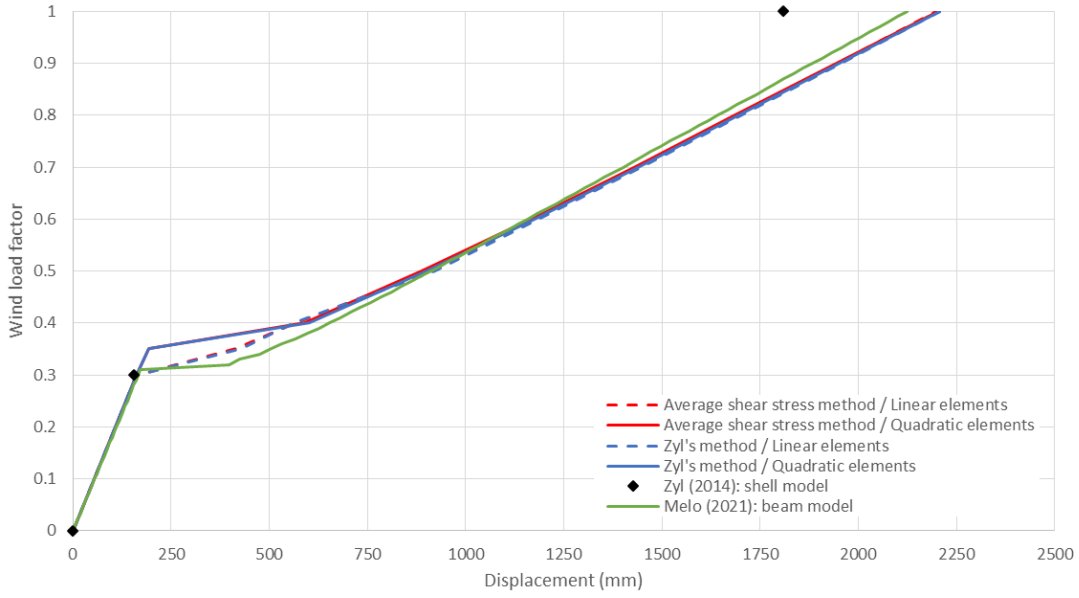

Results for the thrust force distribution analysis (ULS)

Source	Configuration		Uncracked frequency		After-loading frequency		Cracking initiation	Top deflection at 30%		Top deflection at 100%	
			Value (Hz)	Diff.[a] (%)	Value (Hz)	Diff.[a] (%)	Value[b] (%)	Value (mm)	Diff.[a] (%)	Value (mm)	Diff.[a] (%)
Zyl (2014)	Shell model		0.445	-	0.228	-	30	155.0	-	1808.0	-
Melo (2021)	Beam model		0.450	1.12	0.214	-6.14	30	166.4	7.35	2125.3	17.55
The present study	Applied on top nodes of the steel ring	Linear elements	0.440	-1.12	0.201	-11.84	30	164.1	5.88	2228.8	23.27
		Quadratic elements	0.440	-1.12	0.200	-12.28	30	162.9	5.09	2210.2	22.25
	Applied on all nodes of the steel ring	Linear elements	0.440	-1.12	0.201	-11.84	30	162.6	4.90	2198.7	21.61
		Quadratic elements	0.440	-1.12	0.200	-12.28	30	162.4	4.78	2201.7	21.77

[a] Comparison to the results obtained from Zyl (2014); [b] Percentage of the total wind load.

Deflection for the thrust force distribution analysis (ULS)

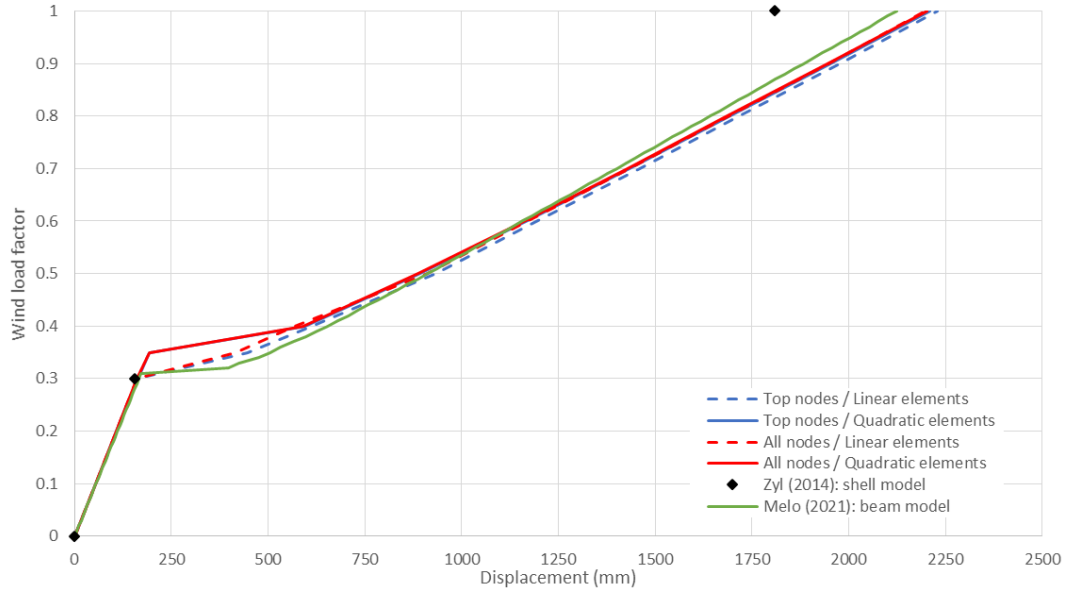

Results for the ring material analysis (ULS)

Source	Configuration		Uncracked frequency		After-loading frequency		Cracking initiation	Top deflection at 30%		Top deflection at 100%	
			Value (Hz)	Diff.[a] (%)	Value (Hz)	Diff.[a] (%)	Value[b] (%)	Value (mm)	Diff.[a] (%)	Value (mm)	Diff.[a] (%)
Zyl (2014)	Shell model		0.445	-	0.228	-	30	155.0	-	1808.0	-
Melo (2021)	Beam model		0.450	1.12	0.214	-6.14	30	166.4	7.35	2125.3	17.55
The present study	Rigid ring	Linear elements	0.440	-1.12	0.201	-11.84	30	162.6	4.87	2200.4	21.70
		Quadratic elements	0.440	-1.12	0.201	-11.84	30	162.4	4.76	2203.1	21.86
	Steel ring	Linear elements	0.440	-1.12	0.201	-11.84	30	162.6	4.89	2198.7	21.61
		Quadratic elements	0.440	-1.12	0.200	-12.28	30	162.4	4.77	2201.7	21.77

[a] Comparison to the results obtained from Zyl (2014); [b] Percentage of the total wind load.

Deflection for the ring material analysis (ULS)

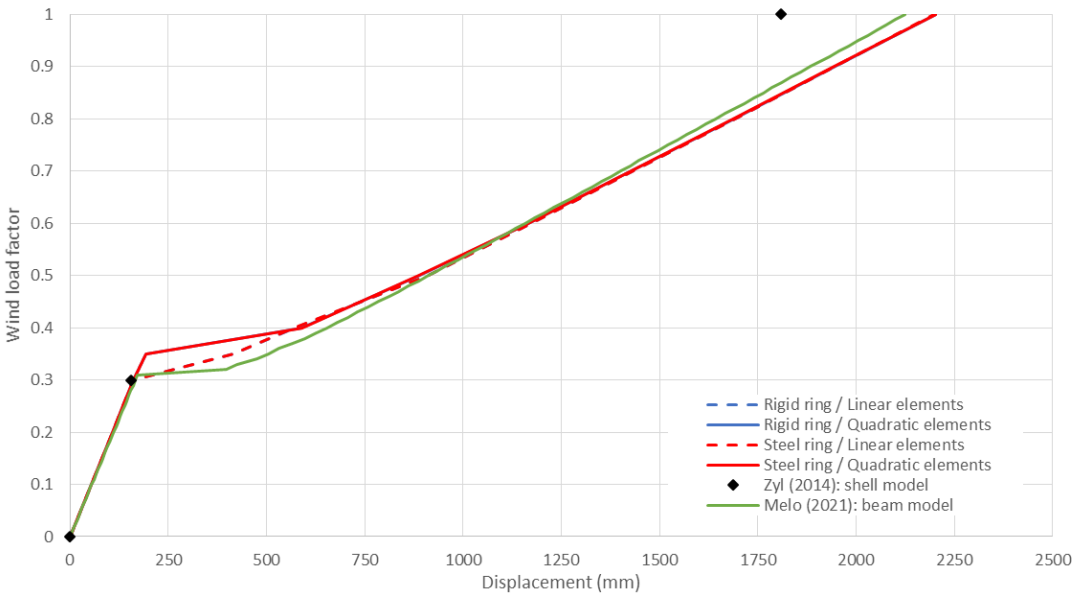

Source: elaborated by the author.

Results for the soil-structure interaction analysis on reinforced tower (ULS)

Soil type and foundation configuration		Uncracked frequency		After-loading frequency		Cracking initiation	Top deflection at 30%		Top deflection at 100%	
		Value (Hz)	Diff.[a] (%)	Value (Hz)	Diff.[a] (%)	Value[b] (%)	Value (mm)	Diff.[a] (%)	Value (mm)	Diff.[a] (%)
No foundation / Fixed base		0.440	-	0.200	-	30	162.4	-	2201.7	-
With foundation	Fixed	0.421	-4.32	0.198	-1.00	35	174.6	7.50	2250.7	2.23
	Fine sand	0.355	-19.32	0.188	-6.00	35	231.9	42.82	2468.6	12.12
	Sand	0.375	-14.77	0.191	-4.50	35	211.7	30.36	2391.9	8.64
	Coarse sand	0.381	-13.41	0.192	-4.00	35	206.1	26.93	2369.5	7.62
	Gravel	0.393	-10.68	0.194	-3.00	35	195.6	20.45	2337.6	6.17
	Soft clay	0.270	-38.64	0.168	-16.00	35	377.3	132.36	3030.7	37.65
	Clay	0.320	-27.27	0.181	-9.50	35	277.7	71.01	2649.4	20.33
	Stiff clay	0.361	-17.95	0.189	-5.50	35	225.5	38.85	2448.8	11.22

[a] Comparison to the no foundation / fixed base analysis; [b] Percentage of the total wind load.

Deflection for the soil-structure interaction analysis on reinforced tower (ULS)

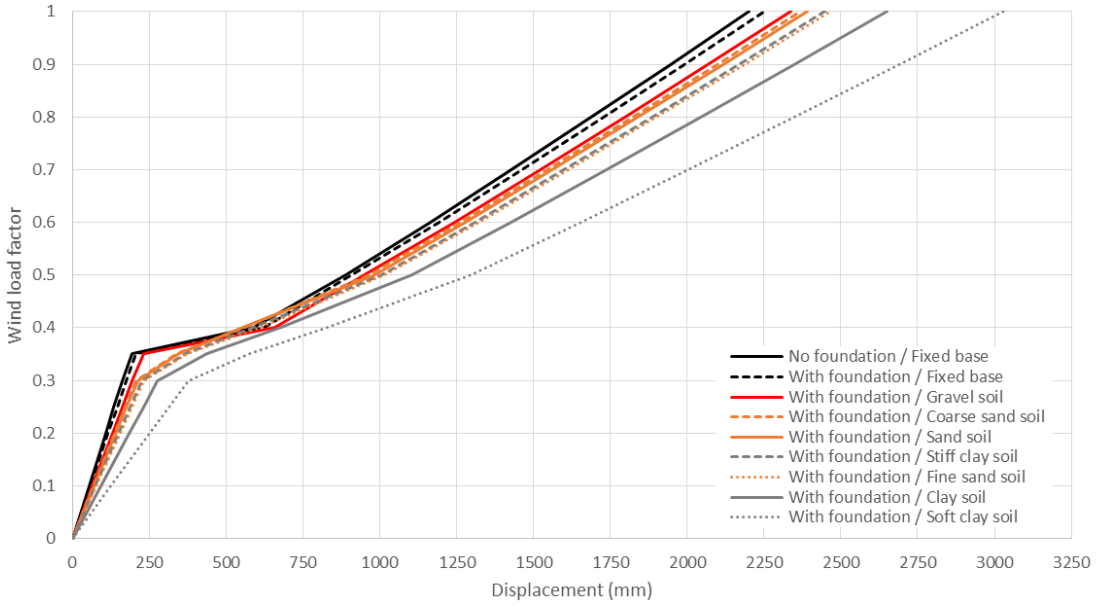

APPENDIX H – ULS RESULTS FOR PRESTRESSED CONCRETE TOWER ANALYSES

Results for the deviators and amount of prestressing tendons analysis (ULS)

Tower configuration			Uncracked frequency		After-loading frequency		Cracking initiation	Top deflection at 30%		Top deflection at 100%	
			Value (Hz)	Diff.[a] (%)	Value (Hz)	Diff.[a] (%)	Value[b] (%)	Value (mm)	Diff.[a] (%)	Value (mm)	Diff.[a] (%)
Reinforced Tower			0.440	-	0.200	-	30	162.4	-	2201.7	-
Prestressed Tower	Without deviators	9, 18 and 36 tendons	0.380	-13.64	0.320	60.00	90	223.9	37.90	778.7	-64.63
	Deviator-guided	9 and 18 tendons	0.418	-5.00	0.414	107.00	90	203.2	25.12	677.1	-69.25
		36 tendons	0.418	-5.00	0.411	105.50	90	203.2	25.12	678.3	-69.19

[a] Comparison to the reinforced tower; [b] Percentage of the total wind load.

Deflection for the deviators and amount of prestressing tendons analysis (ULS)

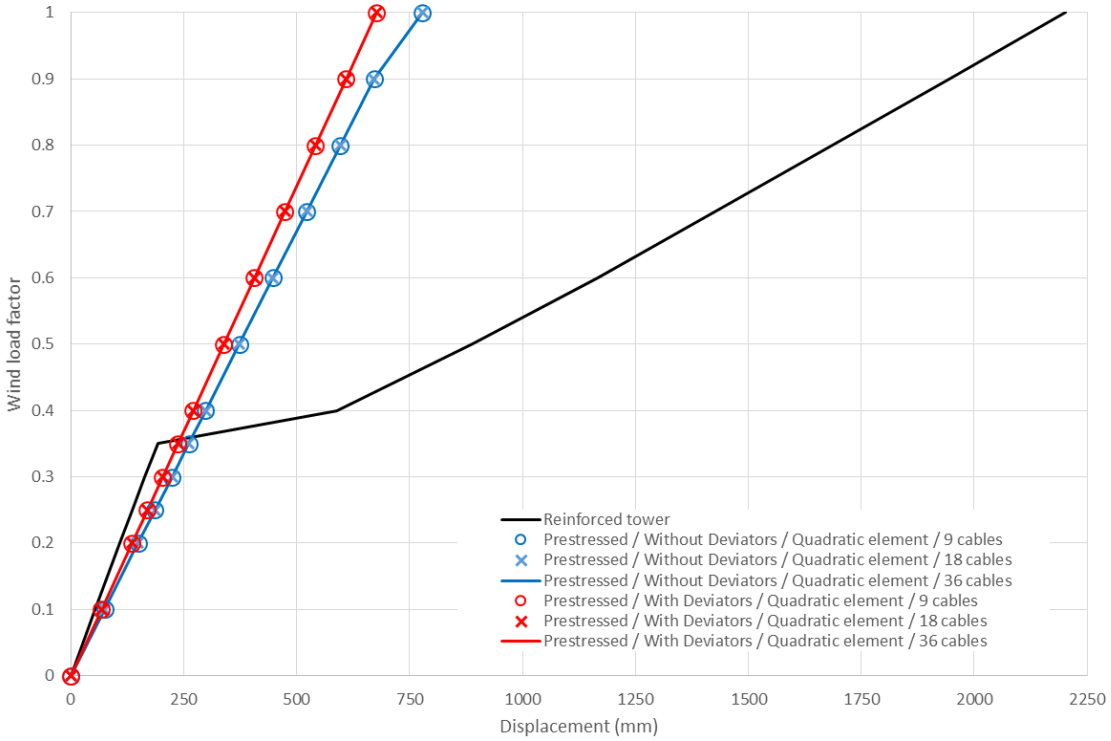

Deflection for the vertical reinforcing analysis (ULS)

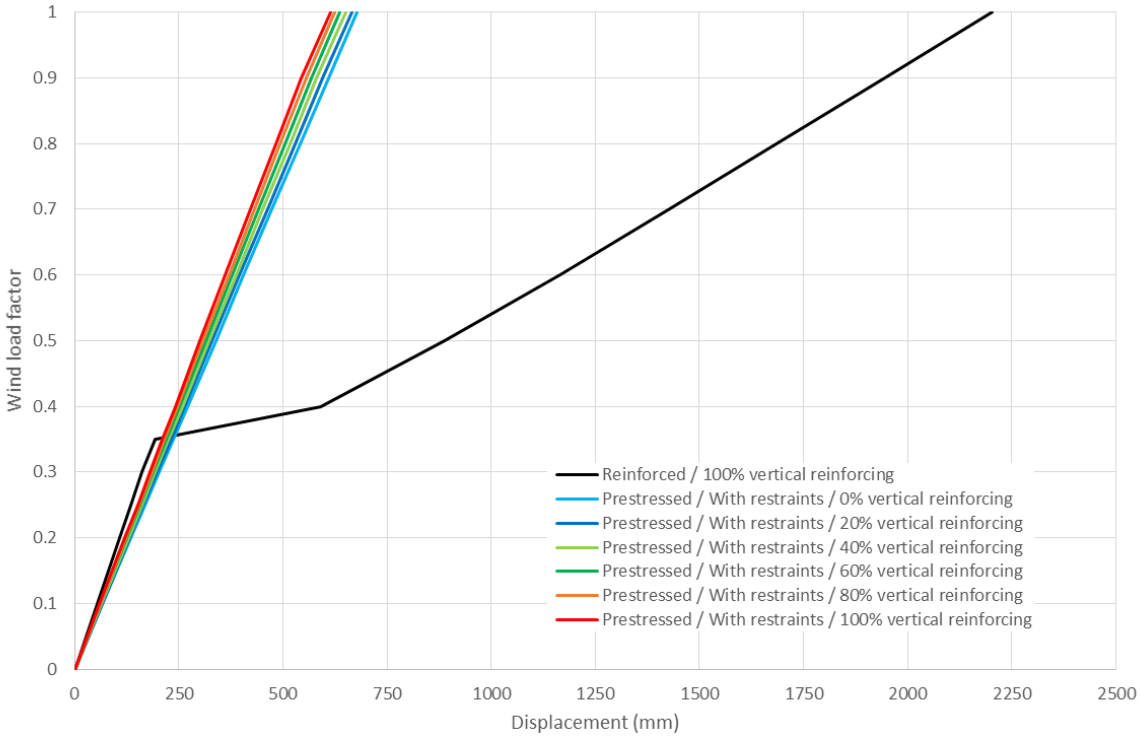

Tower's behavior versus vertical reinforcing at ULS (100% vertical reinforcing = 5068 mm²/m): a) fundamental frequency, b) top displacement

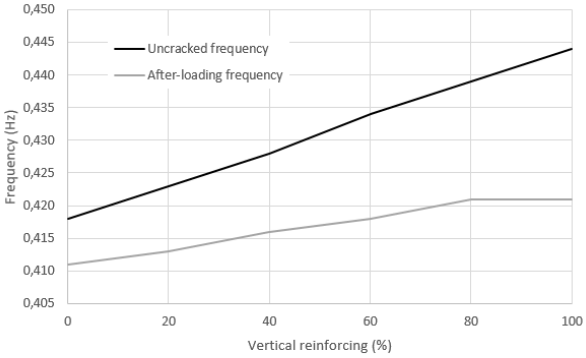

(a)

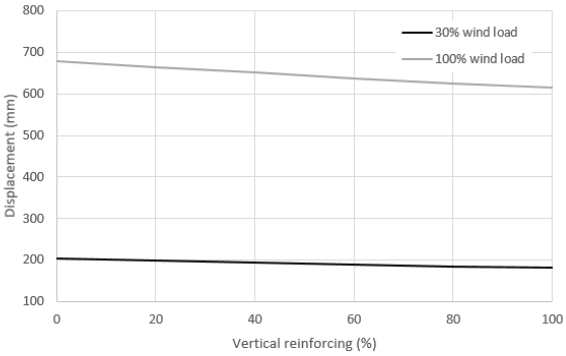

(b)

Results for the soil-structure interaction analysis on prestressed tower (ULS)

Soil type and foundation configuration		Uncracked frequency		After-loading frequency		Cracking initiation	Top deflection at 30%		Top deflection at 100%	
		Value (Hz)	Diff.[a] (%)	Value (Hz)	Diff.[a] (%)	Value[b] (%)	Value (mm)	Diff.[a] (%)	Value (mm)	Diff.[a] (%)
No foundation / Fixed base		0.418	-	0.411	-	90	203.2	-	678.3	-
With foundation	Fixed	0.401	-4.07	0.368	-10.46	100	216.5	6.57	733.8	8.18
	Fine sand	0.349	-16.51	0.308	-25.06	70	273.9	34.80	940.7	38.69
	Sand	0.364	-12.92	0.322	-21.65	80	254.8	25.39	873.2	28.75
	Coarse sand	0.368	-11.96	0.325	-20.92	80	249.3	22.71	854.6	25.99
	Gravel	0.378	-9.57	0.352	-14.36	90	238.6	17.46	808.5	19.21
	Soft clay	0.288	-31.10	0.258	-37.23	40	383.7	88.87	1320.5	94.68
	Clay	0.323	-22.73	0.286	-30.41	60	313.2	54.14	1077.4	58.85
	Stiff clay	0.353	-15.55	0.314	-23.60	70	267.9	31.86	919.2	35.53

[a] Comparison to the no foundation / fixed base analysis; [b] Percentage of the total wind load.

Deflection for the soil-structure interaction analysis on prestressed tower (ULS)

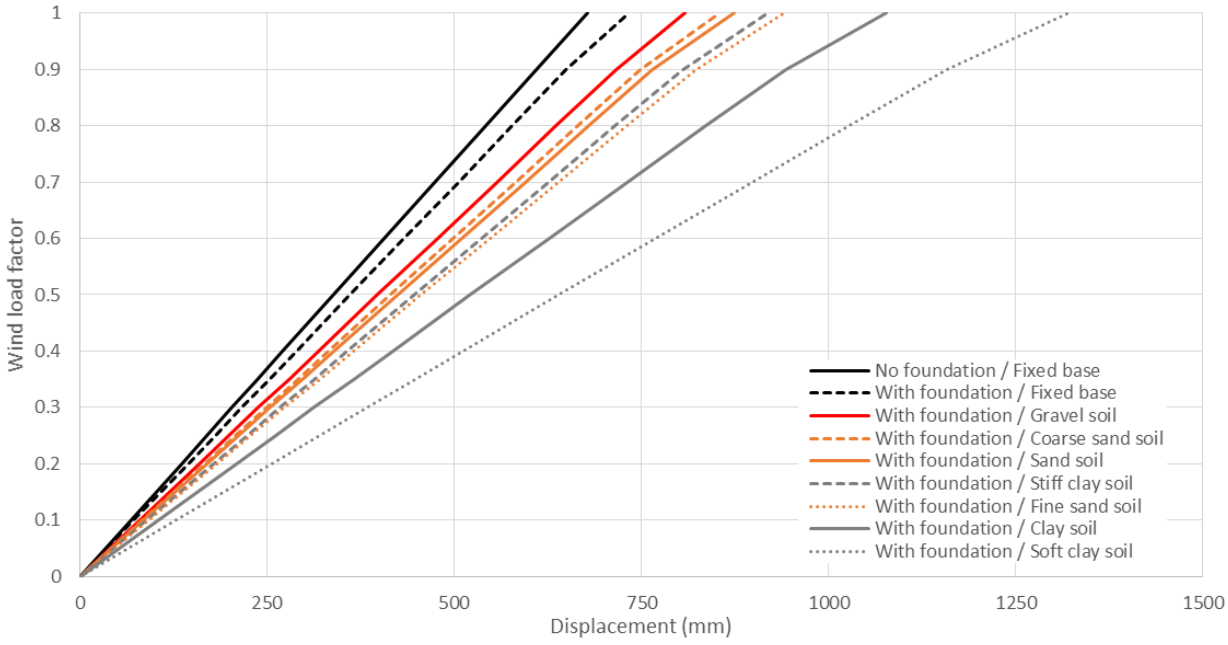

APPENDIX I – ULS RESULTS FOR WIND LOAD ANALYSES

Results for the wind and load combination models analysis (ULS)

Type of tower	Wind and load combination model	Uncracked frequency		After-loading frequency		Cracking initiation	Top deflection at 30%		Top deflection at 100%	
		Value (Hz)	Diff.[a] (%)	Value (Hz)	Diff.[a] (%)	Value[b] (%)	Value (mm)	Diff.[a] (%)	Value (mm)	Diff.[a] (%)
Reinforced Tower	ABNT NBR	0.437	-0.68	0.201	0.50	35	152.6	-6.02	2018.6	-8.31
	Zyl (2014)	0.440	-	0.200	-	30	162.4	-	2201.7	-
Prestressed Tower	ABNT NBR	0.415	-0.72	0.413	0.49	-	163.0	-19.77	543.1	-19.92
	Zyl (2014)	0.418	-	0.411	-	90	203.2	-	678.3	-

[a] Comparison to Zyl's model; [b] Percentage of the total wind load.

Deflection for the wind and load combination models analysis (ULS)

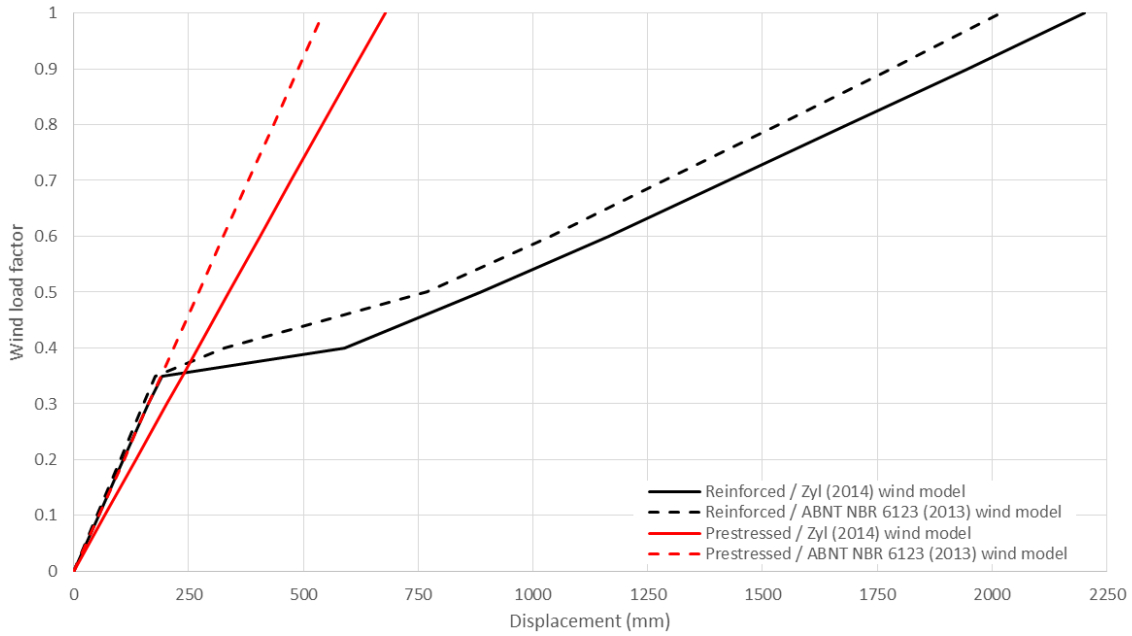

Wind load comparison at windward (ULS)

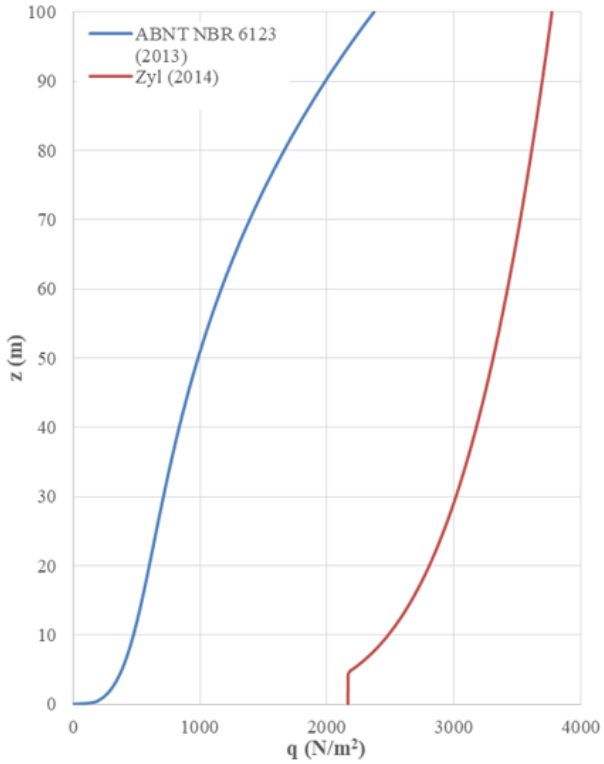

Deflection for the effect of direct wind load on tower analysis (ULS)

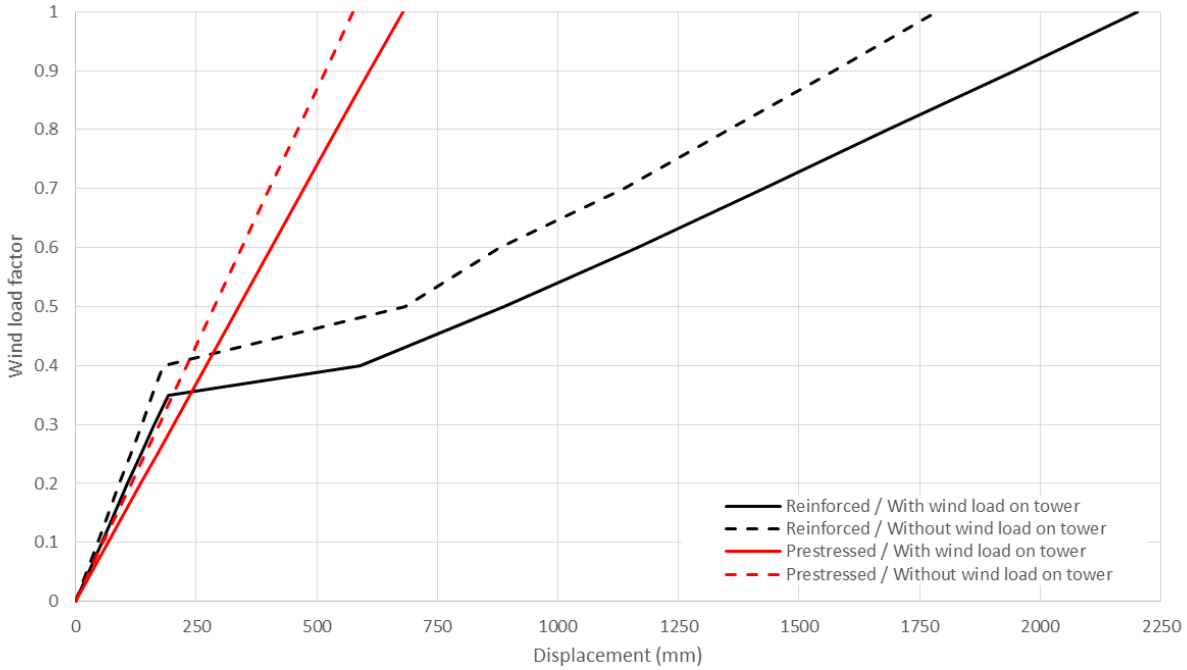

Results for the effect of direct wind load on tower analysis (ULS)

Type of tower	Direct wind load on tower	Uncracked frequency		After-loading frequency		Cracking initiation	Top deflection at 30%		Top deflection at 100%	
		Value (Hz)	Diff.[a] (%)	Value (Hz)	Diff.[a] (%)	Value[b] (%)	Value (mm)	Diff.[a] (%)	Value (mm)	Diff.[a] (%)
Reinforced Tower	Not considered	0.440	0.00	0.203	1.50	40	136.4	-16.03	1785.2	-18.92
	Applied	0.440	-	0.200	-	30	162.4	-	2201.7	-
Prestressed Tower	Not considered	0.418	0.00	0.414	0.73	-	172.5	-15.08	574.9	-15.24
	Applied	0.418	-	0.411	-	90	203.2	-	678.3	-

[a] Comparison to the applied wind load case; [b] Percentage of the total wind load.

ANNEX A – OTHERS FACTORS AND PARAMETERS FROM ABNT NBR 6123 (2013)

Minimum values for the statistical factor S_3

Class	Description	S_3
1	Buildings whose total or partial ruin may affect the safety or possibility of rescuing people after a destructive storm (hospitals, communication centers, etc.)	1.10
2	Buildings for hotels and residences. Buildings for commerce and industry with high occupancy factor	1.00
3	Industrial buildings and installations with low occupancy factor (deposit, silo, rural buildings, etc.)	0.95
4	Sealing (roof, glass, sealing panels, etc.)	0.88
5	Temporary buildings.	0.83

Source: ABNT NBR 6123 (2013).

Values for the exponent p and parameter b

Terrain roughness class	I	II	III	IV	V
p	0.095	0.15	0.185	0.23	0.31
b	1.23	1.00	0.86	0.71	0.50

Source: ABNT NBR 6123 (2013).

Values for the critical damping factor ζ and parameter γ

Building type	γ	ζ
Buildings with concrete structures, without curtains	1.2	0.020
Buildings with concrete structures, with curtains to absorb horizontal loads	1.6	0.015
Concrete towers and chimney, variable cross-section	2.7	0.015
Concrete towers and chimney, uniform cross-section	1.7	0.010
Buildings with welded steel structures	1.2	0.010
Steel towers and chimney, uniform cross-section	1.7	0.008
Wood structures	-	0.030

Source: ABNT NBR 6123 (2013).

ANNEX B – LOAD FACTORS AND COMBINATION FROM THE ABNT NBR 6118 (2014)

Ultimate limit state load factors

The loads' values are modified according to the load factor γ_f, given by:

$$\gamma_f = \gamma_{f1}\gamma_{f2}\gamma_{f3}$$

and the values for the load factors $\gamma_{f1}.\gamma_{f3}$ and γ_{f2} are listed in the following tables:

Load factor $\gamma_f = \gamma_{f1}.\gamma_{f3}$

Load combinations	**Actions**							
	Permanent (*g*)		**Variable (*q*)**		**Prestressing (*p*)**		**Foundation settlement and retraction**	
	D	***F***	***G***	***T***	***D***	***F***	***D***	***F***
Normal	1.4[a]	1.0	1.4	1.2	1.2	0.9	1.2	0

where

D is for unfavorable actions, *F* is for favorable, *G* is for variable actions and *T* is temperature.

[a] For small variability permanent loads, such as the structure self-weight, especially precast, this factor can be reduced to 1.3.

Source: ABNT NBR 6118 (2014).

Load factor γ_{f2} for wind loads

Actions		γ_{f2}		
		ψ_0	ψ_1	ψ_2
Wind	Dynamic wind pressure on structures in general	0.6	0.3	0

Source: ABNT NBR 6118 (2014).

The values for permanent action factors of the same origin, in the same loading condition, must be the same throughout the whole structure.

For each critical load case design values of the effects of actions are determined by combining the effects of actions that are considered to act simultaneously, the values for

permanent and variable actions must be taken into consideration using their respective load factors. The combinations for normal situations are described in the following table:

ULS normal load combination

Ultimate combination	**Description**	**Combinations**
Normal	Failure by excessive deformation for reinforced concrete[a]	$F_d = \gamma_g F_{gk} + \gamma_{\varepsilon g} F_{\varepsilon gk} + \gamma_q \left(F_{q1k} + \Sigma \psi_{0j} F_{qjk}\right) + \gamma_{\varepsilon q} \psi_{0\varepsilon} F_{\varepsilon qk}$
	Failure by excessive deformation for prestressed concrete	Must be considered, when necessary, the prestress load as an external load with the maximum and minimum values for unfavorable and favorable, respectively.

where:

F_d is the representative value of action for ultimate combinations;

F_{gk} represents the direct permanent actions;

$F_{\varepsilon k}$ represents the indirect permanent actions such as shrinkage $F_{\varepsilon gk}$ and variables such as temperature $F_{\varepsilon qk}$;

F_{qk} represents the direct variable actions, and the main one is represented as F_{q1k};

$\gamma_g, \gamma_{\varepsilon g}, \gamma_q, \ \gamma_{\varepsilon q}$ are described previously;

$\psi_{0j}, \psi_{0\varepsilon}$ are described previously;

a In general, combinations where the favorable effects of permanent actions are reduced by considering $\gamma_g = 1.0$ must also be taken into consideration. For regular structures and buildings, the combinations where $\gamma_g = 1.0$ does not need to be taken into consideration.

Source: ABNT NBR 6118 (2014).

Serviceability limit state load factors

The loads are modified according to the load factor γ_f, described by:

$$\gamma_f = \gamma_{f2}$$

where γ_{f2} varies depending on the analysis condition (according to table for load factor for wind load), $\gamma_{f2} = 1$ for characteristic combinations, $\gamma_{f2} = \psi_1$ for frequent combinations and $\gamma_{f2} = \psi_2$ for quasi-permanent combinations.

The serviceability combinations are classified according to their permanency on the structure and must be verified as follows:

a) Quasi-permanent combination: may act during most of the lifespan of the structure, its consideration may be necessary to verify the excessive deformation limit state, it is the typically long term effects and appearance of the structure;
b) Frequent combination: repeats itself many times during the lifespan of the structure, its consideration may be necessary for the verification of cracking initiation, cracking opening and excessive vibration limit states. It may be considered for verification of excessive deformations limit state caused by wind or temperature. It is a typically reversible limit state;
c) Characteristic (rare) combination: rarely occurs during the lifespan of the structure, may be considered for crack initiation limit state. It is a typically irreversible limit state.

The serviceability combinations are described in the following table:

SLS load combinations

Serviceability combination	**Description**	**Combinations**
Quasi-permanent	All variable actions are considered with their respective quasi-permanent values $\psi_2 F_{qk}$	$F_{d,ser} = \Sigma F_{gik} + \Sigma \psi_{2j} F_{qjk}$
Frequent	The main variable action F_{q1} is taken as its frequent value $\psi_1 F_{q1k}$ and all other variable actions are taken as their respective quasi-permanent values $\psi_2 F_{qk}$	$F_{d,ser} = \Sigma F_{gik} + \psi_1 F_{q1k} + \Sigma \psi_{2j} F_{qjk}$
Characteristic (rare)	The main variable action F_{q1} is taken as its characteristic value F_{q1k} and all other actions are taken as their respective frequent values $\psi_1 F_{qk}$	$F_{d,ser} = \Sigma F_{gik} + F_{q1k} + \Sigma \psi_{1j} F_{qjk}$

where:

$F_{d,ser}$ is the representative value of action for serviceability combinations;

F_{q1k} is the characteristic value for the main direct variable actions;

ψ_1 is the SLS frequent combination reduction factor;

ψ_2 is the SLS quasi-permanent combination reduction factor.

Source: ABNT NBR 6118 (2014).